Mechanics of swelling and damage in brain tissue: a theoretical approach

Georgina E. Lang

St Catherine's College

University of Oxford

A thesis submitted for the degree of

Doctor of Philosophy in Mathematics

Trinity Term 2014

Mechanics of swelling and damage in brain tissue: a theoretical approach

Georgina E. Lang

St Catherine's College

University of Oxford

A thesis submitted for the degree of
Doctor of Philosophy in Mathematics

Trinity Term 2014

Following trauma, such as an impact injury or stroke, brain tissue can swell. Swelling is the result of water accumulation in the tissue that is driven by pathological changes, such as increased permeability of the capillary walls and osmotic pressure changes within the tissue. Swelling causes increased intracranial pressure and mechanical deformation of the brain tissue, exacerbating the original injury. Furthermore, prolonged local swelling can lead to the spread of damage to the (initially undamaged) surrounding tissue, since compression and increased intracranial pressure may restrict blood flow in this tissue.

In this thesis, we develop mathematical models to examine the consequences of pathophysiological damage mechanisms on the swelling, and associated stress and strain, experienced by brain tissue. Mixture theory is used to represent brain tissue as a mixture of elastic solid, fluid and solutes. This modelling approach allows elastic deformations to be coupled with hydrodynamic pressure and osmotic gradients; the consequences of different mechanisms of damage may then be quantified.

We consider three particular problems motivated by experimental observations of swelling brain tissue. Firstly, we investigate the swelling of isolated, damaged, brain tissue slices; we show that mechanisms leading to an osmotic pressure difference between the tissue slice and its surroundings can explain experimental observations for swollen tissue slices. Secondly, we use our modelling approach to demonstrate that local changes in capillary permeability can cause significant stresses and strains in the surrounding tissue. Thirdly, we investigate the conditions under which a locally swollen, damaged, region can cause compression of the vasculature within the surrounding tissue, and potentially result in damage propagation. To do this, we propose a coupled model for the oxygen concentration within, and mechanical deformation of, brain tissue. We use our model to assess the impact of treatment strategies on damage propagation through the tissue, and show that performing a craniectomy reduces the extent of propagation.

Acknowledgements

I am immensely grateful to my supervisors, Alain Goriely, Dominic Vella, and Sarah Waters, for their huge amount of input and advice; I am privileged to have had the opportunity to work with such an innovative and insightful team of supervisors. I also thank Peter Stewart for help over the first couple of years of my DPhil, particularly with numerical simulations.

I have been fortunate to be a member of the Oxford Centre for Collaborative Applied Maths (OCCAM) during my DPhil, and am grateful to everyone who has made Oxford maths such a friendly and supportive place to study.

I gratefully acknowledge funding from the EPSRC and St Catherine's College.

Contents

Table of Mathematical Notation

α^n	Material parameter featuring in the Ogden constitutive law
$\mathbf{B}$	Left Cauchy-Green deformation tensor
c	Strain-stiffening parameter featuring in the Fung constitutive law
c^i	Concentration of solute i
c^f	Fixed charge density (FCD)
c_0^f	Reference state fixed charge density
c^*	Ionic concentration of bathing solution
$\mathcal{C}$	Oxygen concentration
$\mathcal{C}_{cap}$	Capillary oxygen concentration
$\mathcal{C}_{crit}$	Critical oxygen concentration, below which tissue becomes hypoxic
D^i	Diffusion coefficient of ith solute in solvent-solute mixture
D_0^i	Diffusion coefficient of ith solute in pure solvent
μ_s	Young's modulus of mixture
f_{ij}	Friction coefficient between phases i and j
F	Faraday constant
$\mathbf{F}$	Deformation gradient tensor
H	Radius of tissue region
J	Ratio between reference and deformed volume
k	Permeability of tissue to pure solvent
K	Permeability of tissue to solvent and solute mixture
k_m	Michaelis-Menten constant for oxygen uptake
κ_s	Bulk modulus of mixture
L_p	Blood brain barrier permeability
λ	Tissue stretch (ratio of current to reference state length)
λ_s	First Lamé parameter of mixture
M^i	Molar mass of phase i
μ^i	Chemical potential of phase i

μ_s	Second Lamé parameter (shear modulus) of mixture
μ'	Material parameter featuring in the Ogden constitutive law
ν	Poisson ratio of mixture
p	Pore pressure
p^*	Pressure of bathing solution
P_e	Transvascular driving pressure
ϕ^i	Volume fraction of phase i
ϕ_0^i	Reference state volume fraction of phase i
$\mathbf{q}^w := \phi^w(\mathbf{v}^w - \mathbf{v}^s)$	Fluid flux
R	Ideal gas constant
ρ^i	Mixture density of phase i
ρ_T^i	True density of phase i
$\mathbf{S}$	Mixture first Piola-Kirchhoff stress
$\mathbf{S}_e$	Mixture effective first Piola-Kirchhoff stress
σ_{crit}	Critical compressive Cauchy stress causing closure of capillaries
σ^i	Reflection coefficient of solute i
$\boldsymbol{\sigma}$	Mixture Cauchy stress
$\boldsymbol{\sigma}_e$	Mixture effective Cauchy stress
t	Time
T	Temperature
$\mathbf{u}$	Displacement
$\mathbf{v}^i$	Velocity of phase i
V_m	Maximal rate of oxygen uptake
$W(\mathbf{F})$	Strain energy function of mixture
$\mathbf{x}$	Reference state material coordinates
$\mathbf{X}$	Current state material coordinates
ξ	Electric potential
z^i	Valence of solute i

List of Acronyms

BBB	Blood brain barrier
CSF	Cerebrospinal fluid
FCD	Fixed charge density
GAG	Glycosaminoglycan
ISF	Interstitial fluid
SAS	Subarachnoid space

Chapter 1

Introduction

1.1 Motivation

The brain is the most intricate organ in the body. It consists of soft tissue, within which a complex network of neurons form the hub of the nervous system. For correct physiological function, the brain must maintain a delicate chemical balance. The consequences of disrupting this balance can be devastating, and are the motivation for this thesis.

Following damage such as stroke or traumatic brain injury (TBI), brain tissue has been observed to swell. Brain swelling, or edema, occurs when there is an abnormal accumulation of water within brain tissue. It is thought that this water accumulation is driven by a combination of osmotic effects and changes in resistance to fluid flow through the brain, as tissue structure and cellular behaviour are affected by damage (Simard *et al.*, 2007).

As the brain is confined by the skull, local swelling may cause compression of other regions of tissue, increased intracranial pressure and restricted blood supply to the brain (Walberer *et al.*, 2008). When brain cells are deprived of oxygen they are unable to function normally, and prolonged lack of oxygen can lead to cell death (Lo *et al.*, 2005).

Stroke, TBI, and the resulting edema can have long term consequences. For example, over two thirds of people who have a stroke will have some disability one year later as a consequence of damage to the brain tissue during stroke. The effects can be wide ranging including memory problems, physical weakness and paralysis, and loss of eyesight (National Stroke Association). To enable treatments to be developed, it is of critical importance to understand the underlying physical phenomena that cause brain tissue to swell following injury.

We aim to offer physical insight into the effects that drive brain tissue swelling, using mathematical models that couple osmotic pressure, hydrostatic pressures, and tissue deformation. In particular, we aim to incorporate the known biological causes of swelling

into mathematical models, to allow us to quantify the effects of these on the mechanical behaviour of the tissue. This allows us to determine the importance of different biological effects, and systematically rule out any effects that may be irrelevant to brain tissue swelling.

1.2 Biological background

In this section we discuss how the brain functions under normal conditions, and the physiological changes that lead to swelling. In §1.2.1 we discuss the basic brain physiology, and in particular the fluid networks within the brain. In §1.2.2 we summarise the causes of brain edema, and finally in §1.2.3 we review the consequences of brain edema. For ease of reference, the key biological terminology is collected together in Appendix C with simple definitions.

1.2.1 Introduction to brain physiology

The brain consists of soft tissue enclosed within a rigid skull, which protects the soft brain from damage due to impact. See Figure 1.1.

Tissue composition

Brain tissue can be described as a porous medium consisting of cells and extracellular matrix (ECM) bathed in interstitial fluid (ISF).

Figure removed due to copyright

Figure 1.1: Schematic of the structure of the brain, showing location of brain tissue, ventricles and skull. Source: www.pennmedicine.org, accessed August 2014.

Cells within the brain are classified into two types: neurons, which are responsible for information transmission, and glial cells, which perform various support functions for the neurons (such as secretion of growth factors and structural support). Neurons are star-shaped cells with a body from which long axons and dendrites protrude to connect with other neurons and allow the passage of chemical and electrical signals through the brain (Nolte, 1998). If axons are damaged then these signals can no longer propagate through the brain, causing

loss of brain function. Ultimately, axonal damage can lead to brain damage, coma and death (Smith and Meaney, 2000).

Neurons and astrocytes are arranged in such a way that tissue can be categorised into two regions. Grey matter contains most of the neuronal cell bodies and a high density of astrocytes, whilst white matter consists primarily of bundles of neuronal axons and more sparsely distributed astrocytes (Nolte, 1998). Typically grey matter is found close to the surface of the brain, whilst white matter is found deeper inside.

Cells bind to the extracellular matrix (ECM), which provides structural support to the tissue and is involved in cell signalling (Novak and Kaye, 2000). The ECM of the brain is composed of fibrous proteins (such as collagen) and negatively charged macromolecules (glycosaminoglycans and proteoglycans) (Syková and Nicholson, 2008). We refer to these negatively charged molecules as the fixed charge density (FCD), since these charges are immobile and attached to the ECM. Recent experimental evidence suggests that brain cells also contain an intracellular FCD that is exposed when the tissue is damaged (Elkin *et al.*, 2010); we shall discuss this further in Chapter 3. Interstitial fluid (ISF) is present in the spaces between the extracellular matrix and cells; nutrients and ions can travel through the tissue by diffusion (Nicholson, 2001) and advection (Abbott, 2004) in the ISF.

Fluid networks

There are three coupled fluid networks in the brain: blood, interstitial fluid (ISF) and cerebrospinal fluid (CSF). As we shall discuss in §1.2.2, brain edema occurs due to an accumulation of ISF in the tissue (Simard *et al.*, 2007). However the three fluid networks are closely interrelated, and the evolution and resolution of edema is affected by all three. Figure 1.2 illustrates schematically how fluid exchange occurs between these networks.

Blood enters the brain through arteries, circulates through the brain in capillaries, and then leaves through veins. Neurons have a high rate of metabolism, and therefore the capillary network in the brain is dense to ensure sufficient oxygen is supplied by diffusion: typically no cell is further than 50μm from a capillary (Nicholson, 2001). In most organs the capillary walls are fenestrated (or holey), allowing easy exchange of fluid and ions between blood and ISF. However neurons are very sensitive to their environment (Strange, 1973), and so a special protective layer ('the blood brain barrier', BBB) separates blood from tissue. The BBB consists of a continuous layer of endothelial cells and membranes (Abbott *et al.*, 2006). Substances (such as ions and proteins) cannot pass between endothelial cells due to tight junctions between adjacent cells. Therefore endothelial cells actively control substances crossing the BBB via ion pumps in their cell membrane, allowing the composition of the interstitial fluid surrounding neurons to re-

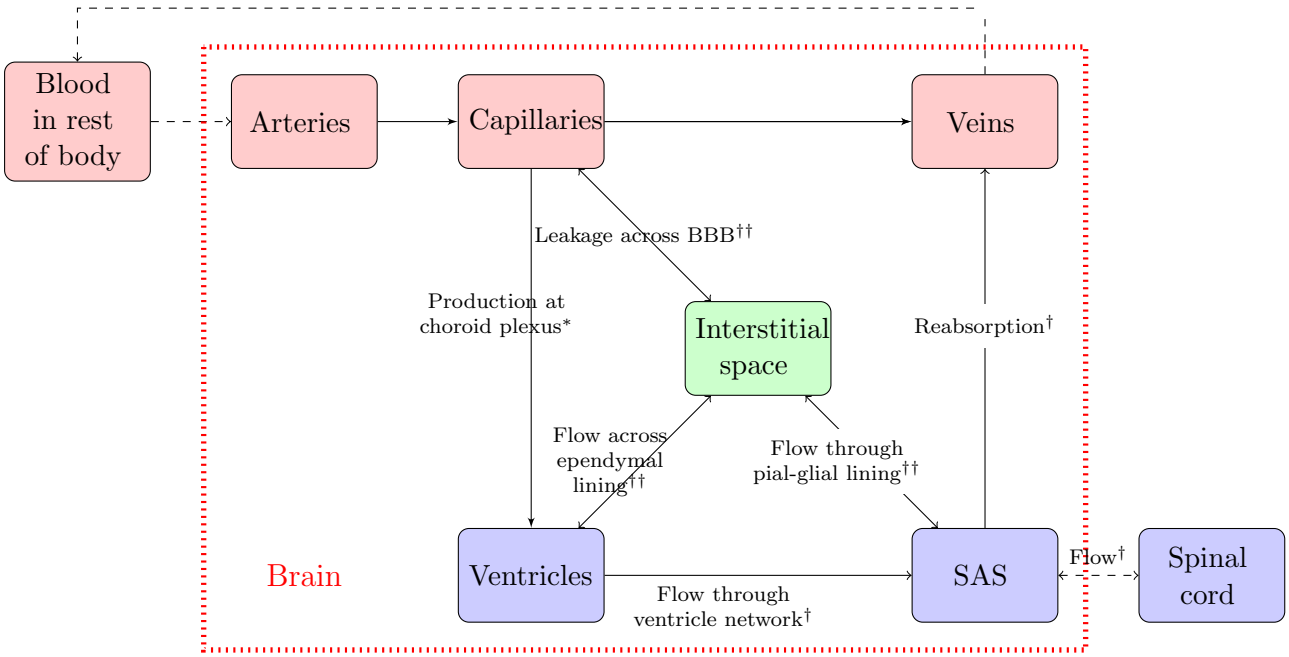

Figure 1.2: Diagram illustrating the relationships between the three fluid networks in the brain. Boxes represent fluid filled compartments, while arrows represent transfer of fluid between compartments. The fluids in the brain are blood (red), interstitial fluid (ISF) (green), and cerebrospinal fluid (CSF) (blue). Symbols on arrows indicate the processes that cause that particular fluid transfer: *active process, †driven by hydrostatic pressure gradients, ††driven by hydrostatic and osmotic pressure gradients. The composition of these fluids, and further descriptions of the flows between compartments, are discussed in §1.2.1.

main well controlled despite fluctuations in the concentration of substances in the blood (Abbott *et al.*, 2010).

A small amount of water is able to leak from capillaries into the ISF. However in the healthy brain this water flux is relatively low because the BBB is highly impermeable (Abbott, 2004). If the BBB is structurally damaged it becomes more permeable to fluid, which can in turn lead to edema, as additional fluid is able to enter the brain tissue across the BBB (and hence cause fluid accumulation and swelling). This is known as vasogenic edema, and is discussed further in §1.2.2.

CSF provides mechanical support for the brain, and helps with disposal of metabolic waste products (a similar role to the lymph system elsewhere in the body) (Johanson *et al.*, 2008). CSF is located within the ventricles, a series of connected compartments within the brain, and the subarachnoid space (SAS) that surrounds the brain (see Figure 1.3). The ventricles and SAS are connected by the aqueduct of Sylvius, allowing CSF to flow from the ventricles to the SAS. CSF is produced within the ventricles at the chorid plexus by an active process of transport from the blood (Brown *et al.*, 2004), and

circulates through the ventricle network to the SAS where it is reabsorbed into the veins. The SAS is connected to the spinal cord, and CSF can also move between the spinal cord and SAS under hydrostatic pressure gradients.

The CSF is separated from the ISF by the ependymal layer at the ventricle walls, and the pial layer at the SAS. Both the pial and ependymal layers allow free movement of water but may obstruct movement of larger molecules (Redzic *et al.*, 2005).

1.2.2 Biological causes of brain swelling

Brain tissue has been observed to swell following impact injury (Unterberg *et al.*, 2004), in the vicinity of a brain tumour (Papadopoulos *et al.*, 2004), and as a result of ischemia (inadequate blood supply) caused by stroke (Kahle *et al.*, 2009; Liang *et al.*, 2007; Simard *et al.*, 2007).

Figure removed due to copyright

Figure 1.3: Illustration of the location of CSF in the brain. Source: www.mayfield.com, accessed August 2014.

Brain swelling is caused by an accumulation of fluid that enters the tissue from cerebral capillaries (Unterberg *et al.*, 2004). The biological processes leading to tissue swelling are complex (see reviews Ayata and Ropper, 2002; Kimelberg, 1995; Marmarou, 2007; Nag *et al.*, 2009; Simard *et al.*, 2007; Unterberg *et al.*, 2004, for examples).

The flow chart in Figure 1.4 illustrates the sequence of processes which lead to brain edema, along with brief descriptions of the reason each change occurs. Here we explain these processes, with a focus on edema due to ischemic stroke. Other pathologies, such as impact injury (which damages cells and blood vessels), cause similar effects. The pathophysiological processes underlying ischemic tissue swelling have two stages: initial cytotoxic edema where individual cells swell, and subsequently vasogenic and ionic edema where the tissue itself swells due to an influx of water (Kimelberg, 1995).

Cytotoxic edema and cellular swelling

Within healthy brain tissue, the composition of intracellular fluid is controlled by cell membranes. Water and ions can pass through cell membranes due to both passive processes (driven by concentration and electrochemical gradients), and active processes (con-

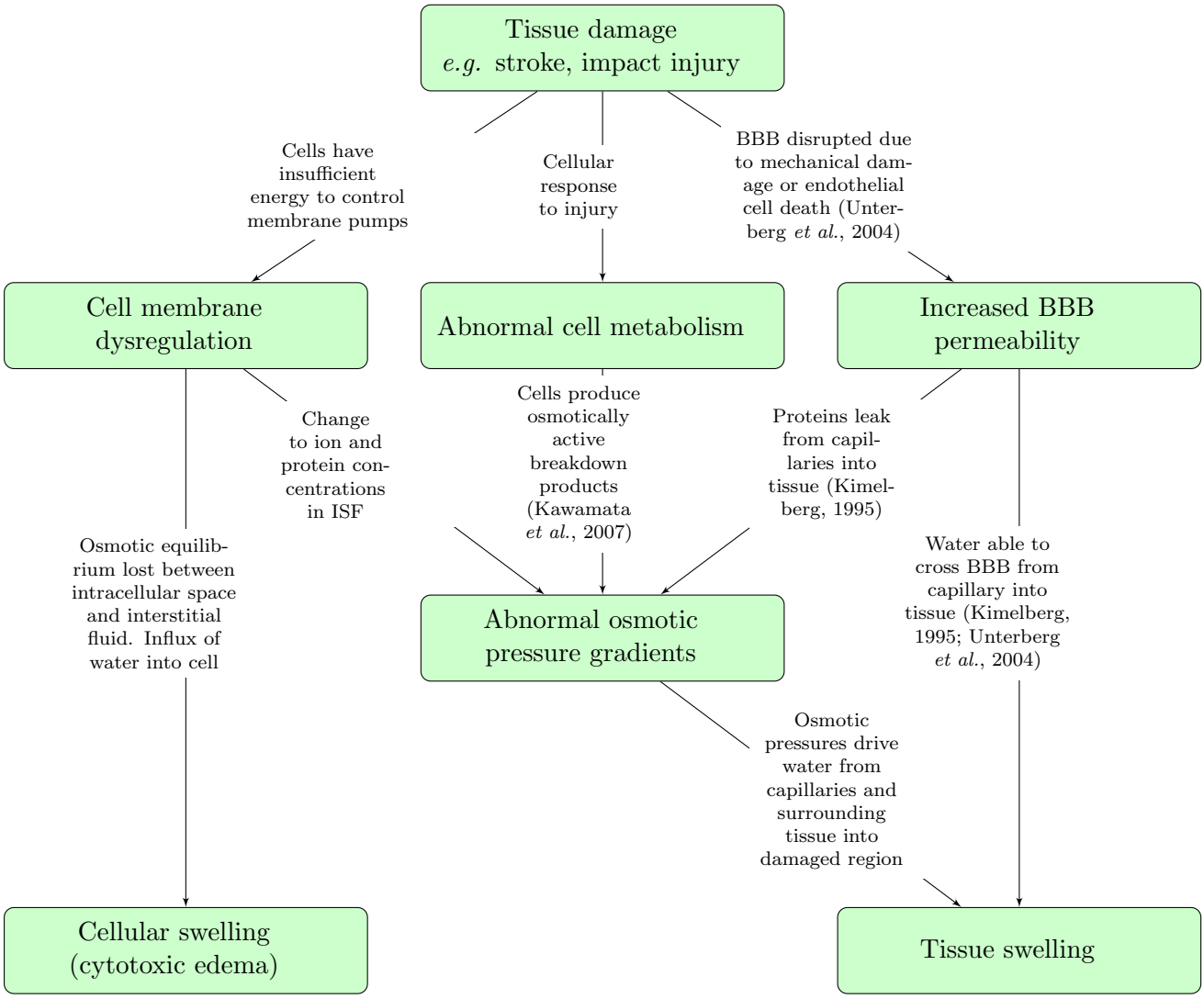

Figure 1.4: Diagram illustrating the processes that are believed to lead to brain tissue swelling following injury.

trolled by pumps in the cell membrane). These cell membrane pumps use energy to selectively move ions and substances across cell membranes, and allow cells to maintain concentration differences across their cell membranes. As water can pass freely through a cell membrane, cells maintain their volume by keeping in osmotic equilibrium with the interstitial fluid (McManus *et al.*, 1995).

Ischemia[1] causes brain tissue to receive insufficient oxygen. Due to the lack of oxygen, cells cannot produce enough energy to continue the active pumping across the cell membrane. In this case ions are able to move freely across the membrane in response to electrochemical potential gradients. This leads to a net influx of ions into the cell and

[1]Ischemia is defined as an inadequate blood supply to a region of tissue, and causes a shortage of oxygen.

subsequent water influx (hence cell swelling) as the cell is no longer in osmotic equilibrium with its surroundings. Some highly swollen cells may even burst, causing their contents to become merged with the interstitium (Simard *et al.*, 2007). Mathematical models for cytotoxic edema, which couple ion and protein concentrations and fluxes together with cell volume and water movement, have highlighted the importance of cell membrane pumps in maintaining an equilibrium cell volume (Leaf, 1959; Dronne *et al.*, 2006). We discuss these models in §1.5.

Although cytotoxic edema leads to the swelling and damage of individual cells, it is simply mass transfer between the extracellular and intracellular space and does not lead to overall swelling of the brain tissue (Liang *et al.*, 2007). However cytotoxic edema leads to changes in ion and protein concentration (and hence osmotic changes) of the interstitial fluid, which can provide a driving force for vasogenic edema and lead to bulk swelling.

Vasogenic edema and tissue swelling

Cytotoxic edema causes swelling of individual cells, but does not cause the tissue itself to swell. Here we describe how movement of water across the BBB can cause tissue scale swelling.

The blood brain barrier (BBB) controls movement of water and solutes from plasma to interstitial fluid. In the healthy brain, the BBB is impermeable to proteins and ions, and very slightly permeable to water. Therefore a small flux of water (of the order of μl/min) leaks from the capillaries, and drains by permeating through the brain tissue into the ventricles and SAS (Redzic *et al.*, 2005).

Since the BBB is comprised of a layer of cells, these cells can be damaged in ischemic tissue (due to the cytotoxic mechanism described above). Furthermore, impact injury can cause direct mechanical damage to the BBB (Unterberg *et al.*, 2004). When the BBB is damaged, it can become more permeable to water, ions, and proteins. When the BBB becomes more permeable to fluid, this fluid can cross the BBB from the vasculature and accumulate in the tissue. This is known as vasogenic edema.

Vasogenic edema is enhanced by the increased BBB permeability to plasma proteins, such as albumin (Simard *et al.*, 2007). The ISF usually contains proteins in low concentration (relative to blood plasma). If plasma proteins can cross the BBB they accumulate in the tissue interstitium, causing an increase in the osmotic pressure of the ISF. Furthermore, changes in the interstitial solute concentration caused by cytotoxic edema, abnormal cell metabolism (Kawamata *et al.*, 2007), or increased ion transport across the BBB (Kimelberg, 1995), may also lead to an increase in interstitial osmotic pressure. This increase in the interstitial osmotic pressure alters the pressure difference between the blood and ISF, providing a driving force for water influx, so that water moves from

surrounding tissue and across the newly permeable BBB into the damaged region (Ayata and Ropper, 2002; Kahle *et al.*, 2009).

In summary, brain tissue swelling occurs when water accumulates in response to osmotic pressure gradients. Brain tissue contains proteins, charged macromolecules, and ions: each of these species can contribute to osmotic pressure changes. The different types of edema usually coexist (Marmarou, 2007).

1.2.3 Consequences of edema

Consequences of swelling include stretching and tearing of brain tissue, which in turn damages the neurons and ultimately leads to a loss of brain function. Figure 1.5 shows an image of a rat brain after a stroke has been induced in the right hemisphere: we observe that large deformations occur in the brain tissue.

Deformation is particularly damaging to the brain because the axons, which connect neurons and allow chemical signals to propagate through the brain, are damaged by the stretching that is associated with swelling. The degree of damage depends on both the magnitude and rate of stretch, and numerous experimental studies have attempted to find thresholds of strain and strain rate that the brain can experience before axonal damage occurs (*e.g.* Bain and Meaney, 2000; Tang-Schomer *et al.*, 2010). The thresholds of damage given in the literature vary, perhaps due to the fact that different studies consider different measures of damage, strain rates, and tissue preparations.

Edema develops over the course of days (Hatashita *et al.*, 1988; Marmarou *et al.*, 2000), whilst experimental studies of axonal damage typically investigate much more rapid strain rates. For example, Bain and Meaney (2000) investigated two different measures of axonal damage, structural damage and electrophysiological impairment[2], by dynamically stretching (strain rates $30 - 60/\text{s}$) the optical nerve of pigs. They found that axons began to show signs of morphological damage at strains above 14%, and signs of electrophysiologial damage at strains above 13%, where this damage was measured shortly (< 1 hour) after stretch. Chung *et al.* (2005) stretched axon bundles between 1-6%, deforming them locally with high pressurised air for 20 ms; 72 hours after injury, they observed that 70% of the bundles contained broken axons.

Raised intracranial pressure (ICP) is another dangerous consequences of edema (*e.g.* Nag *et al.*, 2009; Unterberg *et al.*, 2004). A rise in ICP may impede blood flow to the brain, leading to a reduced oxygen supply. Healthy ICP is considered in the range 7-15mmHg, whilst ICP of 20mmHg and above is considered abnormal and may lead to

[2]Structural damage was assessed by measuring changes in neurofilament protein concentration in the axonal cytoskeleton, a signature of traumatic axonal damage, whilst electrophysiological impairment was assessed by measuring changes in electrical signal propagation

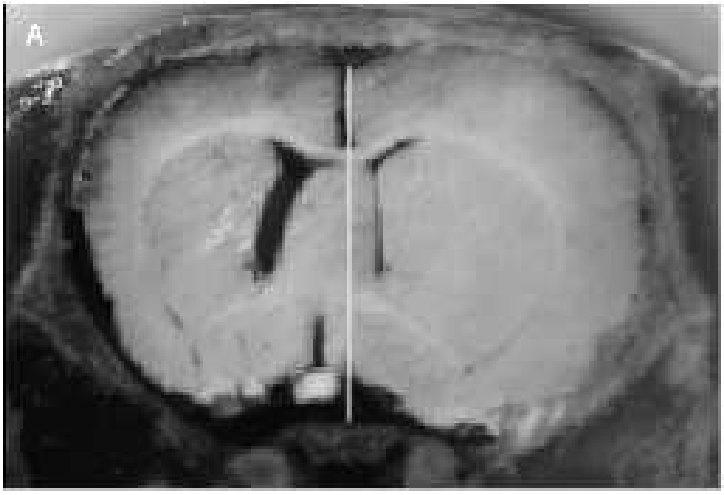

Figure 1.5: Image showing the deformation of a rat brain, after a stroke has been induced in the right hemisphere. A healthy brain would be symmetric about the white midline, but we observe that the right hemisphere has swollen. Reproduced with permission from Simard *et al.* (2007)

.

reduced cerebral blood flow (Czosnyka and Pickard, 2004). Following complete cessation of blood flow, cells cannot survive longer than 5-10 minutes without irreversible damage occurring (Astrup *et al.*, 1981).

There is also a dangerous feedback process associated with edema and raised ICP; local tissue edema leads to raised ICP and mechanical compression of surrounding tissue, leading to a reduction of cerebral blood flow and the spreading of ischemia into this surrounding tissue. Subsequently this surrounding tissue also becomes damaged and swells, and thus edema propagates through the brain (Gerriets *et al.*, 2004, 2009; Walberer *et al.*, 2008). In Chapter 5, we propose a mathematical model to investigate this propagation.

1.2.4 Treatment strategies

Two prominent treatment strategies for edema are the administration of osmotic agents, and surgical decompression (craniectomy) (Papadopoulos *et al.*, 2002). Treatment by osmotic agents involves raising the osmolarity of the blood (typically with mannitol), in order to reverse the osmotic gradient from plasma to ISF and hence draw water out of the tissue (Diringer and Zazulia, 2004). However, this cannot be used if the BBB has become permeable to solutes, as the solutes of mannitol will accumulate in brain tissue and further drive swelling.

In a surgical decompression, or craniectomy, a portion of the skull is removed to allow brain tissue to swell and relieve intracranial pressure (Soustiel *et al.*, 2010). The effectiveness of craniectomy is being investigated, as cohort studies indicate that whilst

intracranial pressure is decreased, a patient's long term functional outcome is decreased if a craniectomy is performed. It is thought that this may be because a craniectomy decreases intracranial pressure, yet increases tissue deformation (leading to axonal stretch) (Cooper *et al.*, 2011).

1.3 Mathematical modelling of the brain

In this section we review previous approaches that have been used to model both the mechanical behaviour of brain tissue and pathological disorders of the brain. We divide this section into parts for each of the modelling techniques that are commonly used for the brain: compartment based, elastic, viscoelastic, and mixture-based. We discuss both experimental evidence for these approaches, and additionally how these approaches have been applied to investigate various pathological conditions of the brain.

The brain has a complicated morphology. White and grey matter have different elastic properties, and the presence of bundles of neuronal axons in the white matter in particular give it a highly anisotropic structure. Additionally, experiments are performed on a wide variety of difference species, under different experimental protocols. Thus there is little consensus on the most appropriate modelling approach.

As we shall discuss in §1.5, edema has received comparatively little attention in the modelling literature. It is important therefore that we consider whether techniques originally applied to other pathologies may be useful to gain an understanding of edema. In particular, hydrocephalus and infusion tests are applications that have received much attention in the modelling literature, and share common features with edema. Hydrocephalus is a condition whereby CSF accumulates in the brain, causing expansion of the ventricles and deformation of the tissue. It can be caused by several mechanisms, including blockage of the aqueduct of Sylvius, excessive CSF production, or inhibited CSF absorption (see for example Linninger *et al.*, 2009; Kaczmarek *et al.*, 1997; Smillie *et al.*, 2005; Tully and Ventikos, 2011). Infusion is a procedure whereby fluid is injected into the brain. This may be done to inject drugs into the brain tissue, which can not enter from the vasculature as they are unable to cross the BBB, or to investigate the cerebral compliance of the brain (for example Basser, 1992; Wirth and Sobey, 2009; Chen and Sarntinoranont, 2007).

1.3.1 Compartment based models

Compartment models divide the brain into a series of fluid filled compartments, *e.g.* tissue, vasculature and ventricles. The governing equations are based upon conservation of

mass in each compartment, while fluid fluxes between connected compartments are driven by hydrostatic and/or osmotic pressure differences. These models have been used to investigate the onset of edema (Rapoport, 1997) (discussed further below), hypertension (Ursino, 1988) and hydrocephalus (Linninger *et al.*, 2009).

At the cellular level, compartment models for individual cell swelling (cytotoxic edema) have been investigated (Yi *et al.*, 2003; Dronne *et al.*, 2006). In these models, the flux of ions across the cell membrane is assumed to occur due to both passive (electrochemical) and active (cell membrane pumps) processes. Fluid moves across the cell membrane according to osmotic pressure gradients. When the action of ion pumps is reduced (as in cytotoxic edema) the osmotic concentration within the cell is predicted to increase, leading to water accumulation within the cell.

A major limitation of compartment models is that they do not allow for spatial variation within a compartment, so are unable to capture the spatial variation occurring across brain tissue that is of interest here. However they do provide useful quantitative description of the fluid flows within the brain, and offer insight into the consequences of changing key parameters (for example, Linninger *et al.* (2009) simulate hydrocephalus by reducing absorption of CSF, leading to CSF build up within the brain).

1.3.2 Elastic models

In the elastic modelling approach, brain tissue is represented by a single phase elastic material. Several different constitutive laws have been chosen in the literature.

Franceschini *et al.* (2006) performed low rate (5mm/min) uniaxial compression and extension tests on cylindrical and prismatic specimens of brain tissue. They found that a finite deformation Ogden model could fit the loading and unloading behaviour, although a 'pseudo-elastic' approach must be taken whereby different elastic parameters are required for the loading and unloading curves.

Rashid *et al.* (2012) performed rapid extension experiments (at strain rates $30-90/\mathrm{s}$), and fitted for the Fung, Gent and one term Ogden elastic models. They found that at each strain rate, each of the elastic models could be fitted to show good agreement with the observed behaviour. However a different set of elastic parameters had to be used at each strain rate, showing that brain tissue exhibits a stiffer response to higher strain rates. This experiment highlights that the rate of strain is important for brain tissue, and suggests that viscoelastic models might be appropriate so that the strain rate dependence can then be captured.

1.3.3 Viscoelastic models

Existing viscoelastic models represent brain tissue as a single phase continuum with time-dependent elastic parameters, allowing strain-rate dependent behaviour to be captured (Bilston, 2011). These models have been commonly applied to simulate rapid compression (Miller and Chinzei, 1997; Miller, 1999) or extension tests (Miller and Chinzei, 2002), and show good fit to experimental data over a range of strain rates.

For example, a viscoelastic model has been applied to the compression of brain tissue at strain rates relevant to surgical procedures (from 500-0.005mm/min) yielding good agreement with experimental results (Miller, 1999). However, it is not clear whether an elastic or biphasic model (see §1.3.4) could have equally well captured the behaviour observed at the lower end of these strain rates

Viscoelastic models are typically applied to rapid processes such as impact injury. For example, a viscoelastic model for a realistic geometry of the brain confined within a rigid skull was constructed by Zhang *et al.* (2004). The authors studied footage of accidents leading to brain injury in footballers, and simulated the responses of the brain tissue to such inputs with their model. This enabled them to predict the stress fields that had been caused in the brain due to the injury, and to construct injury thresholds.

As brain edema is observed to evolve over the course of days (Diringer and Zazulia, 2004), and viscoelastic models are typically applied to high strain rates, we shall not consider viscoelastic models further. In a similar approach, Taylor and Miller (2004) took the long-time limit of the time-dependent viscoelastic material parameters found by Miller (1999), to determine elastic parameters relevant to hydrocephalus. This approach yielded a Young's modulus of 584 Pa, which the authors claim to be relevant for deformations of the brain that are sufficiently slow that rate-dependent behaviour may be neglected.

1.3.4 Poroelastic and mixture-based models

Poroelastic and biphasic models represent brain tissue as a mixture of an elastic solid and interpenetrating fluid. These models explicitly consider the distribution of fluid within the tissue, and thus the movement of solid and fluid phases are coupled (for example, if both phases are incompressible then fluid must be displaced in order to achieve compression of the tissue).

Franceschini *et al.* (2006) provided the first experimental evidence that brain tissue does indeed behave as a biphasic material. They conducted compression tests on radially confined cylinders of brain tissue, where fluid was allowed to drain from the system at the top and bottom of the sample. They showed that brain tissue exhibits consolidation behaviour, whereby the tissue compresses as fluid seeps out. The authors also note that

there is further indirect evidence that brain tissue should be considered as a mixture of solid and fluid phases. For example, injecting a hyperosmotic solution into the cerebral vasculature (mannitol) does causes brain tissue to shrink as fluid is drawn out of the tissue, and brain swelling is associated with an increase in brain water content.

However, Miller (1997) warn that the biphasic approach is inherently unable to account for the viscoelasticity of the solid phase. It has been suggested that a viscoporoelastic model (consisting of a viscoelastic solid phase and interpenetrating fluid) may be necessary to capture both the strain-rate dependent behaviour and the biphasic nature of brain tissue (Kyriacou *et al.*, 2002). Fitting a viscoporoelastic model to unconfined compression of white matter at low strain rates (0.01, 0.001 and 0.0001/s) gave good agreement to experimental results for the stress-relaxation behaviour of the tissue, while a poroelastic model was able only to capture the long-time elastic response (Cheng and Bilston, 2007). However, we observe that even the slowest strain rate (0.0001/s) tested here is still much more rapid than the strain rates relevant to edema.

Poroelastic models have been used to investigate the causes of and treatment strategies for hydrocephalus. In this case, brain tissue is generally modelled by a two phase poroelastic or biphasic mixture of elastic solid and fluid, and the ventricles by fluid filled compartments. Hydrocephalus is driven by changing physical parameters in the system, for example reducing the diameter of the aqueduct of Sylvius (connecting the ventricles to SAS) to obstruct CSF flow (Smillie *et al.*, 2005; Sobey and Wirth, 2006), or impairing CSF absorption at the SAS or within the brain parenchyma (Levine, 1999; Smillie *et al.*, 2005). This causes the ventricles to expand, and the tissue to compress. Typically these models assume a spherically symmetric geometry for the brain, although three-dimensional models have also been considered (Wirth and Sobey, 2006).

Poroelastic models have also been used to investigate infusion tests, whereby a solution is injected into the brain tissue (Basser, 1992; García and Smith, 2009; Sobey *et al.*, 2012). Typically these models mimic infusion through the boundary conditions, by imposing a cavity of fixed pressure or a prescribed fluid flux into the tissue. Whilst it is acknowledged that injecting a solute into the brain may affect water movement, for example by increasing the osmotic force driving fluid across the BBB, in all of these models solutes are either neglected or assumed to be sufficiently dilute that they do not affect water movement (Chen and Sarntinoranont, 2007; Kalyanasundaram *et al.*, 1997). In the latter case the solute phase decouples from the solid/fluid phase, so that the model may initially be solved for the solid and fluid phases alone. Subsequently fluid movement feeds into the advective term for solute movement, from which the solute distribution may be calculated.

Extensions to the two phase approach include modelling the brain tissue as a multi-

network poroelastic model, where several fluid networks (representing interstitial fluid, arteries, capillaries and veins) are considered. This allows for fluid transfer between the vascular networks and interstitial fluid. Hydrocephalus driven by changes in the compliance of the vascular networks and breakdown of the BBB was investigated by Tully and Ventikos (2011).

An alternative extension is treating brain tissue as a triphasic mixture, where additional charged solute species are considered and the solid phase can have a net negative charge (to represent a fixed charge density). This approach has been used by Elkin *et al.* (2010) to investigate swelling of brain tissue slices (see §1.5), and also by Drapaca and Fritz (2012) to propose a novel mechanism for hydrocephalus, whereby tissue swelling is driven by changes in the ionic composition of the CSF.

1.4 Mixture-based approaches to soft tissue modelling

Mixture-based models have been used to model the behaviour of articular cartilage (Cowin and Doty, 2009; Holmes, 1985; Lai *et al.*, 1991; Mak *et al.*, 1987; Mow *et al.*, 1980) and other soft tissues (Gu *et al.*, 1999; Holmes and Mow, 1990) for several decades. Such models assume that the biological tissue in question may be modelled as a mixture of two or more phases: a porous, elastic solid matrix (representing the extracellular matrix and cells), an interpenetrating fluid phase (representing interstitial fluid) and may also include solute and ion species in solution.

Mixture-based models originate from the work of Truesdell (Rajagopal and Tao, 1995). The governing equations are derived from macroscale equations for the mass and momentum conservation of each phase, along with constitutive laws for the interaction forces between the phases (see Chapter 2). We note that the mixture-based modelling approach is distinct from the "multiphase" approach, for which the macroscale governing equations are obtained through averaging of the microscale governing equations for the behaviour of each phase (Davit *et al.*, 2013; Drew, 1983). Interactions between the phases are captured via the specification of constitutive laws. These multiphase models are also commonly utilised to model biological tissues (*e.g.* Byrne *et al.*, 2003; Lemon *et al.*, 2006; O'Dea *et al.*, 2012).

Poroelastic versus biphasic approaches

The simplest two-phase models for soft tissue incorporate just solid and fluid phases. When the solid phase is elastic there are two formulations of these models: poroelastic

and mixture-based. Poroelastic models originate from the field of soil mechanics and in particular the work of Biot and Terzaghi (Biot, 1941). These poroelastic models were originally derived from constitutive assumptions about the coupling between applied stress, pore pressure and volume changes for a fluid filled, porous, elastic medium, but have since also been obtained through homogenization theory (Burridge and Keller, 1981; Penta *et al.*, 2014).

Mixture-based models are known as biphasic models when only two phases are present. Biphasic models were originally derived by Mow *et al.* (1980) for application to articular cartilage. When the mixture is saturated and both solid and fluid phases are intrinsically incompressible, the poroelastic and biphasic models are equivalent (Simon, 1992).

Extension to triphasic models (with solutes)

There is greater precedent for incorporating additional solute species into biphasic rather than poroelastic models. Biphasic models have been extended to incorporate the presence of dilute concentrations of solutes dissolved in the fluid phase (Ateshian *et al.*, 2006; Gu *et al.*, 1999; Huyghe and Janssen, 1997; Lai *et al.*, 1991; Mauck *et al.*, 2003; Sun *et al.*, 1999). Models incorporating solid, fluid and solute species are typically known as triphasic models (or sometimes quadriphasic, where two charged ion species are present (*e.g.* Huyghe and Janssen, 1997)). These models often allow for a net charge of the solid phase, referred to as a Fixed Charge Density (FCD), which may be relevant to biological tissues when the ECM is composed of charged proteins. Triphasic models allow coupling between tissue deformation, fluid flux and solute movement due to both osmotic and hydrostatic pressure gradients.

The original triphasic model was produced by Lai *et al.* (1991). The model considered a mixture of an elastic solid, a saturating fluid and species of positive and negative ions; this mixture was then subject to infinitesimal deformations. To close the model, constitutive laws must be chosen for the drag between phases; solid-fluid and fluid-solute drag were chosen to be consistent with Darcy's law (for fluid flux through a porous medium) and Fickian diffusion respectively, whilst solute-solid and solute-solute drag were neglected relative to the solid-fluid and fluid-solute drag. This model was subsequently extended to multiple electrolytes (Gu *et al.*, 1999) and finite deformations (Huyghe and Janssen, 1997).

Mauck *et al.* (2003) generalised the multiple solute model to also allow for drag between solutes and the solid phase, allowing the presence of the solid phase to hinder solute movement; this approach has been applied to both uncharged (Ateshian *et al.*, 2006) and charged (Huang and Gu, 2007; Yao and Gu, 2007) solutes.

1.5 Previous modelling of brain edema

Few authors have specifically modelled the mechanical effects leading to edema. In this section we discuss in more detail the existing mathematical modelling literature, which primarily consists of compartment models and mixture-based models.

The first model of mathematical edema was proposed by Rapoport (1978). As mentioned above, Rapoport (1978) used a compartment model to represent the different fluids in the brain (*i.e.* blood, ISF, CSF). He proposed constitutive laws for the flux of fluid between each compartment. In particular, the flux between capillaries and the interstitial space was modelled according to the sum of the hydrostatic and osmotic pressure differences across the capillary membrane (Starling's law). Increasing either the hydraulic conductivity of the capillary to water, or the osmotic pressure difference across the membrane, allowed water to accumulate in the tissue.

Nagashima *et al.* (1990) used a biphasic model to investigate the formation and evolution of vasogenic edema, by imposing a diffuse source of fluid throughout the tissue (to represent a capillary source) and investigating the effect of an increase in capillary permeability on the water content of the brain. In Chapter 4, we shall consider a similar model. Whilst their simulations yield results for the evolution of edema that are broadly similar to the evolution seen experimentally, the parameters they use are not consistent with more recent literature and experiments. For example, they use a tissue hydraulic conductivity to water (Darcy coefficient) of 2×10^{-8} cm^3/mmHg/s $\approx 10^{-16}$ m^{3}Pa^{-1}s^{-1}, while more recent studies indicate that this parameter should take a value of 10^{-12} m^{3}Pa^{-1}s^{-1} (Cheng and Bilston, 2007; Smillie *et al.*, 2005).

Elkin *et al.* (2010) performed experiments to investigate the swelling of brain tissue slices. A triphasic model was fitted to experimental results for the change in volume of damaged brain tissue slices when submerged in ionic solution baths of different concentrations. It was observed that tissue slices swelled the most in dilute ionic solution baths, indicating that tissue swelling could be explained by the Donnan effect, whereby negative charges in the tissue induce an osmotic pressure between the tissue and solution bath. This work considers the behaviour of damaged brain tissue, but does not consider the transition from healthy to damaged tissue. In Chapter 3, we revisit the experimental results of Elkin *et al.* (2010) further, to propose a model explaining this transition.

1.6 Outline of this thesis

As discussed in §1.2.2, brain edema is driven by changes in ion and protein concentration, and BBB permeability, within the brain. Because mixture-based models offer a framework

to couple tissue deformation together with water accumulation (driven by hydrostatic and osmotic pressure gradients) and solute movement (driven by electrochemical gradients), we will use a mixture-based approach to model brain tissue.

In Chapter 2, we present and discuss the governing equations for a triphasic mixture. Through a series of case studies, we highlight the features of the triphasic model that are particularly relevant to the brain.

In Chapter 3, we focus on the swelling of *ex vivo* tissue slices. We use an equilibrium triphasic model to propose a theory to explain the experimental results of Elkin *et al.* (2010), who conducted experiments to investigate the effect of bathing solution ionic concentration on the swelling of tissue slices.

In Chapter 4, we use a biphasic model (a simplification of the triphasic model in the absence of solutes) to investigate the effect of BBB failure on brain edema. Our model is based on that of Nagashima *et al.* (1990), and we extend their approach by considering a finite deformation model and performing dimensional analysis of the system to identify which parameter groupings are key to tissue swelling.

In Chapter 5, we consider propagation of brain edema. We are interested to understand the experimental results of Walberer *et al.* (2008), who show that following ischemic stroke the final volume of damaged tissue is smaller if a craniectomy has been performed. We couple the damage mechanism from Chapter 3, exposure of intracellular FCD, along with oxygen transport in brain tissue, to propose an iterative model for damage propagation. We compare predictions for intact and craniectomy brains by imposing a no-displacement boundary condition in the former case, and allowing the tissue to swell outwards in the latter case.

Finally in Chapter 6, we conclude with a discussion of our results, the limitations of our modelling approach, and possible future directions.

Chapter 2

Mixture Based Models for Finite Deformation of Soft Tissue

2.1 Introduction

Many of the mechanical phenomena exhibited by the brain, particularly swelling, can be described by triphasic models. In this chapter we present a triphasic model, which will form the basis for much of the rest of this thesis. To gain a better understanding of this model, we will then interrogate features of the model that are relevant to the brain and tissue swelling in a series of case studies.

In §2.2 we present a triphasic model for a porous elastic solid saturated with a liquid that contains multiple solutes. Our approach combines those of Mauck *et al.* (2003) who present a triphasic model for multiple uncharged solutes allowing for friction between the solid and solute phases, and Gu *et al.* (1999) who present a triphasic model for multiple charged ion species where friction between the ions and solid phases is neglected.

Our first case study, in §2.3, applies the triphasic model to the free swelling of a charged mixture in a bath of ionic solution. The focus here is on the great variety of constitutive laws chosen to represent the elastic behaviour of brain tissue in previous models. We discuss the sensitivity of the behaviour to the choice of constitutive law in this simple problem.

It has been proposed that the hydraulic permeability of brain tissue is altered in the course of edema. The permeability may increase in the core of the swollen region due to expansion of the extracellular space (Fenstermacher and Patlak, 1976), and decrease in the region surrounding the core due to compression or cellular swelling (Katayama and Kawamata, 2003). In a second case study (§2.4) we consider the compression of a biphasic mixture to investigate different constitutive laws for permeability that have been purposed for soft tissue modelling. A biphasic mixture model is a simplification

of the triphasic mixture model, in the absence of solute species, and we consider this here to highlight the properties of the mixture associated with compressibility. We show that appropriate constitutive laws may be incorporated into the model to capture this deformation-dependent permeability, and highlight the importance of choosing physically realistic constitutive laws to describe mixture properties.

The third case study investigates the fact that the formation and resolution of brain tissue swelling may be caused by osmotic gradients across the blood brain barrier (Kimelberg, 1995; Simard *et al.*, 2007), and hydrostatic pressure and osmotic gradients within the tissue itself (Kawamata *et al.*, 2007; Reulen *et al.*, 1977). In §2.5 we demonstrate the features of the triphasic model that allow solute concentrations to cause osmotic pressure gradients, and hence drive fluid movement and tissue deformation. Understanding the parameters controlling osmotic effects gives insight into the biological changes that are able to drive tissue swelling in the brain.

2.2 A Triphasic Model

Figure 2.1 illustrates the phases of a triphasic model for soft tissue. In this section we present a triphasic model for a mixture of porous elastic solid, solvent and solutes.

In the literature, the triphasic model has been derived from thermodynamic considerations, allowing it to be shown that the momentum equations are consistent with the laws of thermodynamics (Cowin and Doty, 2009; Huyghe and Janssen, 1997; Lai *et al.*, 1991). Here we state the governing equations that follow directly from the principles of mass and momentum conservation, and refer the reader to these references for the thermodynamic approach.

2.2.1 Definition of variables

We consider a mixture of $2 + N$ phases: a porous elastic solid (s), interstitial solvent (w), and N charged solutes ($i = 1, \ldots, N$). Each phase is assumed to be inherently incompressible, and the solute concentrations are assumed to be low (so that the solutions are dilute). The solid phase has a net charge, referred to as the Fixed Charge Density (FCD) (f).

Let ϕ^i denote the volume fraction of each phase, where $i = s, w, 1, \ldots, N$. We define ρ^i to be the density of each phase **per volume of tissue** so that,

$$\rho^i = \phi^i \rho^i_T, \qquad\qquad i = s, w, 1, \ldots, N, \tag{2.1}$$

where ρ^i_T is the true density of each phase. As the phases are assumed to be intrinsically

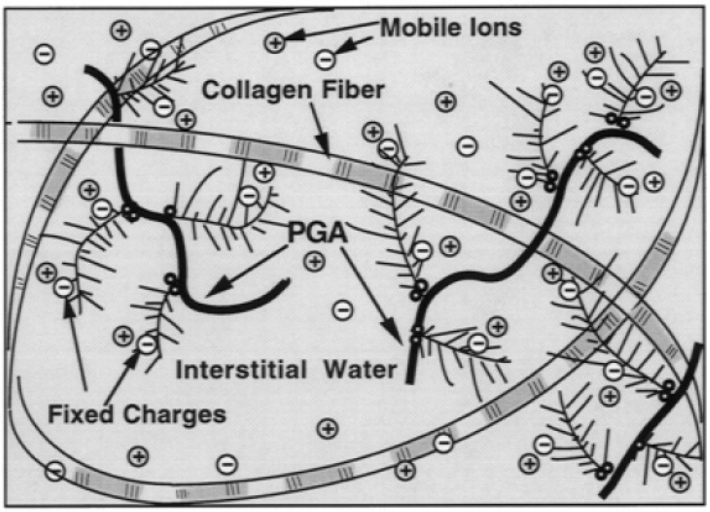

Figure 2.1: An illustration of the phases considered in the triphasic model when applied to articular cartilage. The tissue is treated as a mixture of phases: elastic solid, fluid, and solutes (in this case, positive and negative ions). The solid phase has a net negative charge due to the presence of fixed charges (referred to as the Fixed Charge Density (FCD)). Reproduced with permission from Sun *et al.* (1999).

incompressible and homogeneous, each ρ_T^i is a constant parameter. For each solute species we define z^i as the valence (charge per molecule), and the phase concentration c^i as the number of moles **per fluid volume** so that,

$$\rho^i = M^i c^i \phi^w, \qquad i = 1, \ldots, N \tag{2.2}$$

where the parameter M^i is the molar mass of species i. Each of the solid, solvent and solute phases is mobile, with velocity denoted $\mathbf{v^i}$. The FCD is defined as the density of charge associated with the solid phase **per fluid volume**, denoted c^f, and the FCD has a negative charge. As the FCD represents the charge of the solid phase, the velocity of the FCD is equal to that of the solid phase, $\mathbf{v^s}$.

Further variables are defined to represent the mechanical and electrical properties of the mixture. The pore pressure is denoted by p, the electric potential ξ, and the mixture Cauchy stress $\boldsymbol{\sigma}$. The electrochemical potentials of the solvent and solute phases are denoted μ^i, $i = w, 1, \ldots, N$.

Tissue deformation is determined by the displacement of the solid phase. The tissue is described in the (stress free) reference configuration by the material coordinates $\mathbf{X}$, and after deformation is described by new coordinates $\mathbf{x} = \boldsymbol{\chi}(\mathbf{X}, t)$ (referred to as the

current configuration). The tissue displacement $\mathbf{u}$ is given by the change in position,

$$\mathbf{u} = \mathbf{x} - \mathbf{X}. \tag{2.3}$$

The deformation gradient tensor is defined as,

$$\mathbf{F} = \frac{\partial \boldsymbol{\chi}}{\partial \mathbf{X}} = \mathbf{I} + \frac{\partial \mathbf{u}}{\partial \mathbf{X}}, \tag{2.4}$$

and $J = \det(\mathbf{F})$ represents the local change in volume due to deformation. The strain tensor $\mathbf{E}$ gives a measure of the strain due to a deformation,

$$\mathbf{E} = \frac{1}{2}\left(\mathbf{F}^{\mathbf{T}} \cdot \mathbf{F} - \mathbf{I}\right). \tag{2.5}$$

We have two sets of spatial coordinates: the Eulerian (current) coordinates $\mathbf{x}$ and Lagrangian (reference) coordinates $\mathbf{X}$. Throughout, it should be assumed that we refer to the current coordinates unless the notation explicitly refers to the reference coordinates. Hence ∇ refers to spatial derivatives with respect to the current coordinates (*i.e.* $\nabla = \partial/\partial x^i \otimes \mathbf{e}_i)$) whilst $\nabla_X = (\partial/\partial X^i \otimes \mathbf{E}_i)$ refers to derivatives with respect to the reference coordinates, where $\mathbf{e}_i$, $\mathbf{E}_i$ are bases in the current and reference configurations respectively. Similarly, we use $\partial/\partial t$ to denote the partial derivative in time with the current coordinates fixed (*i.e.* $\partial/\partial t = \partial/\partial t|_{\mathbf{x}}$), and $\partial/\partial t|_{\mathbf{X}}$ to denote the partial derivative in time with the reference coordinates fixed. The chain rule shows that the partial derivatives with respect to time are related by,

$$\left.\frac{\partial}{\partial t}\right|_{\mathbf{X}} f(\mathbf{x}(\mathbf{X}, t), t) = \left.\frac{\partial f}{\partial t}\right|_{\mathbf{x}} + \mathbf{v}^s \cdot \nabla f, \tag{2.6}$$

where $f(\mathbf{x}, t)$ is an arbitrary scalar function.

As the mixture displacement $\mathbf{u}$ is defined relative to the solid phase, the solid phase velocity $\mathbf{v}^s$ and displacement are related,

$$\mathbf{v}^s = \left.\frac{\partial}{\partial t}\right|_{\mathbf{X}} \mathbf{u}, \tag{2.7}$$

so that the solid velocity is the convective derivative over time of the displacement.

2.2.2 Governing equations

The triphasic model is obtained by considering mass balance, and momentum conservation for each of the phases.

Dilute approximation

We assume that the mixture is saturated ($\sum_{s,w,1,\ldots,N} \phi^i = 1$), and the solutes are in dilute solution (so that $\sum_{i=1,\ldots,N} \phi^i$ may be neglected in comparison to ϕ^s, ϕ^w). In the dilute approximation, we therefore have a simplified saturation condition,

$$\phi^w + \phi^s = 1. \tag{2.8}$$

Mass conservation

As each species is assumed to be intrinsically incompressible, the conservation of mass for each phase gives,

$$\frac{\partial \phi^i}{\partial t} + \nabla.(\mathbf{v}^i \phi^i) = Q^i, \qquad\qquad i = s, w, 1 \ldots N. \tag{2.9}$$

where $\mathbf{v}^i$ is the velocity of the ith phase, and Q^i is the rate at which volume of phase i is added per unit volume of mixture per unit time, representing a source or sink.

Solute quantities are typically tracked by concentration rather than volume fraction. To rewrite (2.9) in terms of concentration we substitute in the relations between concentration, density and volume fraction (2.1), (2.2) and find,

$$\frac{\partial \phi^w c^i}{\partial t} + \nabla.(\mathbf{v}^i \phi^w c^i) = q^i, \qquad\qquad i = 1 \ldots N. \tag{2.10}$$

where $q^i = Q^i \rho^i_T / M^i$ is a rescaled source term representing the number of moles of species i added per volume of mixture, per unit time.

From the saturation condition (2.8) and mass balance (2.9) for the solid and water phases, we obtain a continuity equation for the mass of the mixture,

$$Q^s + Q^w = \nabla.\left(\phi^s \mathbf{v}^s\right) + \nabla.\left(\phi^w \mathbf{v}^w\right) = \nabla.\mathbf{v}^s + \nabla.\mathbf{q}^w \tag{2.11}$$

where $\mathbf{q}^w := \phi_w(\mathbf{v}^w - \mathbf{v}^s)$ is defined as the solvent flux. This conversion allows us to track solvent movement relative to the solid phase, rather than considering the solvent velocity explicitly.

Since the solid phase is incompressible, mass conservation of the solid phase (2.9 for $i = s$) can equivalently be written in term of the deformation. In the absence of a solid source term ($Q^s = 0$), we find that

$$\phi^s = \frac{{\phi^s}_{(0)}}{J}. \tag{2.12}$$

where ${\phi^s}_{(0)}$ is defined as the volume fraction of solid in a stress free reference state. By taking the partial derivative of equation (2.12) with respect to time, it can be shown that equations (2.9 for $i = s$) and (2.12) are equivalent.

Additionally we consider conservation for the FCD. The FCD is attached to the solid phase and thus,

$$\frac{\partial \phi^w c^f}{\partial t} + \nabla.(\mathbf{v}^s \phi^w c^f) = 0. \tag{2.13}$$

Mass conservation of the FCD can equivalently be expressed in terms of the deformation, J, as

$$c^f = \frac{{\phi^w}_{(0)} {c^f}_{(0)}}{J\phi^w}. \tag{2.14}$$

where ${\phi^w}_{(0)}$, ${c^f}_{(0)}$ are the volume fraction of water and the FCD in a stress free reference state respectively.

Mixture momentum balance

Neglecting body forces and inertia, momentum balance for the mixture takes the form

$$\nabla \cdot \boldsymbol{\sigma} = \mathbf{0} \tag{2.15}$$

where $\boldsymbol{\sigma}$ is the mixture Cauchy stress tensor.

In mixture-based models, the mixture stress $\boldsymbol{\sigma}$ is divided into two components: the pore pressure p and the effective stress $\boldsymbol{\sigma}_e$ (arising from the elastic behaviour of the matrix) (Lai *et al.*, 1991; Mak *et al.*, 1987). Thus [1],

$$\boldsymbol{\sigma} = -p\mathbf{I} + \boldsymbol{\sigma}_e. \tag{2.16}$$

The effective stress $\boldsymbol{\sigma}_e$ is obtained from a strain energy function for the mixture, which we denote $W(\mathbf{F})$,

$$\boldsymbol{\sigma}_e = \frac{1}{J}\mathbf{F} \cdot \frac{\partial W}{\partial \mathbf{F}}, \tag{2.17}$$

[1] We note that in the poroelastic formulation of the mixture theory, the mixture stress is similarly written as a sum of two components, $\boldsymbol{\sigma} = -\alpha p\mathbf{I} + \boldsymbol{\sigma}_e$, where now there is an additional parameter α, the Biot-Willis parameter, preceding the pressure term (Detournay and Cheng, 1999). Physically, α represents the ratio of the fluid volume change to the bulk volume change, when the pore pressure remains constant (Wang, 2000). For the set-up which we consider, *i.e.* saturated mixtures where all phases are inherently incompressible, $\alpha = 1$.

where $[\partial W/\partial \mathbf{F}]_{ij} := \partial W/\partial F_{ji}$. A constitutive law must be chosen for the strain energy function $W(\mathbf{F})$; the effect of this choice is discussed further in §2.3.

Momentum balance for mobile species

Each of the solvent and solute phases ($i = w, 1 \dots N$) is associated with an electrochemical potential representing the energy per unit mass of that phase. The gradient of the electrochemical potential of each phase provides the driving force for its movement, and is balanced by friction between phases (Katchaslsky and Curran, 1974). Thus,

$$-\rho^i \nabla \mu^i = \sum_{j \neq i} f_{ij}(\mathbf{v}_i - \mathbf{v}_j), \qquad i = w, 1 \dots N, \qquad j = s, w, 1 \dots N, \tag{2.18}$$

where f_{ij} are the friction coefficients between the ith and jth phases. To close the system, constitutive equations must be posed for the friction coefficients and electrochemical potentials; see §2.2.3.

Electroneutrality

We assume that each point in the mixture is electroneutral, *i.e.* there is no net charge at any point or

$$\sum_{i=1}^{N} z_i c_i = c^f, \tag{2.19}$$

where we recall that the FCD refers to a negative charge. The electroneutrality constraint is an approximation to Gauss's law for the electric field, and is valid for lengthscales greater than the Debye length (which is of the order of nanometres for electrochemical solutions) (see Dickinson *et al.*, 2011, for example).

Summary of the full equations

In Table 2.1 we summarise the variables comprising the triphasic model. In total, there are $2N+9$ variables; in order that the system is closed we must therefore also have $2N+9$ governing equations. These comprise:

- relationship between solid velocity and displacement (2.7)
- dilute approximation to the saturation conditions (2.8)
- $N + 3$ mass conservation equations (2.10, 2.11 2.12 2.14)
- mixture momentum balance (2.15)
- constitutive law for the effective stress (2.17)

- $N+1$ momentum equations for mobile phases (2.18)
- electroneutrality constraint (2.19)

These governing equations must be considered along with appropriate initial and boundary conditions.

At this stage, we have presented a full set of governing equations for the triphasic mixture, but have yet to discuss constitutive laws for the electrochemical potentials μ_i, friction coefficients f_{ij}, or strain energy function W. In §2.2.3 we shall discuss these constitutive laws, and subsequently in §2.2.4 we simplify the governing equations to eliminate several variables and write the equations in a form that offers physical insight into the behaviour of the system.

Table 2.1: Summary of the variables involved in the triphasic mixture theory model.

ϕ^i	Volume fraction of phase i (i=w, s)	c^i	Concentration of phase i (i=$1 \dots N$)
c^f	FCD (fixed charge density)	ξ	Electrochemical potential
$\mathbf{v}^i$	Velocity of phase i (i=$w, s, 1 \dots N$)	$\mathbf{u}$	Solid displacement
p	Pore pressure	$\boldsymbol{\sigma}_e$	Mixture effective stress

2.2.3 Constitutive laws

(Electro)chemical potentials

The electrochemical potentials for the solutes and solvent are taken from the standard result for dilute electrolytic solutions (Atkins, 2006)

$$\mu^i = \mu_0^i + \frac{RT}{M^i} \ln\left(\gamma^i c^i\right) + \frac{z^i F \xi}{M^i}, \qquad i = 1 \dots N, \tag{2.20}$$

$$\mu^w = \mu_0^w + \frac{1}{\rho_T^w} \left(p - \Phi RT \sum_{i=1}^{N} c^i \right), \tag{2.21}$$

where z^i, M^i are the valence and molar mass of species i respectively, $\mu_0^i$and μ_0^w represent reference values of the electrochemical potential, and R, T and F are the ideal gas constant, temperature and Faraday constant respectively. The coefficient γ^i is the activity coefficient of solute i, and Φ is the osmotic coefficient of the solvent; both these constants are unity in an ideal solution.

An ideal solution obeys Raoult's law: the vapour pressure of the solution is equal to the weighted pure vapour pressure of each component. This occurs where the intermolecular forces between any two molecules in the mixture (whether the same or different species) are equal. In reality, dilute solutions and solutions comprised of similar molecules are close to ideal (Atkins, 2006). From herein we assume ideal solutions, *i.e.* that $\gamma^i =$

1, $\Phi = 1$, which simplifies the governing equations considerably whilst capturing the essential physical effects (Donnan, 1924).

Friction coefficients

Physically the friction coefficients f_{ij} represent the resistance to movement of phase i caused by phase j. By Onsager's Law, the friction coefficients are symmetric (Gu *et al.*, 1993; Katchaslsky and Curran, 1974),

$$f_{ij} = f_{ji} \qquad\qquad i, j = s, w, 1 \dots N. \tag{2.22}$$

In mixture theory, solute-to-solute drag is neglected (Ateshian *et al.*, 2006; Huyghe and Janssen, 1997) so that

$$f_{ij} = 0 \qquad\qquad i, j = 1 \dots N. \tag{2.23}$$

The original formulations of mixture theory considered only small ionic solutes. Then solute-to-solid drag was also neglected (Huyghe and Janssen, 1997; Lai *et al.*, 1991; Gu *et al.*, 1999; Sun *et al.*, 1999), *i.e.* the presence of the solid phase was assumed to offer negligible resistance to the movement of solutes. While this is natural for small solutes, Mauck *et al.* (2003) proposed that solute-solid drag should not be neglected for larger solutes. They therefore define two diffusion coefficients for each solute: D_0^i being the diffusion coefficient for the ith solute species in a pure solvent, whilst D^i is the diffusion coefficient for the solute in the solid-solvent mixture. The friction coefficients are then defined as (Ateshian *et al.*, 2006; Mauck *et al.*, 2003; Yao and Gu, 2007),

$$f_{iw} = \frac{RT\phi^w c^i}{D_0^i}, \qquad f_{iw} + f_{is} = \frac{RT\phi^w c^i}{D^i}, \qquad i = 1 \dots N. \tag{2.24}$$

We observe that if $D^i = D_0^i$ (*i.e.* the diffusion coefficient of a solute is the same in the mixture as pure solvent) then $f_{is} = 0$. In this case, solute-solid drag is indeed neglected and the governing equations reduce to the original formulation for small ionic solutes. As we are aiming to present a general formulation of mixture theory, and it has been observed that diffusion of large solutes is hindered in brain tissue (Nicholson and Phillips, 1981), we retain the effect of solute-solid drag.

The friction coefficient between fluid and solid is taken to be inversely related to the hydraulic permeability k of brain tissue,

$$f_{sw} = \frac{\left(\phi^w\right)^2}{k}. \tag{2.25}$$

where k ($\mathrm{m^2Pa^{-1}s^{-1}}$) is the Darcy coefficient for pure solute moving through the porous solid (Sun *et al.*, 1999).

2.2.4 Summary of the system

We now combine the expressions for the friction coefficients (2.22)-(2.25) and constitutive laws for electrochemical potentials (2.20)-(2.21) into the momentum conservation equations (2.18) for the solute and solvent phases. This yields transport equations for the solute and solvents that provide more physical intuition into the behaviour of the system. Finally we perform a variable and equation count to summarise which equations are necessary to define a closed system.

Transport equations

Rearranging the momentum balance equations (2.18) and substituting for the friction coefficients (2.22)-(2.25) and electrochemical potentials (2.20)-(2.21) yields an expression for the flux of solvent, relative to the solid matrix,

$$\mathbf{q}^w := \phi^w(\mathbf{v}^w - \mathbf{v}^s) = -K\left[\nabla p - \sum_{i=1\ldots N}\left[RT\left(1 - \frac{D^i}{D_0^i}\right)\nabla c^i + \frac{D^i}{D_0^i}z^i c^i \nabla\xi\right]\right] \tag{2.26}$$

where K is defined by,

$$\frac{1}{K} = \frac{1}{k} + \frac{RT}{\phi^w}\sum_{i=1\ldots N}\left(1 - \frac{D^i}{D_0^i}\right)\frac{c^i}{D_0^i}. \tag{2.27}$$

and represents the Darcy hydraulic permeability of the mixture to the solvent and solute mixture, whilst k represents the Darcy hydraulic permeability to pure solvent (Ateshian *et al.*, 2006).

Equation (2.26) shows that solvent flux is driven by pressure gradients, osmotic pressure gradients, and electric potential gradients (the latter is a consequence of drag between solvent and the charged solutes that move under an electric field). We observe that in the absence of solutes ($c^i = 0$), equation (2.26) reduces to Darcy's law for flow through a porous media. Additionally, equation (2.26) also reduces to Darcy's law for uncharged solutes ($z^i = 0$) in the absence of solute-to-solid drag ($D^i = D_0^i$): this suggests that the presence of solutes will affect solvent movement only if they are charged or cannot flow freely through the mixture.

A similar process of rearranging the momentum balance equations (2.18) and substituting for friction coefficients (2.22)-(2.25) and electrochemical potentials (2.20)-(2.21)

also yields a transport equation for the solutes,

$$\phi^w c^i \mathbf{v}^i = -\phi^w D^i \left(\nabla c^i + \frac{z^i c^i}{RT} \nabla \xi \right) + \phi^w c^i \left(\mathbf{v}^s + \frac{D^i}{D_0^i} \left(\mathbf{v}^w - \mathbf{v}^s \right) \right), \quad i = 1 \dots N. \quad (2.28)$$

This can now be substituted into mass conservation equations (2.10) to yield transport equations for the solute phases,

$$\frac{\partial \phi^w c^i}{\partial t} = \nabla . \left[\phi^w D^i \left(\underbrace{\nabla c^i}_{\text{diffusion}} + \overbrace{\frac{z^i c^i}{RT} \nabla \xi}^{\text{electric}} \right) - \underbrace{\phi^w c^i \left(1 - \frac{D^i}{D_0^i} \right) \mathbf{v}^s - \phi^w c^i \frac{D^i}{D_0^i} \mathbf{v}^w}_{\text{advection}} \right] + \overbrace{q^i}^{\text{source}}, \quad i = 1 \dots N \quad (2.29)$$

The above equation shows that solute movement is governed by four effects: diffusion, electric field, advection (due to movement of both the solid and fluid phases), and the presence of a source.

When $D^i = D_0^i$ then solid-solute drag is neglected and the governing equations reduce to the original mixture theory formulation (Gu *et al.*, 1999). In this case, equation (2.29) is equivalent to the Nernst-Planck equation for ions in a dilute solution subjected to an electric field (see p.384 of Truskey *et al.*, 2010, for example). We shall discuss the physical meaning of the ratio D^i/D_0^i further in §2.5.

Equation and Variable Count

At this point we summarise the reduced system. The system now has $5 + N$ variables, where N is the number of solute species considered: the solid displacement $\mathbf{u}$, solid velocity $\mathbf{v^s}$, fluid flux $\mathbf{q}^w := \phi_w(\mathbf{v}^w - \mathbf{v}^s)$, fluid pressure p, electric potential ξ, and solute concentrations c^i $(i = 1 \dots N)$. The $5 + N$ equations defining the model are the relation between solid displacement and velocity (2.7), the mixture stress balance (2.15), the mixture mass balance (2.11), fluid flux equation (2.26), electroneutrality constraint (2.19), along with N transport equations for the solutes (2.28).

All of the other variables that feature in these $N + 5$ equations can be expressed directly in terms of the variables listed above. The deformation gradient tensor $\mathbf{F}$ may be computed from the solid displacement $\mathbf{u}$ (equation (2.4)), and the stress tensor $\boldsymbol{\sigma}_e$ is also a function of $\mathbf{u}$ (depending upon the constitutive law chosen for the strain energy function (2.17)). The solid volume fraction ϕ^s and FCD c^f are dependent upon $J = \det \mathbf{F}$ due to the mass conservation constraints (2.12, 2.14), and the fluid volume fraction can subsequently be found from the saturation constraint (2.8).

The diffusion coefficient D^i for each solute, and permeability K, may be deformation

dependent. For example, if the mixture is stretched then the pores will expand, and this may make it easier for solvent to flow through the mixture. In particular, the permeability of brain tissue is observed to change due to edema (Fenstermacher and Patlak, 1976), and we shall discuss constitutive laws for deformation-dependent permeability K in §2.4.3.

These equations must be solved in a defined geometry together with appropriate boundary and initial conditions. In §2.3-§2.5 we explore applications of this model to some simple situations chosen to reveal aspects of the model of particular relevance to brain mechanics. The boundary conditions and geometry used will be problem dependent. Before moving onto this, however, we first consider the effect of linear vs. non-linear elasticity.

2.2.5 Finite vs. Infinitesimal Deformations

The triphasic and biphasic theories are often formulated for linear elasticity, which is strictly valid only for infinitesimal deformations. In linear elasticity it is assumed that the displacement $\mathbf{u}$ is small compared to any other length scale, and this means that at leading order the reference configuration, $\mathbf{X}$, and the current configuration, $\mathbf{x}$, are the same (Howell *et al.*, 2009). This assumption is commonly used to model articular cartilage, which is stiff and undergoes only small deformations (Lai *et al.*, 1991; Sun *et al.*, 1999).

The small displacement assumption simplifies the governing equations, because the partial derivative of the displacement with respect to time (used to obtain the solid velocity (2.7)) is no longer in a different coordinate system to the derivatives in the other governing equations. Additionally the leading order strain tensor $\mathbf{e}$ becomes a linear function of the displacement, namely,

$$\mathbf{e} = \frac{1}{2}\left(\nabla\mathbf{u} + \nabla\mathbf{u}^T\right) \tag{2.30}$$

and for a homogeneous, isotropic material the general form of the effective stress tensor is also linear,

$$\boldsymbol{\sigma}_e = \lambda_s \mathrm{tr}(\mathbf{e})\mathbf{I} + 2\mu_s\mathbf{e} \tag{2.31}$$

where λ_s and μ_s are the first Lamé parameters.

As edema can cause the brain to undergo large strains (see Figure 1.5), we consider finite deformations in this Chapter. In §4.3.2 of Chapter 4, we shall compare the results of infinitesimal and finite deformation models for a biphasic system, where brain swelling is driven by changes in BBB permeability.

2.3 Elasticity: Swelling in an ionic solution bath

In this section, we investigate equilibrium swelling of an isotropic and homogeneous cube of tissue submerged in a bath of ionic solution. We use this (homogeneous) model problem to determine the effect of the many constitutive laws that have been suggested to capture the mechanical behaviour of brain tissue in a poroelastic or mixture-based framework (for example Elkin *et al.*, 2010; García and Smith, 2009). This allows us to understand the influence of the choice of strain energy function on the model predictions.

We consider the general triphasic mixture described in §2.2 for the case where the solid phase has a negatively charged FCD, and there are only two solute species: monovalent positive ions (+) and monovalent negative ions (−). This is the simplest system that captures the free swelling behaviour of a triphasic mixture. The tissue swells because the presence of a charged FCD induces an ionic concentration difference between the mixture and solution bath, an effect known as the Donnan effect (Donnan, 1924). This causes an osmotic pressure difference between the mixture and bath, driving fluid into the mixture, swelling it and causing it to deform (Cowin and Doty, 2009; Lai *et al.*, 1991).

In Chapter 3 we shall explore the Donnan effect further and compare our model results with experimental results for swelling of brain tissue slices (Elkin *et al.*, 2010). The slices used experimentally were cuboids; we therefore use a cuboidal geometry here for consistency between chapters.

2.3.1 Free swelling: Geometry and boundary conditions

We consider a cuboid of tissue submerged in a bath of ionic solution, as illustrated in Figure 2.2. The bath is assumed to be well mixed and maintained at a constant ionic concentration. We denote the pressure in the bath by p^*, and total ionic concentration of the bath by c^* (so that the concentration of each species of ions (positive and negative) is $c^*/2$).

As the tissue is allowed to swell freely, appropriate boundary conditions are that the mixture stress and electrochemical potentials of water and ions are continuous across the boundary (Frijns *et al.*, 1997),

$$0 = [\mu^w]^+_-, \tag{2.32}$$

$$0 = [\mu^+]^+_-, \tag{2.33}$$

$$0 = [\mu^-]^+_-, \tag{2.34}$$

$$0 = [\mathbf{n} \cdot (\boldsymbol{\sigma}_e - p\mathbf{I}) \cdot \mathbf{n}]^+_-, \tag{2.35}$$

where $[\ ]^+_-$ denotes the change in value of a variable across the boundary, and $\mathbf{n}$ is an

outwards unit normal to the tissue boundary.

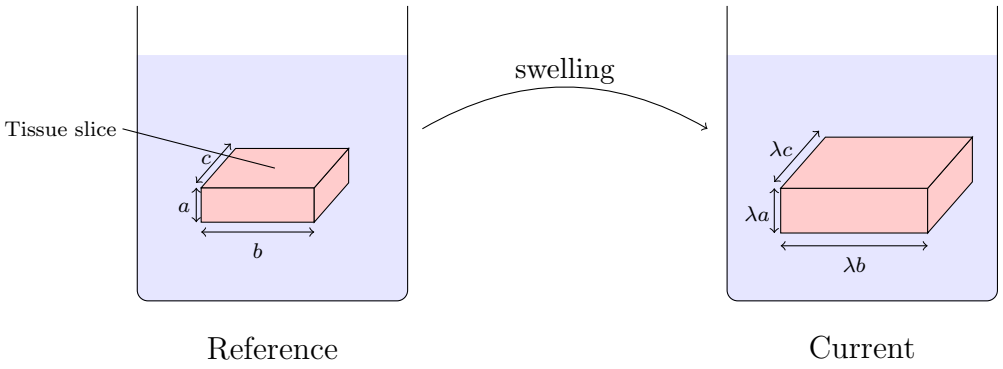

Figure 2.2: Schematic of the reference and current configurations relevant to modelling of tissue slice experiments. For a homogeneous and isotropic mixture under free swelling boundary conditions, the strain field will be isotropic under quasi-static loading. Thus a cuboid with sides of original length (a, b, c) will deform into a cuboid with sides of length $(\lambda a, \lambda b, \lambda c)$ where λ is the stretch. Both locally and globally, the relative volume change is $\lambda^3 - 1$.

2.3.2 Equilibrium solutions for free swelling of a triphasic cube

For an isotropic and homogeneous slab of tissue under the free swelling boundary conditions (equation (2.35)), the strain field will be isotropic under quasi-static loading, and the gradient deformation tensor of the form $\mathbf{F} = \lambda \mathbf{I}$ with λ the stretch. Thus the volume of a reference unit element in the current configuration is $J = \det \mathbf{F} = \lambda^3$, see Figure 2.2. This volume change is relative to an unstressed reference state; for this example the unstressed reference state is where the tissue is submerged in a 'hypertonic' bath so that $c^* \gg c^f$. In this reference state the ion concentrations are the same in the bath and the tissue and there is no pressure gradient between the tissue and bath.

For the slab to be in equilibrium, the electrochemical potential of the fluid and ion phases must be constant across the tissue (otherwise gradients of the electrochemical potentials would drive movement of the fluid and ion phases according to equation (2.18)). Hence,

$$\mu^i = \text{constant} \qquad \text{for} \qquad i = +, -, w. \tag{2.36}$$

The concentration of ions within the tissue may be found by rearranging the expressions for the electrochemical potentials for the ion species (2.21) to eliminate the electric potential, and applying the electroneutrality (2.19) and boundary conditions (2.32)-(2.33).

We find that,

$$c^{\pm} = \frac{1}{2}\left(\pm c^f + \sqrt{c^{f\,2} + c^{*2}}\right). \tag{2.37}$$

where we recall that c^f is the FCD and c^* is the concentration of ion species in the external solution.

Equation (2.37) is the well known equation of a Donnan equilibrium (Cowin and Doty, 2009; Lai *et al.*, 1991). Note that if the solid phase were uncharged (so that $c^f = 0$), then at equilibrium the ion concentration in the tissue would equal that of the solution bath. However when an FCD is present, there is an ionic concentration difference between the tissue and the bath. This arises as both ionic species must satisfy electroneutrality, and must be in electrochemical equilibrium.

As the chemical potential of water is constant across the tissue, equation (2.21) for the chemical potential of solute and boundary condition (2.32) allow the pressure difference between the tissue and solution bath to be found:

$$p - p^* = RT\left(c^+ + c^- - c^*\right), \tag{2.38}$$

This shows that, in equilibrium, a hydrodynamic pressure difference exists between the tissue and bath that is exactly balanced by the osmotic pressure difference.

For a homogeous, isotropic deformation the mixture stress balance (2.18) may be integrated, and boundary condition (2.35) applied, to show that the pressure difference between the tissue and solution is balanced by the elastic stress in the tissue,

$$p - p^* = \sigma_e. \tag{2.39}$$

Here, we have used the fact that the deformation is isotropic to write $\boldsymbol{\sigma}_e = \sigma_e \mathbf{I}$. We emphasise that equation (2.18) can be integrated to obtain (2.39) for this specific geometry (homogeneous, isotropic deformations in a Cartesian geometry), but this does not hold more generally. In Chapters 4 and 5 we consider inhomogeneous swelling of a sphere, for which equation (2.39) does not hold.

Together, equations (2.38) and (2.39) show that the elastic stress in the mixture balances the osmotic pressure difference, and may be combined along with mass conservation for the FCD (2.14) to obtain an algebraic expression for the stretch of the elastic medium

λ:

$$RT\left[\sqrt{\left(\frac{\phi^{w}{}_{(0)}c_0^f}{\lambda^3-1-\phi^{w}{}_{(0)}}\right)^2+c^{*2}}-c^*\right]=\sigma_e(\lambda) \tag{2.40}$$

To make further progress, the effective Cauchy mixture stress $\sigma_e(\lambda)$ must be specified (by choosing a constitutive law), and equation (2.40) solved for the amount of swelling, *i.e.* the stretch λ. In the following section we consider some of the constitutive laws that have been chosen to model brain tissue, and investigate how these different choices affect the appropriate solutions of equation (2.40).

2.3.3 Comparison of strain energy functions

Equation (2.40) shows that tissue deformation is determined by a balance between the osmotic pressure and elastic stress. Here we compare several constitutive laws which have been used in previous models of brain tissue in the literature. The strain energy functions and corresponding general forms of the effective stress tensor (obtained using equation 2.17) are detailed in Appendix A.

Table 2.2: Effective stress corresponding to deformations of the form $\mathbf{F}=\lambda\mathbf{I}$ for several constitutive laws. Two neo-Hookean models are investigated: the first includes a logarithmic volumetric term, and the second an algebraic volumetric term.

Constitutive law	Effective stress $\sigma_e(\lambda)$, ($\boldsymbol{\sigma}_e{=}\sigma_e(\lambda)\mathbf{I}$)
Infinitesimal	$3\kappa_s(\lambda-1)$
Neo-Hookean	$\frac{1}{J}\left[\mu_s(\lambda^2-1)+\lambda_s\ln\lambda^3\right]J$ logarithmic volumetric term $\frac{1}{J}\left(\mu_s(\lambda^2-1)\right)+\lambda_s(J-1))$ algebraic volumetric term
Ogden	$\frac{1}{J}\sum_{n=1}^{N}\left(\frac{2\mu_n}{\alpha_n}(\lambda^{\alpha_n}-1)+\mu'(J-1)J\right)$
Fung	$3\kappa_s\frac{(\lambda^2-1)}{2\lambda}\exp\left[\frac{9\kappa_s}{4c}(\lambda^2-1)^2\right]$

We first consider the infinitesimal strain tensor, which is valid for only small defor-

mations, but which has been used extensively to represent the elastic behaviour of brain tissue (see Chen and Sarntinoranont, 2007; Nagashima *et al.*, 1990; Smillie *et al.*, 2005; Taylor and Miller, 2004, for example). Additionally we investigate constitutive laws valid for finite deformation: the Ogden, neo-Hookean and Fung elastic models. An Ogden type hyperelastic model was applied to brain tissue by García and Smith (2009) to model infusion tests, whilst the Fung model was used by Elkin *et al.* (2010) to model the equilibrium behaviour of brain tissue slices in solution baths of differing concentrations. Table 2.2 shows the form of the effective stress $\sigma_e(\lambda)$ corresponding to a homogeneous isotropic deformation for each of these constitutive laws.

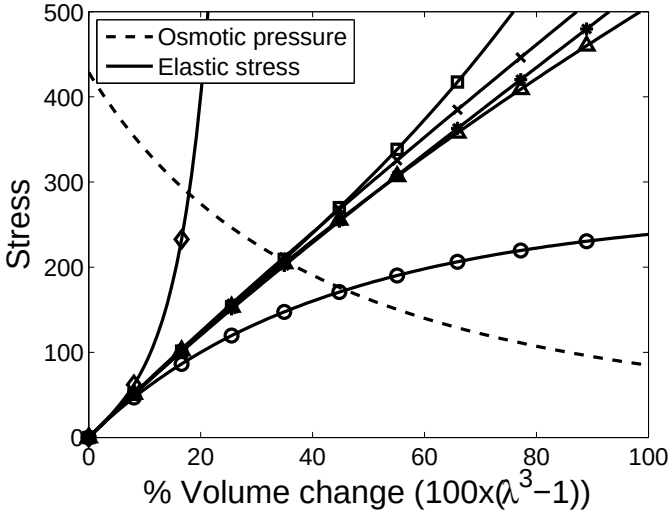

Figure 2.3: Dashed curve shows osmotic pressure (left side of equation (2.40)) with $c_0^f = 5$ mEq/l, $c^* = 300$ mOsm. Solid curves show elastic stress for the strain energy functions from Table 2.2. The equilibrium swelling is given by the intersection of the dashed curve and the solid curves. $\diamond$: Fung model with $c = 16.5$ Pa, $\square$: Fung model with $c = 1000$ Pa, $\times$: neo-Hookean with algebraic volumetric term, $*$: 1-family Ogden model with $a_1 = -4.7$ and μ', μ_1 calculated from equation A.10, $\triangle$: infinitesimal stress tensor, $\circ$: neo-Hookean with logarithmic volumetric term. For all models $R = 8.3$ J mol^{-1} K^{-1}, $T = 310$ K, the Young's modulus $E = 584$Pa and Poisson ratio $\nu = 0.35$, with corresponding Lamé parameters $\lambda_s = 500$ Pa, $\mu_s = 200$ Pa.

Figure 2.3 illustrates the effective Cauchy stress for each of the functions from Table 2.2, as a function of the stretch λ. The Lamé parameters are fixed, and other parameters based upon values used by others for each particular model. The Fung model is shown for two different values of the strain-stiffening parameter: c=1000 Pa which is a typical value for biological tissues (Holzapfel *et al.*, 2000), and c=16.5 Pa which is the value used Elkin *et al.* (2010) to model swelling of brain tissue[2]. We see that up to volume changes

[2]We believe this value is unphysiological, and present an alternative explanation for their observations in Chapter 3.

of 100%, the Ogden, algebraic neo-Hookean and Fung (with physiological parameter $c = 1000$) models display similar behaviour. However, choosing a different volumetric term for the neo-Hookean model or changing the parameter c controlling the effect of the exponential term in the Fung model causes very different behaviours. The wide variations in the behaviour of these functions highlights the importance of choosing a strain energy function with reasonable parameter values.

As shown by equation (2.40), tissue deformation is determined by a balance between the osmotic pressure and elastic stress. The dashed line in Figure 2.3 shows the osmotic pressure in the tissue as a function of the deformation. We see that osmotic pressure is a decreasing function of the stretch. This is due to the fact that the FCD decreases as the tissue expands, and therefore the difference in ion concentration between the tissue and bath decreases. For a particular constitutive law the volume change is determined by the intersection between the osmotic pressure and elastic stress; for example Figure 2.3 shows that the chosen 1-family Ogden material would exhibit a volume increase of about 35% (the intersection of the dashed curve, and solid curve with starred markers, in Figure 2.3).

2.3.4 Role of bathing solution concentration

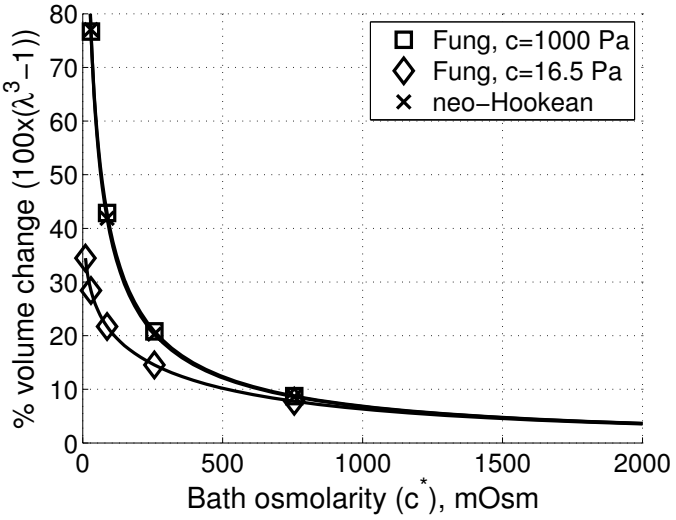

Figure 2.4: Predicted volume change for tissue slices in osmotic solution bath, as a function of the bath osmolarity c^* (solutions to equation (2.40)). Two different strain energy functions are chosen for comparison. The neo-Hookean model and Fung with $c = 1000$ Pa predict very similar results, which would be expected as the stress-strain dependence is similar over the region of interest (see Figure 2.3). Parameters: $\lambda_s = 500$ Pa, $\mu_s = 200$ Pa, $c_0^f = 5$ mEq/l.

As well as the constitutive relation for the strain energy function, the volume change

in swelling may depend on the elastic moduli and the concentration bathing solution. The elastic parameters are reasonably well constrained, so in Figure 2.4 we show the expected volume change for Fung and neo-Hookean materials as a function of the ionic concentration of the bathing solution c^*. These strain energy functions were chosen for comparison, because with a physiological strain stiffening parameter c the Fung and neo-Hookean models display similar stress-strain behaviour up to $\approx 50\%$ volume change, whilst the Fung model with a lower strain stiffening c parameter exhibits different behaviour (see Figure 2.3). Results were obtained by solving equation (2.40) numerically for λ (using an inbuilt Matlab solver), across the range of values for c^*.

We observe that the tissue swells more in a less concentrated solution. This counter intuitive result is a consequence of the Donnan equation (2.37). As in Figure 2.3, the choice of strain energy function affects the results once the predicted volume changes exceed approximately 10%.

2.4 Compressibility: Deformation-dependent permeability

An important component of the mechanics of edema is the compression of brain tissue. To investigate this, we consider a simple example: a piston compressing a cube of mixture, in the absence of solute species and FCD. The triphasic model described in §2.2 then reduces to a biphasic model for a porous elastic solid and interpenetrating fluid in the absence of any solute species ($c^i = 0$) and where the solid phase is uncharged ($c^f = 0$); this biphasic model was originally formulated by Mow *et al.* (1980) for infinitesimal deformations, and has been applied to finite deformations of articular cartilage (Cowin and Doty, 2009; Holmes and Mow, 1990) and other tissues including the brain (García and Smith, 2010).

This example allows us to explore the compressibility of a biphasic system, and investigate the relationship between deformation and key parameters such as the hydraulic permeability and elastic moduli. We consider a geometry that allows only uniaxial strain, simplifying the governing equations significantly. This set-up is similar to the experiments performed to investigate consolidation of brain tissue by Franceschini *et al.* (2006), although they considered only infinitesimal deformations.

2.4.1 Governing equations and geometry

The governing equations for the biphasic mixture consist of the mass and momentum balance for the mixture, (2.11) and (2.18) respectively, mass conservation for the solid phase (2.12), relation between the solid displacement and velocity (2.7), and the expression for

the fluid flux (2.26). In the absence of solutes, the fluid flux equation (2.26) reduces to Darcy's law for flow through a porous medium,

$$\mathbf{q}^w := \phi^w(\mathbf{v}^w - \mathbf{v}^s) = -K\nabla p. \tag{2.41}$$

We model a cube of biphasic mixture enclosed in a container, as illustrated in Figure 2.5. A piston acts on the uppermost surface of the tissue, and applies a time dependent force $F(t)$ per unit surface area to the tissue surface. The upper surface allows free drainage of fluid, whilst the side and base walls of the container are impermeable to fluid. Therefore the displacement of the tissue is independent of the x and y coordinates, and the system reduces to a uniaxial strain problem in the z direction.

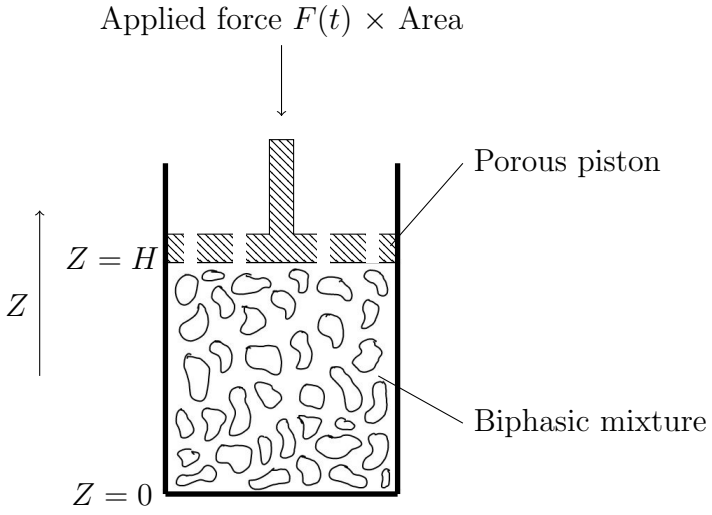

Figure 2.5: Illustration of the set-up considered for the uniaxial biphasic model described in §2.4.1. A biphasic material in an impermeable container is compressed by a porous piston. This results in uniaxial deformation in the Z direction.

We use finite deformation elasticity, and work in the reference (or Lagrangian) configuration. We define $u = \boldsymbol{u} \cdot \hat{\mathbf{e}}_z$, v^s and q^w as the displacement, solid velocity and fluid flux respectively in the Z direction, and assume that the tissue originally has a height H. As the deformation occurs only in the Z direction, the deformation gradient tensor $\mathbf{F}$ and dilation $J = \det \mathbf{F}$ are of the form,

$$\mathbf{F} = \begin{pmatrix} 1 & 0 & 0 \\ 0 & 1 & 0 \\ 0 & 0 & 1 + \dfrac{\partial u}{\partial Z} \end{pmatrix}, \qquad J = 1 + \frac{\partial u}{\partial Z}. \tag{2.42}$$

For the boundary conditions, on the lowermost surface of the mixture there is no

tissue displacement and no flux of fluid, *i.e.*

$$u|_{Z=0} = 0, \qquad q^w|_{Z=0} = 0, \tag{2.43a,b}$$

On the uppermost surface of the tissue ($Z = H$), a time dependent applied stress $F(t)$ is imposed by the piston and, because fluid may drain freely, the pore pressure equals the pressure outside the mixture, which we set to 0 as a reference pressure. We therefore have,

$$\sigma|_{Z=H} = F(t), \qquad p|_{Z=H} = 0, \tag{2.44a,b}$$

We prescribe that initially the mixture is undeformed and in equilibrium,

$$u|_{t=0} = 0, \qquad p|_{t=0} = 0. \tag{2.45a,b}$$

To solve this system (comprising equations (2.7), (2.11), (2.18) and (2.41) along with boundary and initial conditions (2.43)-(2.45)), we first manipulate the governing equations to obtain a single partial differential equation for the displacement u, which we then solve numerically. For uniaxial strain the stress balance for the mixture (2.18) reduces to,

$$\frac{\partial}{\partial z}(\sigma_e - p) = 0 \tag{2.46}$$

where $\sigma_e = \{\boldsymbol{\sigma}_e\}_{zz}$. Integration of the one-dimensional mass conservation equation (2.11), in the absence of a source term, gives,

$$v^s = -\, q^w, \tag{2.47}$$

where the no flux boundary condition on the lowermost surface (2.43b) has been applied. Physically, equation (2.47) means that the mixture can only compress if a corresponding amount of fluid leaves via the porous lid (since each component is incompressible).

We now use the relationship between solid phase strain and velocity (2.7), Darcy's law (2.41) and the integrated one-dimensional mass conservation equation (2.47) to obtain a governing equation for u:

$$\left.\frac{\partial u}{\partial t}\right|_Z = v^s = K\frac{1}{J}\frac{\partial \sigma_e}{\partial Z}, \tag{2.48}$$

where σ_e is a function of $\partial u/\partial Z$ (depending upon the constitutive law chosen), and $J = 1 + \partial u/\partial Z$ is the mixture dilation. Thus the system is reduced to a single partial differential equation for $u(Z,t)$, along with boundary conditions (2.43a) and (2.44a), and

initial condition (2.45a). To progress any further, a constitutive law must be specified for the effective mixture stress, σ_e. In this section we choose the solid as a neo-Hookean material, such that

$$\sigma_e = \mu_s \left(J - \frac{1}{J} \right) + \lambda_s \left(J - 1 \right), \tag{2.49}$$

where μ_s, λ_s are the Lamé coefficients. The above expression is obtained from the general Cauchy stress for a neo-Hookean material (A.6).

We solve equation (2.48) numerically, using the Method of Lines. The first step is to discretise equation (2.48) in space, using a central second order finite difference scheme. This results in a set of time dependent ordinary differential equations in time (one at each gridpoint). As each endpoint, we have algebraic constraints (2.43a) and (2.44a). The resulting system can then be solved using the MATLAB `ode15s` ODE solver.

2.4.2 Uniaxial compression with constant hydraulic permeability

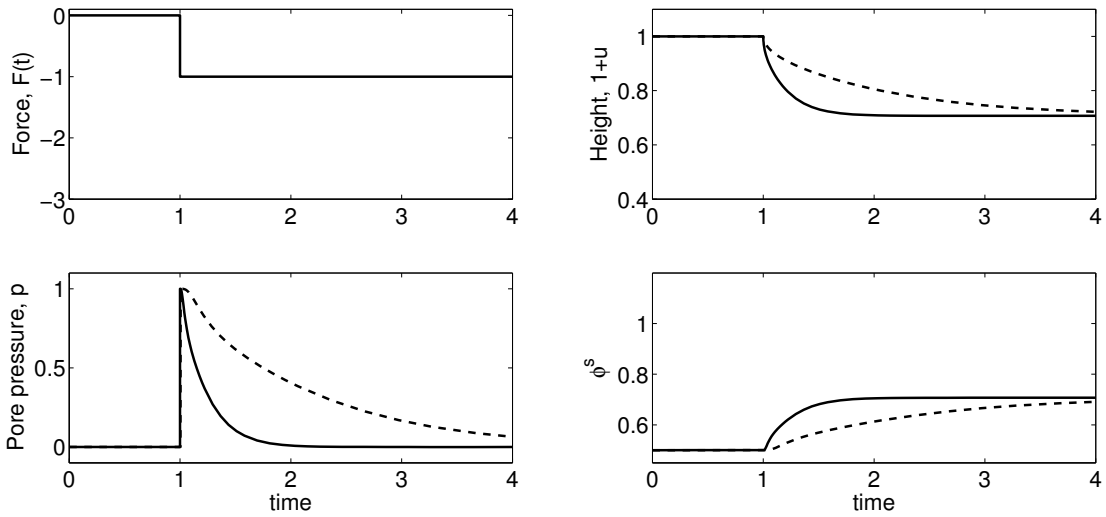

Figure 2.6: Simulations for the one-dimensional compression of a biphasic material, subjected to a constant force applied instantaneously at $t = 1$. Plots shows the imposed applied force, height of the tissue, and pore pressure and solid volume fraction at the centre of the tissue $Z = 0.5$, as a function of time. Solid curves correspond to a more permeable mixture ($K = 0.5$) and the dashed curves to a less permeable mixture ($K = 0.05$). Elastic parameters: $\lambda_s = \mu_s = 1$.

Solutions to equation (2.48) along with boundary conditions (2.43) and (2.44) for an instantaneous applied force are shown in Figure 2.6. Results show the height of the

tissue, along with the pore pressure and solid volume fraction at the centre of the tissue. The mixture undergoes consolidation, whereby the tissue gradually compresses to its final state after the force is applied. The pressure in the tissue instantaneously increases when the force is applied, and gradually returns to its original value as the water moves out. This occurs because it takes time for water to flow through the mixture; we observe that a greater hydraulic permeability K allows the mixture to reach equilibrium more quickly. From equation (2.48) we observe that time, t, scales with K (so that letting $\hat{t} = Kt$ removes K from the problem), and therefore we would expect the system to respond more slowly to a lower value of K.

Figure 2.7 shows a continuously increasing applied force. Whilst the pressure within the tissue does increase when the force is applied, the peak pressure attained is lower than when the tissue was subjected to an instantaneous applied force (Figure 2.6). This is because the pressure peak is required to move fluid more quickly: when the force is applied more slowly, the fluid can leave more slowly, and a lower pressure is required to drive it. However the bottom right subplot in Figure 2.7 highlights a problem with the physical relevance of this simulation: as the force increases, the volume fraction of solid ϕ^s becomes greater than 1.

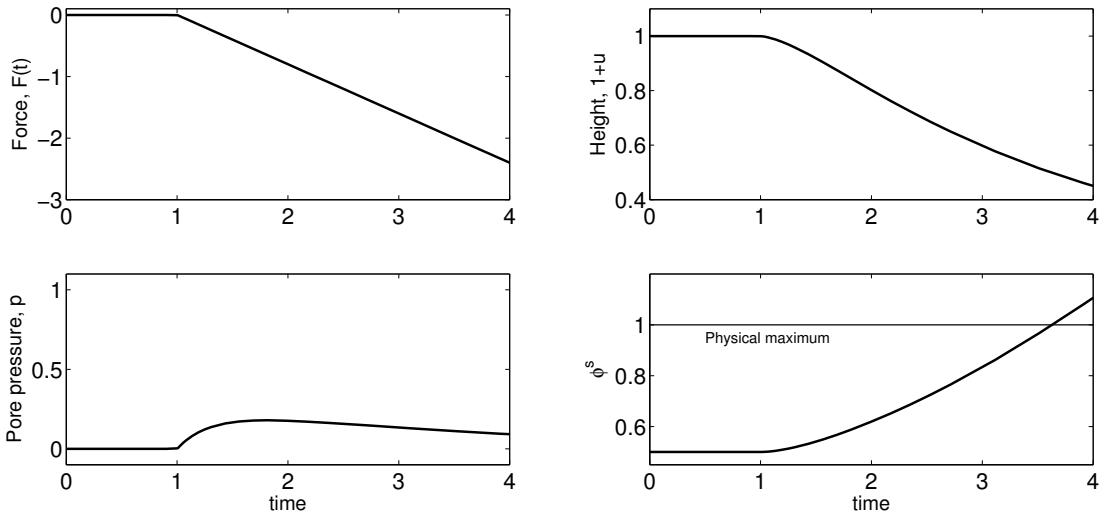

Figure 2.7: Simulations for the one-dimensional compression of a biphasic material, subjected to an gradually increasing applied force. Plots shows the imposed applied force, height of the tissue, and pore pressure and solid volume fraction at the centre of the tissue $Z = 0.5$, as a function of time. Parameters: $K = 0.5$, $\lambda_s = \mu_s = 1$. From the lowermost plot, we observe that the solid volume fraction ϕ^s exceeds the physical limit $\phi^s < 1$: see text for a discussion of this.

Volume fractions are defined as the proportion of the mixture volume comprised of each phase, and therefore by definition must be constrained between 0 and 1 if the model

is to be physically relevant:

$$0 \leq \phi^s \leq 1 \tag{2.50}$$

Using the mass conservation constraint for the solid phase (equation (2.12)), this is equivalent to a constraint on the deformation,

$$J \geq \phi_0^s. \tag{2.51}$$

In fact, when $\phi^w = 0$ and $\phi^s = 1$ there is no water present: the mixture is entirely composed of incompressible solid and and is impermeable to fluid flow. This relationship between K and ϕ_s is missing from the current formulation. However, it is observed (*e.g.* Holmes and Mow, 1990; Markert, 2007) that constraint (2.50) is satisfied if the hydraulic permeability of the mixture is made a function of the volume fraction(s), such that

$$K(\phi^w) \to 0 \text{ as } \phi^w \to 0. \tag{2.52}$$

In §2.4.3 we explore solutions to equation (2.48) where the hydraulic permeability is a function of the volume fractions in such a way that (2.52) is satisfied.

Trivially, we note that if we had assumed zero water flux rather than free drainage on the surface of the piston, regardless of the magnitude of force applied by the piston the mixture would experience no deformation. This is because the fluid and solid phases are both intrinsically incompressible; when water cannot escape the mixture is unable to compress.

2.4.3 Constitutive laws for hydraulic permeability

In the previous section, we observed that assuming K=constant gives unphysical behaviour, and suggested that this behaviour would be removed if $K(\phi^w) \to 0$ as $\phi^w \to 0$. To our knowledge, no experimental studies have explicitly investigated the deformation-dependent permeability of brain tissue. However, it has been discussed in the experimental literature that the permeability of brain tissue would be expected to increase in the core of the swollen region (Fenstermacher and Patlak, 1976), and decrease in the surrounding tissue (Katayama and Kawamata, 2003).

For small deformations of brain tissue, several authors (Chen and Sarntinoranont, 2007; Sobey and Wirth, 2006) used the constitutive form for hydraulic permeability pro-

posed by Mow *et al.* (1980) for articular cartilage under infinitesimal deformations,

$$K = K_0 \exp\left[M(J-1)\right]. \tag{2.53}$$

where K_0 and M are constant parameters, and J is the dilation of the tissue. Similar constitutive laws have been proposed by Holmes (1985). However these constitutive laws are proposed only for infinitesimal deformations, and do not satisfy the constraint (2.52): they should not be used for large deformations where ϕ^s approaches 1.

Constitutive laws for the permeability of soft tissue undergoing large deformations have only been partially investigated experimentally. An example of a suitable dependence was tested by Gu *et al.* (2003), who found that the hydraulic conductivity of agarose gels varied with fluid volume fraction. They proposed an empirical relation of the form,

$$K = \frac{1}{\mu}\alpha\left(\frac{1-\phi^s}{\phi^s}\right)^n \tag{2.54}$$

(where α has units m^2 and μ is the fluid viscosity). For agarose gel and cartilage, a value of $n = 3.2$ showed good agreement with experimental data.

A constitutive law of the form (2.54) was also shown to exhibit better agreement with experimental results for foam compression than an exponential law (2.53) (Markert, 2007). An alternative to (2.54) is the Carman-Kozeny equation (Coussy, 2004), which relates the mixture permeability to the underlying matrix structure. Attempts have been made to apply this approach to biological tissues, although the complex microstructure (the solid matrix can be thought of as a mixture of cells, collagen and other proteins such as GAGs) makes it difficult to identify which components of the tissue are relevant to water movement (Levick, 1987).

Figure 2.8 shows the same simulation as Figure 2.7, but where the hydraulic permeability is of the form (2.54) for $n = 1$ and $n = 3.2$. In each case the volume fractions remain bounded in the range 0 to 1, and the pore pressure in the material increases to balance the applied stress as the solid volume fraction approaches 1. Where $n = 3.2$ the mixture compresses at a slower rate than where $n = 1$, and the pore pressure builds up more rapidly: this is because a decrease in the solid volume fraction causes a greater decrease in the permeability of the mixture for larger n, making it more difficult for the fluid to leave the mixture.

In this section, we have considered the compression of a biphasic cube undergoing uniaxial strain. This example highlights the compressible nature of the biphasic mixture: even though each of the solid and fluid phases is inherently incompressible, the mixture itself compresses as fluid leaves. This causes the volume fraction of solid to increase.

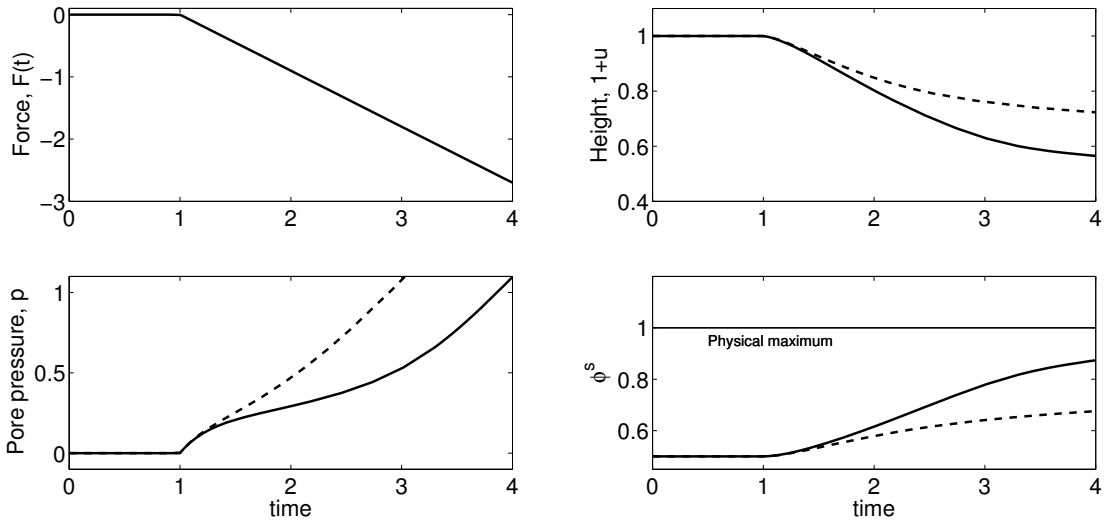

Figure 2.8: Simulations for the one-dimensional compression of a biphasic material, compressed with a permeable piston at $X = 1$. The set-up is as described in Figure 2.7, with the exception that $K = K_0(\phi^w/\phi^s)^n$ with $n = 1$ (solid curves) and $n = 3.2$ (dashed curves) so that $K \to 0$ as $\phi^w \to 0$. The bottom-left plot shows that the volume fractions are within the range 0 to 1 (contrast with Figure 2.7).

Care must be taken to ensure that a suitable constitutive law is chosen for the hydraulic permeability K, so that the permeability decreases as fluid leaves.

Along with an appropriate choice for the permeability K, we must also consider a suitable strain energy function $W(\mathbf{F})$ for the mixture. When there is no fluid present in the mixture (*i.e.* $\phi_s = 1$) then the mixture is comprised only of incompressible solid; therefore the strain energy function must be chosen to ensure that the mixture becomes incompressible when $\phi^s = 1$. The strain energy functions considered in §2.3.2 do not satisfy this requirement, and therefore cannot capture the behaviour of the mixture when no fluid is present.

2.5 Solute Transport and Osmotic Pressure

The formation and resolution of brain edema is closely related to changes in ion and protein concentrations, which drive water movement (Simard *et al.*, 2007). In §2.3, we showed that the interaction of a FCD and charged solutes can result in tissue swelling via the Donnan effect. In this section, the last of our three case studies, we aim to understand whether osmotic effects besides the Donnan effect can drive water movement and swelling within the triphasic modelling framework.

We investigate transport of a single uncharged solute species within an uncharged

deformable porous media, as this is the least complicated version of the triphasic model that retains solute movement. As we are considering just a single solute, we drop the i superscript from quantities related to the solute. Of particular interest is the ratio of mixture to pure diffusion coefficient D/D_0 introduced by Ateshian *et al.* (2006), and we define $\sigma = 1 - D/D_0$ in analogy to the reflection coefficient for transport through a membrane[3]. For the case of a single neutral solute this parameter appears in the expressions for fluid flux (2.26), which may be simplified:

$$\mathbf{q}^w := -K\left[\nabla p - RT\sigma\nabla c\right] \tag{2.56}$$

and the governing equation for solute transport (2.29),

$$\frac{\partial}{\partial t}(\phi^w c) = \nabla.\left[\phi^w D\nabla c - \phi^w c\sigma\mathbf{v}^s - \phi^w c(1-\sigma)\mathbf{v}^w\right]. \tag{2.57}$$

We recall that D and D_0 are defined relative to the solute-to-solid and solute-to-solvent drag (2.24). If the solute-to-solid drag is negligible then $D = D_0$; $\sigma = 0$ and the solid matrix offers no resistance to solute movement. If the solute-to-solid drag is infinite, then $D = 0$; $\sigma = 1$ and drag between the solute and solid is so large that the solute is unable to move through the solid matrix. That is, the solute moves with the velocity of the solid phase, and is effectively 'trapped' by the solid matrix. Hence the ratio D/D_0 is a measure of the extent to which solute movement is hindered by the solid matrix and $\sigma = 1 - D/D_0$ is a measure of the permeability of the mixture to the solute.

We seek to understand the equilibrium behaviour of a mixture, with an initially inhomogeneous spatial distribution of solute, for two cases. Firstly, we neglect solute-solid drag ($D = D_0$ and $\sigma = 0$), following many authors who model small ionic solutes (for example, Lai *et al.*, 1991; Sun *et al.*, 1999). Secondly, we consider the limit in which the solute is unable to permeate through the tissue, so that $D = 0$ and $\sigma = 1$. In Chapter 3, we present a model to explain the swelling of tissue slices which incorporates solute species with each of these properties.

[3]Starling's law of filtration states that the rate of fluid flow across a semipermeable membrane (such as a microvessel wall) is proportional to the hydrostatic pressure difference minus the osmotic pressure difference,

$$J_v = L_p(\Delta p - \sigma\Delta\pi) \tag{2.55}$$

where J_v is the rate of fluid flow, L_p the hydraulic conductivity of the vessel wall, Δp the hydrostatic pressure difference across the vessel wall, $\Delta\pi$ the osmotic pressure difference across the vessel wall, and σ the osmotic reflection coefficient. The osmotic reflection coefficient $\sigma = 1$ if the vessel wall is impermeable to the solute, and $\sigma = 0$ if the vessel wall offers no resistance to solute movement ((Truskey *et al.*, 2010), p. 474).

In Chapter 4 we incorporate Starling's law into a biphasic model of brain tissue, to represent fluid entering the brain from capillaries. Starling's law is discussed further in §4.2.2.

2.5.1 Model problem: solute and water transport in a one-dimensional slice

For simplicity, we consider a one-dimensional mixture immersed in a solution bath. We assume that the bathing solution pressure is $p^* = 0$ and solute concentration $c^* = 0$ relative to some reference pressure and concentration, and that the mixture is initially in a stress free reference state (see Figure 2.9). At $t = 0$ we impose an spatially inhomogeneous solute distribution, and investigate the equilibrium solute distribution and whether the presence of solutes drives deformation of the mixture.

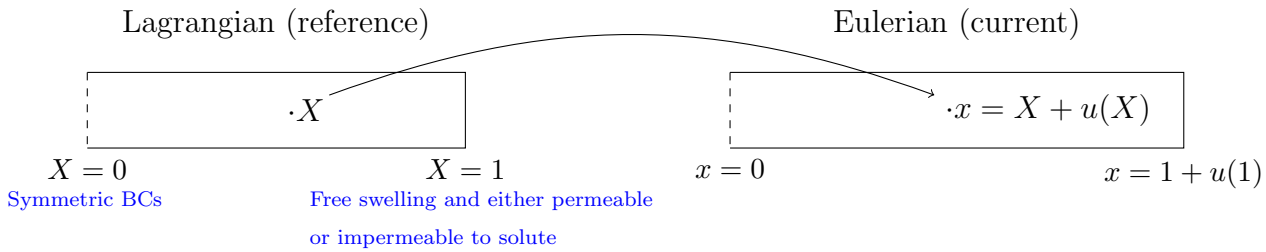

Figure 2.9: Illustration of the set-up considered for the one-dimensional reduction of a triphasic model, with a single uncharged solute, as described in §2.5.1.

The governing equations presented in §2.2 may be reduced when only a single neutral solute is considered. We can consider a system of three variables: the solute concentration c, displacement $\mathbf{u}$, and pore pressure p. The three governing equations comprise the mixture stress balance (2.15), the mass conservation equation for the solute (2.57), and the mass conservation for the mixture (2.11). This latter equation may be written,

$$\left.\frac{\partial \mathbf{u}}{\partial t}\right|_{\mathbf{X}} = K\left[\nabla p - \sigma RT \nabla c\right] \tag{2.58}$$

by substituting the solute flux (2.56) and solid displacement (2.7) into the mixture mass conservation equation (2.11). Additional variables that appear in these equations (fluid volume fraction and velocities) may be expressed in terms of the pore pressure p, solute concentration c and displacement $\mathbf{u}$ using the solid mass conservation (2.12), the saturation condition (2.8) and relation between solid and fluid velocity (2.7). Additionally, a constitutive law must be chosen for the effective stress tensor.

For a one-dimensional system we define $u = \mathbf{u} \cdot \hat{\mathbf{e}}_x$ as the displacement in the x direction so that the dilation is $J = 1 + \partial u / \partial X$. As the outer boundary (initially at $X = 1$) is free to move, in order to solve the system on a fixed domain we will rewrite the governing equations into the Lagrangian (reference) configuration. Thus we write the initial and boundary conditions in terms of Lagrangian coordinates.

Initially we assume that there is an inhomogeneous distribution of solute, prescribed by a function $c_0(X)$, that the mixture is not deformed, and that the pressure is constant everywhere. Thus the initial conditions are,

$$c|_{t=0} = c_0(X), \qquad u|_{t=0} = 0, \qquad p|_{t=0} = 0. \tag{2.59a,b,c}$$

For the boundary conditions, we impose symmetry at $X = 0$,

$$u|_{X=0} = 0, \qquad \left.\frac{\partial c}{\partial X}\right|_{X=0} = 0, \qquad \left.\frac{\partial p}{\partial X}\right|_{X=0} = 0 \tag{2.60a,b,c}$$

and consider two different types of boundary condition on the outer surface $X = 1$. In both cases, we assume that the tissue can swell freely and the outer boundary is freely permeable to water. Therefore the chemical potential of the solute (2.21) and normal component of stress (2.16) are continuous across the boundary at $X = 1$,

$$\sigma_e|_{x=1} - p|_{X=1} = 0, \qquad p|_{X=1} - RT\, c|_{X=1} = 0, \tag{2.61a,b}$$

where $\sigma_e = \hat{\mathbf{e}}_x \cdot \boldsymbol{\sigma}_e \cdot \hat{\mathbf{e}}_x$. For the solute, we assume that either the outer boundary is freely permeable to solute, or that the outer boundary is entirely impermeable to solute,

$$c|_{X=1} = 0, \qquad \text{or} \qquad 0 = v^c|_{X=1} - v^s|_{X=1} \tag{2.62a,b}$$

where v^c is the solute velocity, which may be related to the fluid flux and solute concentration using equation (2.28). We choose these two boundary conditions so that we can contrast the consequences of solute being trapped locally within the material ($\sigma = 1$) with the consequences of solute being unable to leave at the boundary (2.62b).

We consider the equilibrium steady state behaviour of the system in §2.5.2. We will investigate whether the initial distribution of solute, $c_0(X)$, affects the final equilibrium state, and the effect of the parameter σ and outer boundary permeability.

2.5.2 Steady-state behaviour

For a one-dimensional problem in steady state, integrating the time-independent fluid flux equation (2.58) shows that osmotic pressure in the tissue is everywhere equal to the pore pressure plus a constant. Integrating the stress balance (2.15) and applying the stress balance boundary condition (2.61a) gives that the pore pressure is everywhere equal to the elastic stress, *i.e.*, $\sigma_e = p$. We therefore have that, in steady state, the

osmotic pressure balances with the elastic stress at each point,

$$\sigma_e = p = \sigma RTc + \text{constant}. \tag{2.63}$$

The behaviour of the tissue therefore depends on the value of the parameter $\sigma = 1 - D/D_0$. When $\sigma = 0$ the solute is able to permeate through the tissue, whilst when $\sigma = 1$ the solute is unable to permeate through the tissue. We consider each of these limiting cases in turn.

Permeating solute ($\sigma = 0$)

Where the solute is able to permeate through the mixture ($\sigma = 0$), at steady state the solute transport equation (2.57) reduces to,

$$0 = \nabla . \left(\phi^w D \nabla c\right). \tag{2.64}$$

In one spatial dimension, this can be integrated and the symmetry boundary condition at the centre (2.60b) applied; this shows that the solute concentration c is constant. Furthermore, the integrated stress balance (2.63) gives that the pore pressure p and the effective stress σ_e are also constant. The constant value that c takes depends on the choice of boundary condition for solute movement at the outer edge (2.62a,b).

If the solute is able to move freely across the tissue boundary, *i.e.* (2.62a) holds, then to be in equilibrium the solute must have equilibrated with the solution bath (*i.e.* $c = 0$). The remaining boundary conditions on the outer edge (2.61a,b) give that in this case the pore pressure and effective stress will also be 0. Hence,

$$c = 0, \qquad p = 0, \qquad u = 0, \tag{2.65}$$

at steady state.

If no solute flux is allowed through the mixture boundary, *i.e.* (2.62b) holds, then at equilibrium the mixture must contain the same total amount of solute as it did initially. Thus,

$$\int_0^1 c_0 \phi_0^w \, \mathrm{d}X = \int_0^{1+u(1)} c\phi^w \, \mathrm{d}x = \int_0^1 \frac{1}{J} c\phi^w \, \mathrm{d}X = \frac{1}{J} c\phi^w \tag{2.66}$$

where the first equality reflects the global conservation of solute, the second is a mapping from Eulerian ($x = X + u$) to Lagrangian (X) co-ordinates, and the third follows since, in equilibrium, the concentration and deformation gradient are uniform. In the case of no-

flux boundary conditions, the steady-state solute concentration may thus be calculated as the spatially averaged initial solute concentration,

$$c = \frac{J}{\phi_w} \int_0^1 c_0(X)\phi_0^w \, \mathrm{d}X. \tag{2.67}$$

Applying the outer boundary conditions (2.61a,b) yields,

$$\sigma_e = RT\frac{J}{\phi_w} \int_0^1 c_0(X)\phi_0^w \, \mathrm{d}X, \tag{2.68}$$

which is an algebraic equation for the dilation J. Equation (2.68) can be solved for J and hence u, following which c and p may be obtained from equations (2.67) and (2.63) respectively.

Non-permeating solute ($\sigma = 1$)

When a solute cannot permeate through the mixture, $\sigma = 1$; the diffusion coefficient of the solute in the mixture is $D = 0$. The governing equation for solute movement (2.57) then reduces to,

$$\frac{\partial}{\partial t}(\phi^w c) + \nabla \cdot (\phi^w c \mathbf{v}^s) = 0. \tag{2.69}$$

Comparing the above equation with the original mass conservation equation for a solute species (2.10), we observe that these two equations are equivalent, except that the solute velocity appears within the second term of equation (2.10) while it is the solid velocity that appears in the second term of equation (2.69): the solute and solid velocities are equal when $\sigma = 1$. This is to be expected since $\sigma = 1$ means that the solute can only move if the solid does. Equation (2.69) is equivalent to,

$$\phi^w c = \frac{\phi_0^w c_0}{J} \tag{2.70}$$

where ϕ_0^w is the reference-state fluid volume fraction and c_0 the reference state solute concentration, showing that the solute may move only due to deformation of the solid matrix.

We have already shown that at steady state, the elastic stress is balanced by the steady-state osmotic pressure (2.63). Thus the deformation-dependent solute concentration (2.70) may be substituted into the stress balance (2.63) to yield an algebraic equation

for the dilation $J = 1 + \partial u/\partial X$,

$$\sigma_e = RT\left(\frac{\phi_0^w c_0(X)}{J\phi_w}\right) \tag{2.71}$$

where σ_e is a prescribed function of J (via a constitutive law). The steady-state fluid volume fraction is given as a function of J by,

$$\phi_w = \frac{J - \phi_0^s}{J}. \tag{2.72}$$

As in §2.4, we shall use a neo-Hookean strain energy function here (see 2.49).

We observe the similarities between the expression for the equilibrium swelling of a mixture containing non-permeating neutral solutes (2.71), and the equilibrium swelling of a mixture with ion concentrations induced by a FCD and the Donnan effect (2.37), which was discussed in §2.3. We see that in both cases there is an osmotic pressure difference between the mixture and surroundings; this is caused by solutes that are unable to travel through the mixture. In the case of non-permeating solutes, the solutes are unable to move due to mechanical restriction, whilst in the case of charged ions and the Donnan effect the solutes are held in place by their electrostatic attraction to the FCD. This osmotic pressure difference balances with the elastic stress in the mixture at equilibrium, leading to swelling.

Examples of steady-state solutions

Figure 2.10 shows steady state solutions for two different initial solute concentration profiles $c_0(x)$, under both free-solute-movement (2.62a) and no-solute-flux (2.62b) boundary conditions. The initial profiles of solute, $c_0(x)$, are chosen such that in both cases the total amount of solute within the mixture is the same. These results show the stretch profile, $J - 1$, as a function of X; all other variables can be determined from this.

Figure 2.10(b) shows that when solute can permeate through the tissue ($\sigma = 0$) and move across the tissue boundary, then in equilibrium there is no concentration difference between the tissue and external solution as the solute equilibrates with the solution bath. Therefore the tissue remains undeformed. When $\sigma = 0$, Figure 2.10(c) shows that if solute cannot move across the tissue boundary, the equilibrium stretch is constant but non-zero throughout the tissue and does not depend on the initial concentration profile. This is because the steady state solution depends only upon the total amount of solute, rather than the initial solute distribution (see equation (2.67)). However the tissue does expand, because of the osmotic pressure difference between the mixture and solution bath.

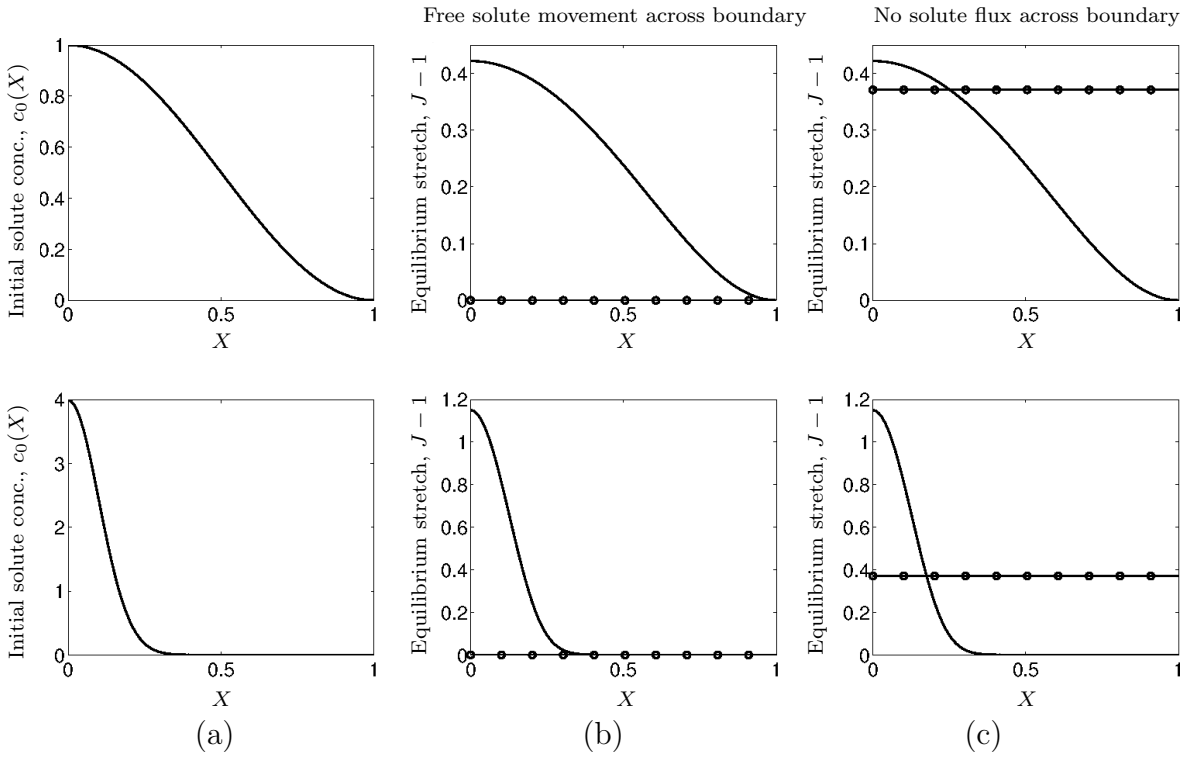

Figure 2.10: Steady-state solutions for the stretch $(J-1)$ of a triphasic mixture, containing a single uncharged solute, for two different initial solute distributions. (a) initial solute distribution $c_0(X)$, (b) equilibrium tissue stretch for free-solute-movement boundary conditions, (c) equilibrium tissue stretch for no-solute-flux boundary conditions. The top row shows solutions for a cosine initial distribution, whilst the bottom row shows solutions for a Gaussian initial distribution. The total amount of solute is the same for each distribution. Curves without symbols correspond to $\sigma = 1$ (non-permeating solute), whilst symbols '•' correspond to $\sigma = 0$ (permeating solute). Parameters: $\lambda_s = \mu_s = 1000$Pa, $\phi_0^w = 0.2$.

When $\sigma = 1$, Figure 2.10 shows that the tissue deformation is identical for both free solute movement and no solute flux boundary conditions. This is because the solute cannot move through the tissue and therefore behaviour of solute at the boundary will not affect solute behaviour in the tissue. Hence the deformation is determined solely by the initial concentration distribution.

These steady state solutions illustrate that neutral solutes can only lead to osmotic pressures when the solutes are unable to move freely, either due to a semipermeable membrane at the boundary, or due to their inability to move through the solid matrix. Both of these mechanisms may be relevant in the brain. The blood brain barrier (BBB) surrounding the capillaries can be thought of as a semipermeable membrane; under healthy conditions the BBB is impermeable to solutes and little water can pass through, whilst, when damaged, the BBB becomes more permeable to both solutes and water (Rapoport,

1978). Prolonged periods of increased osmolarity have been observed in regions of damaged and swollen tissue (Kawamata *et al.*, 2007), which may contribute to retention of water. We will explore these concepts further in Chapters 3, 4 and 5.

2.6 Discussion

In this Chapter, we have presented a triphasic model for a mixture of porous elastic solid, fluid and solute phases. The model can be simplified by neglecting some of these phases, allowing us to highlight the features of the model relevant to the behaviour of brain tissue.

Any mathematical model able to capture swelling of brain tissue must be capable of exhibiting certain effects: in particular water accumulation, hydrostatic and osmotic pressure driven deformation, deformation-dependent permeability, and the ability to incorporate the elastic properties of brain tissue that have been observed experimentally. We have shown that the model is indeed able to capture these effects and have given three case studies that illustrate the important concepts. The remainder of this thesis is concerned with incorporating these effects in more realistic, biological relevant, scenarios.

Chapter 3

Swelling of brain tissue slices

3.1 Introduction

Brain swelling, or edema, occurs when there is an abnormal accumulation of water within the brain tissue (Fishman, 1975; Marmarou, 2007). It is thought that this water accumulation is primarily driven by osmotic effects (Klatzo, 1987), as the mechanisms that maintain osmotic gradients between tissue, blood and cerebrospinal fluid are disrupted when tissue is damaged (see §1.2.2).

Ultimately we would like to understand the relation between osmotic gradients, water accumulation and deformation in damaged brain tissue. As an initial step towards understanding the interplay of these complex processes leading to edema, we consider here the swelling of brain tissue slices bathed in a salt solution. This scenario is simpler than the *in vivo* brain for two main reasons. Firstly there is no blood flow through the slices, so physiological effects caused by changes in blood brain barrier permeability may be ignored. Secondly, the source of edema fluid is the salt solution bath whose composition and pressure can be controlled.

3.1.1 Experimental swelling of brain tissue slices

Tissue slice experiments are common as brain slices *in vitro* maintain many aspects of their *in vivo* characteristics, whilst the external environment can be controlled with relative ease (Cho *et al.*, 2007). Numerous experimental studies have observed that when brain tissue slices are excised from the brain and placed in an isotonic solution bath they swell (Elkin *et al.*, 2010; Hrabětová *et al.*, 2002; Pappius and Elliott, 1956). We focus on understanding the experimental results of Elkin *et al.* (2010), who carried out systematic experiments to determine slice volume change over a range of bathing solution concentrations.

This chapter in based upon Lang *et al.* (2014)

Elkin *et al.* (2010) performed experiments on rat cortex slices, of size 3×1.5×0.35mm. Two sets of experimental conditions were used that are of particular interest. First, slices were treated with electron transport chain decouplers (10mM 2-deoxyglucose and 5mM sodium cyanide) and placed in an isotonic (300mOsm) artificial CSF solution (Gey's salt solution) for 24 hours. This treatment blocked metabolic activity in the cells, leading to damage and hence swelling. The volume of the slices was measured to establish a baseline volume change in isotonic conditions; this value was found to be 74±10%.

Second, damaged slices were transferred to solutions with different ionic concentrations (6, 200, 300, 1000, 2000 and 4000mOsm) for two hours. The volume of the tissue was then measured again. It was observed that when the tissue was moved to a less concentrated ionic solution bath it would swell further but when the tissue was moved to a more concentration solution bath then it would shrink. Elkin *et al.* (2010) presented results for the volume change relative to the baseline volume. However we are interested in the processes leading to the total volume change from healthy to damaged tissue and so we combine the results for the concentration dependent swelling with the mean baseline volume change to obtain the total volume change in each ionic concentration, relative to the original volume of the healthy tissue slice.

3.1.2 Causes of brain slice swelling

As discussed in §1.2.2, *in vivo* brain tissue swelling may be caused by one or more of a number of mechanisms, including changes in blood brain barrier permeability, accumulation of plasma proteins in the tissue and abnormal cell metabolism and function. However as brain tissue slices are isolated from the vasculature, changes in blood brain barrier permeability cannot be a factor in the swelling of such slices.

Elkin *et al.* (2010) propose that the Donnan effect contributes to the physical driving force underlying brain tissue swelling. The Donnan effect occurs when a charged porous medium is in contact with an ionic solution. At equilibrium the ions must be in electrochemical equilibrium, and the tissue must be electroneutral. The charges on the porous medium require neutralisation and so ions move in to neutralise the charge attached to the porous medium; the ion concentration is therefore greater within the porous medium that outside. This difference in internal and external ion concentration leads to an osmotic pressure that drives fluid from the ionic solution into the porous medium (Lai *et al.*, 1991). If the porous medium is elastic, this osmotic pressure and the concomitant influx of water causes deformation of the medium, *i.e.* swelling.

The fixed negative charges in the brain tissue are due to macromolecules such as proteoglycans and DNA: we refer to these charges collectively as the Fixed Charge Density (FCD). In healthy brain tissue, macromolecules with a net negative charge are present

within cells (Leaf, 1959). As living cells are able to actively regulate transport across their cell membrane, they are able to prevent the influx of ions that would otherwise lead to the Donnan effect. The FCD in healthy tissue is therefore isolated from the tissue mixture, and so there is effectively no FCD. However, when brain tissue is damaged the cell membranes lose their integrity and the FCD within cells may become exposed. The tissue can then be thought of as a mixture of solid components (extra and intracellular matrix with FCD attached), water, and dissolved ions. Thus, tissue damage effectively causes an increase in the FCD of the tissue, which might lead to tissue swelling via the Donnan effect.

An alternative hypothesis for the increase in osmotic pressure within the tissue slices is that it is caused by an accumulation of solutes. An increase in tissue osmolarity has been measured in the core of an edemic region following contusion and ischemia, that was not due to changes in organic ion concentration (Kawamata *et al.*, 2007). The authors hypothesise that the increase in osmolarity is due to solutes produced during abnormal metabolism in distressed tissue. An increase in solute concentration could also arise from the proteins which are usually isolated within the intracellular space (Leaf, 1959) and become merged with the interstitum when the cell membranes are damaged.

As the experimental slices of Elkin *et al.* (2010) measure just 0.35mm in thickness, small uncharged solutes that are able to diffuse easily through the mixture will rapidly equilibrate in concentration with the solution bath. Only solutes that cannot move through the convoluted architecture of the tissue, and become 'trapped' by the solid matrix, will contribute to the osmotic pressure within the tissue. These are equivalent to the non-permeating solutes, with a reflection coefficient $\sigma = 1$, discussed in §2.5.1

In this work, we extend the triphasic approach to investigate whether exposure of FCD (the Donnan effect) alone is sufficient to explain the two experimental observations of Elkin: (i) the 74% volume increase observed in isotonic bathing solution, and (ii) the dependence of the final slice volume on the ionic concentration of the bathing solution.

3.2 Mathematical model for equilibrium swelling

We consider a steady state equilibrium model of swelling, rather than investigating the dynamics of the system. To understand why this static assumption is appropriate we consider the time scales in the problem. The experimental slices were of thickness h=0.35mm, the diffusion coefficient of ions in soft tissue is of order D=10^{-10} $\mathrm{m^2 s^{-1}}$ (Sun *et al.*, 1999), and the hydraulic conductivity of brain tissue to water is of order K=10^{-12} $\mathrm{m^2 Pa^{-1} s^{-1}}$ (Cheng and Bilston, 2007; Smillie *et al.*, 2005). The time scale for ions to equilibrate is h^2/D, whilst the time scale for water to equilibrate is $h^2/(K\Delta p)$ (where Δp is the

pressure drop across the system, which is of order Δp=1000 Pa for brain tissue swelling). Calculating these time scales indicates that both the water and ions should respond to an instantaneous change in FCD over a time scale of minutes. In the experiments of Elkin *et al.* (2010) however, swelling evolved over several hours. This suggests that it is biological processes (such as the rate of exposure of FCD) rather than physical processes (such as the rate of movement of ions and water) that determine the swelling rate. At each stage of the process we therefore expect the system to be approximately in equilibrium.

We use a steady state triphasic model (see §2.3) to investigate the volume change in brain tissue caused by a prescribed FCD increase. The mathematical model we present in §3.2.1 is equivalent to that given by Elkin *et al.* (2010). However in §3.4 we show that this model can be extended to account for the presence of additional non-permeating solute species.

A key point is that a triphasic mathematical model measures the volume change of the tissue relative to a 'reference state'. We take the reference state to be the original volume of the tissue when excised, before the experiments began. Therefore the volume change predicted by our model is the total volume change undergone during the experiments (*i.e.* the volume change between healthy tissue when originally excised, and damaged tissue following both experiments). In contrast, Elkin *et al.* (2010) treated the already damaged tissue, in a concentrated solution bath, as being the reference state. Whilst the latter approach allows the behaviour of damaged tissue to be studied, the physical relevance of their reference state is unclear, and the causes of the overall change in tissue volume cannot be investigated.

3.2.1 Model setup

We consider a cuboid of tissue allowed to swell freely in an ionic solution bath. We assume that the solution bath is of constant composition, well mixed, and at concentration c^* and pressure p^*. The tissue is modelled as a triphasic mixture of incompressible phases: an elastic solid phase (representing solid components of the tissue such as the extracellular matrix), a fluid phase, and a solute phase composed of positive and negative ion phases in solution. In addition there is an FCD represented by a negative charge on the solid matrix. Figure 3.1 shows a schematic of the phases considered in our model.

The volume fraction of the solid phase, defined as the volume of solid divided by the volume of the mixture, is denoted by ϕ^s. We assume that the mixture is saturated and the solute concentrations are sufficiently dilute that the volume fractions of solute may be neglected in comparison with the solid and fluid phases: thus the volume fraction of fluid is $1 - \phi^s$. The concentrations of positive and negative ions, and FCD within the tissue, are denoted c^+, c^- and c^f respectively. The mixture is electroneutral, and when in

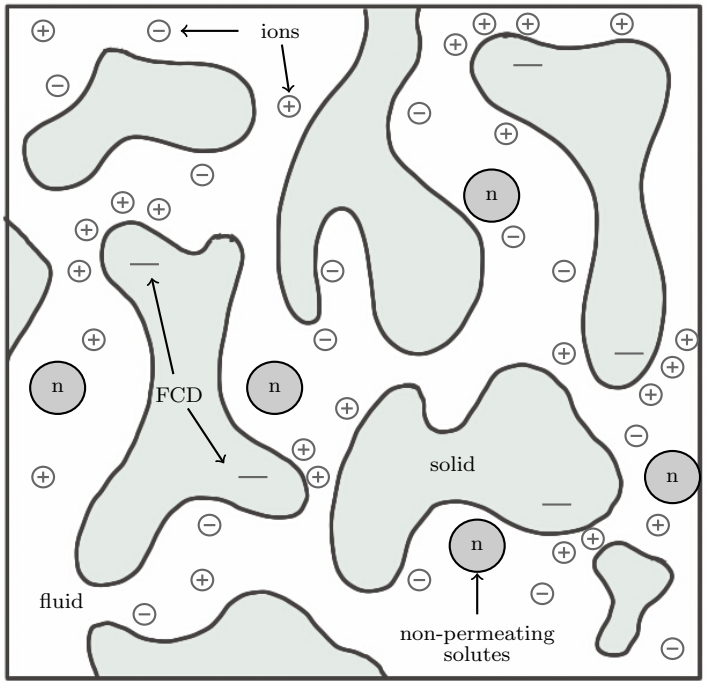

Figure 3.1: A schematic of the phases considered in a triphasic model: a solid phase, fluid phase, and solutes (positive (+) and negative (−) ion species, and non-permeating solutes (n)). Some components of the solid phase have a net negative charge (fixed charge density (FCD)), which induce ion concentrations to satisfy charge neutralisation.

steady state the fluid and ion phases are in electrochemical equilibrium. When an FCD is present these requirements cause the steady state ion concentration to be greater within the tissue than in the solution bath (Lai *et al.*, 1991; Huyghe and Janssen, 1997).

We compute the steady state equilibrium to determine the volume change between healthy and damaged tissue. In the healthy state we assume that the FCD is negligible: therefore the ion concentration within the tissue is equal to that of the solution bath and there is no osmotic pressure within the tissue. We model tissue damage by increasing the reference state c_0^f to mimic an increase of FCD caused by breakdown of the regulatory mechanism. This FCD induces an ion concentration difference between the tissue and bath which causes an osmotic pressure gradient. This osmotic pressure difference drives water to accumulate within the tissue, therefore causing swelling.

3.2.2 Governing equations

In this section, we recap the governing equations for a triphasic cuboid in equilibrium. This is equivalent to the first case study presented in Chapter 2 (§2.3).

The solid phase is treated as a homogeneous, isotropic, incompressible elastic solid, and the tissue deformation is determined by the stretch of the solid phase. The tissue is

described in the (stress free) reference configuration by the material coordinates $\mathbf{X}$, and after deformation is defined by new coordinates $\mathbf{x} = \boldsymbol{\chi}(\mathbf{X}, \mathbf{t})$ (referred to as the current configuration). The deformation gradient tensor $\mathbf{F}$ is defined by,

$$\mathbf{F} = \frac{\partial \boldsymbol{\chi}}{\partial \mathbf{X}}. \tag{3.1}$$

It is also useful to define $J = \det(\mathbf{F})$, the local change in volume due to deformation (Ogden, 1984). Since the solid phase is incompressible, the mass conservation of the solid phase can be written as

$$\phi^s = \frac{\phi_0^s}{J}. \tag{3.2}$$

where ϕ_0^s is the volume fraction of solid in the stress-free reference state.

The behaviour of the tissue is determined by a balance of elastic stress and osmotic pressure. The elastic properties of brain tissue under finite deformation has been modelled by several stress-strain constitutive laws, including the Ogden (García and Smith, 2010) and Fung (Elkin *et al.*, 2010) models. In §2.3, we showed that these different constitutive laws exhibit similar behaviour when physiological parameter values are chosen. To facilitate comparison with the modelling efforts of Elkin *et al.* (2010) we treat the tissue as an isotropic Fung material (Fung, 1984).

In mixture theory the stress tensor has two components, which represent the stress due to the elastic properties of the tissue and that due to the pore pressure (equation (2.16)). Thus the Cauchy stress for a Fung material has the form:

$$\boldsymbol{\sigma} = -p\mathbf{I} + \frac{1}{J} e^{Q} \left[\lambda_s (\mathrm{tr}\mathbf{B} - 3)\mathbf{B} + 2\mu_s(\mathbf{B}^2 - \mathbf{B}) \right], \tag{3.3}$$

where p is the fluid pressure, $\mathbf{B} = \mathbf{F}\mathbf{F}^T$ is the left Cauchy-Green deformation tensor and,

$$Q = \frac{1}{4c} \left[\lambda_s (\mathrm{tr}\mathbf{B} - 3)^2 + 2\mu_s(\mathrm{tr}(\mathbf{B}^2) - 2\mathrm{tr}\mathbf{B} + 3) \right]. \tag{3.4}$$

The parameters λ_s, μ_s are chosen so that for small deformations they coincide with the Lamé coefficients of the solid, and c is an additional elastic modulus (with units of stress) that controls the strain stiffening.

The tissue experiences free swelling boundary conditions. At equilibrium the stress within the tissue must balance the pressure exerted by the solution bath ($\boldsymbol{\sigma} = -p^*\mathbf{I}$) (Frijns *et al.*, 1997). As the tissue is assumed homogeneous and isotropic, an equilibrium deformation with these free swelling boundary conditions takes the form $\mathbf{F} = \lambda\mathbf{I}$ where λ is the stretch in each of the principal directions. This is the same setup as investigated

in §2.3,and in particular Figure 2.2 illustrates the geometry that we consider. Therefore,

$$p - p^* = \frac{3\kappa_s(\lambda^2 - 1)}{2\lambda}\exp\left[\frac{9\kappa_s}{4c}(\lambda^2 - 1)^2\right]. \tag{3.5}$$

where $\kappa_s = \lambda_s + 2/3\mu_s$ is the bulk modulus.

At equilibrium, the chemical potential of the fluid phase (see equation (2.21)) is constant. Thus the osmotic pressure difference between the tissue and solution balances with the hydrostatic pressure difference. Within the tissue the positive ions (c^+) and negative ions (c^-) contribute to the osmotic pressure. Assuming ideal solutions,

$$p - p^* = RT\left[c^+ + c^- - c^*\right], \tag{3.6}$$

where c^* is the osmotic concentration of the bath, R is the ideal gas constant, and T the absolute temperature.

Equation (3.6) is an expression for the pore pressure p, once the ion concentrations c^+, c^- have been determined. At equilibrium the ions must be distributed so that they are in electrochemical equilibrium (*i.e.* the electrochemical potentials (2.20) are constant) and such that the tissue is electroneutral everywhere ($c^+ = c^- + c^f$): the positive and negative ion concentration within the tissue is therefore determined by the Donnan equilibrium (see Cowin and Doty, 2009; Huyghe and Janssen, 1997, for example):

$$c^+ + c^- = \sqrt{{c^f}^2 + {c^*}^2}. \tag{3.7}$$

As the FCD is attached to the solid phase, the concentration of FCD is related to the deformation according to,

$$c^f = \frac{\phi_0^w c_0^f}{\lambda^3 - 1 + \phi_0^w}, \tag{3.8}$$

where c_0^f and $\phi_0^w = 1 - \phi_0^s$ represent the FCD and volume fraction of water in the stress-free reference state respectively. Substituting equations (3.6), (3.7) and (3.8) into equation (3.5) gives a single equation for the stretch λ:

$$RT\left[\sqrt{\left(\frac{\phi_0^w c_0^f}{\lambda^3 - 1 + \phi_0^w}\right)^2 + {c^*}^2} - c^*\right] = \frac{3\kappa_s(\lambda^2 - 1)}{2\lambda}\exp\left[\frac{9\kappa_s}{4c}(\lambda^2 - 1)^2\right] \tag{3.9}$$

which can be solved numerically for λ (*e.g.* using Newton's method). The right hand side of equation (3.9) represents the elastic stress in the tissue, while the left hand side

the osmotic pressure; the equilibrium state occurs when the elastic stress and osmotic pressure are balanced.

3.2.3 Parameterisation

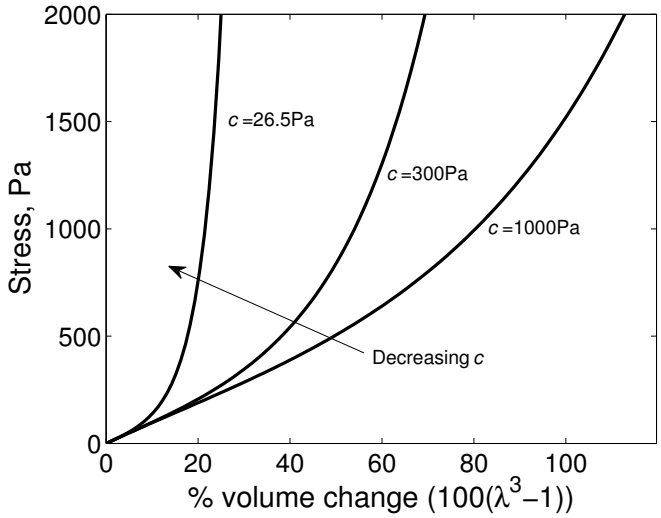

Figure 3.2: Stress-strain relationships for the Fung elastic model, as given by equation (3.5), with bulk modulus $\kappa_s = 380$Pa, for three values of the strain stiffening parameter c. The gradient of each curve gives a measure of the stiffness: a steeper slope indicates that the mixture is stiffer, as a greater stress is required to produce a particular volume change. We observe that all these curves exhibit strain stiffening, whereby the material becomes stiffer at greater strains. The ratio κ_s/c determines the extent of strain stiffening, and at lower values of c the effects of stiffening are noticeable at small volume changes.

The meanings and typical physiological values of the parameters used in the model are given in Table 3.1. Note in particular that for the strain stiffening parameter, c, Elkin *et al.* (2010) fitted their experimental data to obtain $c = 26.5$Pa for brain tissue (they noted that their fit was not sensitive to this parameter). However, if this were the case then the observed volume increase of 74% would require fluid pressure to be of the order 1×10^7Pa (1×10^5mmHg). Since intracranial pressure increases associated with edema are of the order 1×10^3Pa (10−20mmHg) (Reulen *et al.*, 1977), such a large pressure is clearly unphysiological. For a typical biological tissue the exponential coefficient $9\kappa_s/4c \approx 1$ (Holzapfel *et al.*, 2000), and Rashid *et al.* (2012) found this exponential coefficient in the range of $1.68-2.19$ when fitting a hyperelastic Fung model to the uniaxial rapid extension of porcine brain tissue. Therefore we choose $c = 1000$ Pa to ensure that $9\kappa_s/4c \approx 1$. The difference in stress-strain relationships for these values of the strain stiffening parameter c is shown in Figure 3.2.

Elkin *et al.* (2010) used the elastic parameters of Cheng and Bilston (2007), who identified the Young's modulus and Poisson ratio of white matter as $E = 350$ Pa and $\nu = 0.35$ respectively. These values were obtained by fitting experimental data for tissue compression to a viscoporoelastic model for brain tissue. Alternative values for the elastic moduli of brain tissue undergoing slow deformation were proposed by Taylor and Miller (2004), by taking the long-time limit of time-dependent viscoelastic moduli, which had been found by fitting a viscoelastic model to experimental results of compression tests (Miller, 1999). This method yielded $E = 584$Pa and $\nu = 0.35$, and these values have since been used in models of hydrocephalus (*e.g.* Smillie *et al.*, 2005; Sobey and Wirth, 2006; García and Smith, 2010). Since the approaches of Cheng and Bilston (2007) and Taylor and Miller (2004) result in parameters of the same order of magnitude, we use $E = 350$Pa and $\nu = 0.35$ to retain consistency with the approach of Elkin *et al.* (2010)[1].

In the healthy state we assume that the FCD is negligible ($c_0^f \approx 0$). In this case $\lambda = 1$ is a solution of equation (3.9), *i.e.* there is no swelling without FCD. We model damage by increasing the FCD to a fixed value: the FCD in damaged brain tissue was measured by Elkin *et al.* (2010) by assaying the GAG content (glycosaminoglycan, a major component of FCD in biological tissue) of damaged brain tissue; they found a reference state FCD of c_0^f=4mEq/l. For a particular c_0^f the solution λ to equation (3.9) gives the stretch of the tissue from the healthy to damaged state; the corresponding volume change is simply $J - 1 = \lambda^3 - 1$.

Table 3.1: Summary of the parameters values used in the model. Note that the units Eq represent the concentration of a substance multiplied by its valence.

Parameters for the triphasic model in the brain			
Item	Meaning	Value	
κ_s	Bulk modulus (calculated from Poisson ratio of $\mu = 0.35$ and Young's modulus of $E = 350$ Pa)	380 Pa	(Cheng and Bilston, 2007)
c	Strain stiffening elastic parameter	1000 Pa	(Holzapfel *et al.*, 2000)
ϕ_0^w	Reference state tissue water volume fraction	0.8	(Hrabětová *et al.*, 2002)
ϕ_0^s	Reference state solid volume fraction$(1 - \phi_0^w)$	0.2	(Hrabětová *et al.*, 2002)
c_0^f	FCD of damaged tissue at reference state	4 mEq l^{-1}*	(Elkin *et al.*, 2010)
R	Gas constant	8.3 J $\mathrm{mol}^{-1}\mathrm{K}^{-1}$	(Atkins, 2006)
T	Temperature	310 K	(Elkin *et al.*, 2010)

* This value was found using an assay for sulphated glycosaminoglycans (a component of the FCD of brain tissue). Elkin *et al.* (2010) note that this value may not represent the entirety of the FCD found in brain tissue, and in §3.3 and §3.4 we fit for this parameter.

[1]The Lamé parameters λ_s and μ_s are related to the Young's modulus E and Poisson ratio ν by standard relations (*e.g.* Howell *et al.*, 2009),

$$\lambda_s = \frac{E\nu}{(1+\nu)(1-2\nu)}, \qquad \mu_s = \frac{E}{2(1+\nu)}. \tag{3.10}$$

The bulk modulus is given by $\kappa_s = \lambda_s + 2/3\mu_s$.

3.2.4 Reliability of experimental data

In Figure 3.3 we show the experimental data, obtained from Elkin *et al.* (2010). We will exclude the data point corresponding to the 6mOsm solution bath (the most dilute bathing solution) in our analysis. This is because it has been observed experimentally that brain tissue fails at strains over 25% (Bilston, 2011), and the only bathing concentration causing a strain over 25% is 6mOsm (a volume increase of 130% is equivalent to over 30% strain in each principal direction). Therefore it is uncertain whether the elastic parameters are relevant in this regime.

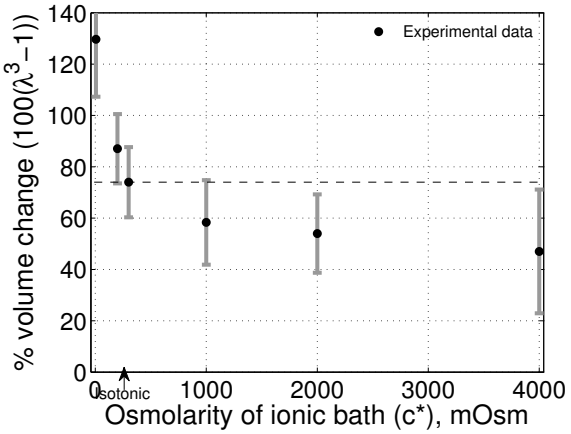

Figure 3.3: Experimental data, obtained from Elkin *et al.* (2010). The horizontal dashed line shows the baseline swelling in an isotonic (300mOsm) solution. The error bars signify the minimum and maximum expected range based upon the standard error of the mean given by Elkin *et al.* (2010).

Furthermore, if the FCD is of comparable magnitude to the concentration of the bathing solution, the osmotic pressure induced by the Donnan effect is very sensitive to the FCD. For example, an increase in the FCD from 10 to 11mEq/l would lead to an osmotic pressure change of only 90Pa (less than 1mmHg) in an isotonic solution. The same FCD increase in a 6mOsm bathing solution (dilute compared with isotonic) could cause an osmotic pressure change of over 2000Pa (15mmHg). For the 6mOsm bathing solution we cannot be confident of the assumption that the concentration of the solution bath remains constant, since products released from the damaged tissue may cause a proportionally large change in the concentration of the bathing solution. For more concentrated bathing solutions this effect would be relatively insignificant. Given the sensitivity of the model to this data point, and the uncertainly over whether the assumptions of the model are valid, we exclude this data point from our analysis.

3.3 The Donnan hypothesis

In this section we analyse solutions to equation (3.9) to investigate whether the Donnan effect is able to explain the magnitude of swelling observed experimentally. The experimental results of Elkin *et al.* (2010) are shown in Figure 3.4b, showing the volume change of tissue slices in ionic solution baths of 6, 200, 300, 1000 and 2000 and 4000mOsm

relative to their size when initially excised.

To begin with, we consider whether the Donnan effect can explain the 74% 'baseline' swelling observed when damaged tissue slices are submerged in an isotonic ionic solution. Figure 3.4a shows both the osmotic pressure (left hand side of equation (3.9)) and elastic stress (right hand side of equation (3.9)) for a tissue slice in isotonic bathing solution (c^*=300mOsm), as a function of the volume change $J-1=\lambda^3-1$. Solutions to equation (3.9) occur where these curves intersect so that the osmotic pressure balances the elastic stress. Table 3.1 shows relevant physiological parameters for brain tissue: based upon the accepted values of these parameters, a volume change of 15% should be expected.

The discrepancy between the 15% swelling predicted and 74% observed experimentally leads us to re-evaluate the material parameters used. The bulk modulus of κ_s=380Pa was measured for recently excised brain tissue (Cheng and Bilston, 2007). It therefore seems possible that the elastic properties of brain tissue may change over the course of the experiment. Figure 3.4a shows that if the bulk modulus of brain tissue were reduced to κ_s=30Pa then 74% swelling would be predicted in an isotonic solution bath. However, whilst there is evidence that unphysiological experimental conditions such as temperature may affect the Young modulus by 50% (Rashid *et al.*, 2013) there is no precedent for the ten-fold decrease in the elastic moduli of damaged brain tissue that would be needed to explain the 74% baseline swelling shown in Figure 3.4a. On the contrary, experiments have indicated that the elastic moduli of brain tissue actually increases post mortem (Metz *et al.*, 1970).

An alternative explanation for the discrepancy is that the FCD of dead brain tissue may be greater than that measured experimentally. The physiological FCD of c_0^f=4mEq/l was calculated by assaying just the sulphated GAGs concentration. As observed by Elkin *et al.* (2010) there may be other sources of FCD in the damaged tissue. If instead the bulk modulus is maintained at κ_s=380Pa but the FCD is increased to c_0^f=15mEq/l, we observe from Figure 3.4a that a volume change of 74% is predicted in an isotonic solution. We now use these two scenarios (κ_s=380 Pa and c_0^f=15 mEq/l, or κ_s=30 Pa and c_0^f=4 mEq/l) as a starting point to investigate the second series of experiments performed by Elkin: examining the additional swelling when the swollen tissue is exposed to different bath concentrations.

Figure 3.4b shows the results of our theoretical model for both of the parameter sets in Figure 3.4a along with the experimental data. This shows that whilst an FCD of c_0^f=15 mEq/l and bulk modulus of κ_s=380 Pa, or FCD of c_0^f=4 mEq/l and bulk modulus of κ_s=30 Pa, are sufficient to explain the swelling observed in isotonic bathing solution (300mOsm), these parameters are not able to explain the swelling observed across the range of ionic bathing solutions investigated experimentally. As a first step

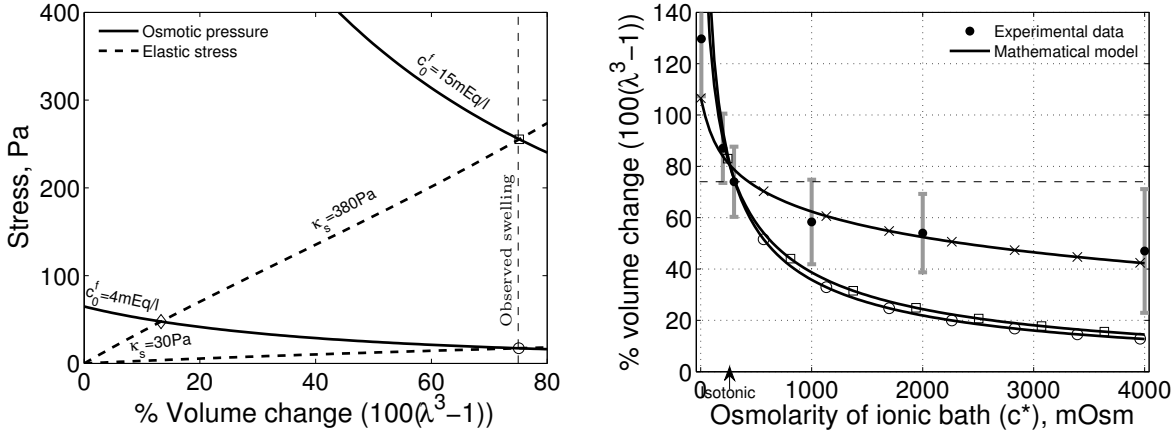

(a) (b)

Figure 3.4: (a) Elastic stress within the tissue (dashed curves) and osmotic pressure due to the Donnan effect (solid curves) in an isotonic solution ($c^* = 300$mOsm) as a function of the tissue volume change. The solution of equation (3.9) is given by the intersection of the elastic stress and osmotic pressure. For an FCD of c_0^f=4mEq/l and bulk modulus κ_s=380 Pa we see that only 15% volume change would be expected, yet experimentally 74% was observed. Increasing the FCD to c_0^f=15 mEq/l or decreasing the bulk modulus to κ_s=30 Pa allows 74% swelling. (b) Shows expected swelling (solutions to equation (3.9)) as a function of bath ionic concentration, for comparison with experimental data from Elkin *et al.* (2010). Each of the two parameter sets that give 74% swelling in isotonic solution (□: c_0^f=15 mEq/l, κ_s=380 Pa. ○: c_0^f=4 mEq/l, κ_s=30 Pa) are used. Additionally we show the curve obtained by performing a least squares fit for the bulk modulus and FCD. ×: c_0^f=157mEq/l, κ_s=4475 Pa. These parameters are unphysiological.

to understanding the swelling observed at different concentrations, we conducted a least squares fit to determine the bulk modulus and reference state FCD that best fit the experimental data. This fit procedure yields κ_s=4475Pa and c_0^f = 157mEq/l. Whilst these parameters show a good fit to the data they are unphysiological: the bulk modulus is an order of magnitude greater than that measured experimentally, while the FCD is two orders of magnitude greater than that measured in brain tissue.

Our theoretical model shows that the Donnan effect is unable to explain the concentration dependent swelling observed experimentally using physiological parameters. This indicates that the exposure of intracellular FCD, leading to the Donnan effect, cannot be the only mechanism driving tissue slice swelling. We therefore seek an alternative explanation.

3.4 Extension to non-permeating solutes

As our modelling in §3.3 shows that it is unlikely that exposure of intracellular FCD is the only driver of increased osmotic pressure, we consider other sources of solutes. For example, the breakdown of capillary membranes can lead to an increase in the plasma protein content of the tissue (Simard *et al.*, 2007). Similarly, breakdown of cell membranes may allow proteins previously isolated within the intracellular space to be released into the tissue. It has been hypothesised that brain injury causes abnormal cellular metabolism leading to degradation of large molecules and tissue structures, causing an elevation in tissue osmolarity (Kawamata *et al.*, 2007). In this section, we investigate the effects of an increase in solute concentration within the tissue.

We hypothesise that along with an increase in FCD, damaged brain tissue also experiences an increase in the concentration of neutral (uncharged) solutes. Whereas many of these solutes may be small enough to diffuse down concentration gradients and equilibrate with the external solution bath, others may be sufficiently large that they become trapped within the tissue by the various membranes and intracellular and extracellular structures that are present. We refer to these as non-permeating solutes (following Ateshian *et al.*, 2006).

Whilst changes in non-permeating solute concentrations and exposure of FCD both lead to osmotic pressure increases, the mechanism through which they do so is different. On the one hand, exposure of FCD induces an ion concentration difference between the bathing solution and the tissue. This is both to ensure electroneutrality and prevent chemical potential gradients at equilibrium (Donnan, 1924). Because of this coupling, the osmotic pressure induced by exposure of FCD depends on the concentration of the bathing solution. On the other hand, non-permeating solutes are physically trapped within the tissue and exert an osmotic pressure of their own accord, independent of the bathing concentration. They are unable to equilibrate with the external bathing solution because they cannot diffuse through the mixture.

For simplicity we assume that a negligible concentration of these non-permeating solutes are present in healthy tissue, whilst there is a homogeneous concentration in damaged tissue. Defining c^n as the solute concentration in a deformed damaged tissue, and c_0^n as the concentration for damaged tissue in the reference state, similarly to equation (3.8) we may express the current concentration in terms of the deformation,

$$c^n = \frac{\phi_0^w c_0^n}{\lambda^3 - 1 + \phi_0^w}, \tag{3.11}$$

Since the non-permeating solutes are trapped within the tissue, their presence alters the governing equation by adding an additional term to the osmotic pressure. Therefore the

governing equation (3.9) is modified to become,

$$RT\left[\sqrt{\left(\frac{\phi_0^w c_0^f}{\lambda^3-1-\phi_0^w}\right)^2+c^{*2}}+\left(\frac{\phi_0^w c_0^n}{\lambda^3-1-\phi_0^w}\right)-c^*\right] = \frac{3\kappa_s(\lambda^2-1)}{2\lambda}\exp\left[\frac{9\kappa_s}{4c}(\lambda^2-1)^2\right]. \tag{3.12}$$

Again the stretch λ is given by the solution of (3.12) for different values of the solution

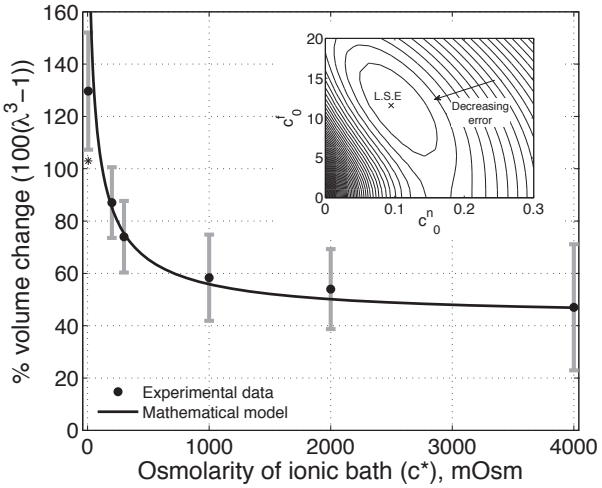

Figure 3.5: Main figure: The solid curve shows solutions to (3.12) for the values of FCD and non-permeating solute concentrations (c_0^f and c_0^n respectively) that minimise the mean squared error (see inset). Black circles show experimental data from Elkin *et al.* (2010), where the error bars signify the minimum and maximum expected range based upon the standard error of the mean. The bulk modulus is κ_s=380Pa for all of these computations. $*$: the data point for the 6mOsm solution bath is excluded from the fitting, see text. Inset: Contours showing the mean squared error of solutions across a range of FCD c_0^f and fixed osmole c_0^n concentrations, compared to the experimental data shown in the main figure. The values that correspond to the least squared error (L.S.E) are c_0^f=11.6mEq/l and c_0^n=0.09mOsm.

bath concentration c^*.

We fit for the reference state FCD c_0^f and non-permeating solute concentration c_0^n from equation (3.12) to the experimental data by minimising the least square error. We find c_0^f=11.6mEq/l and c_0^n=0.09mOsm. Figure 3.5 shows the experimental data and solutions of equation (3.12) for these values. As discussed in §3.2.3, we neglect the data point corresponding to the 6mOsm solution when performing the least squares fit (because it is uncertain whether the model parameters are relevant to such concentrated bathing solutions). However, we include this data point in the plot to show that the mathematical

model and experimental data still agree qualitatively, even with such large deformations.

The inset of Figure 3.5 shows the contours of the least squares error of solutions to equation (3.12) (compared to the experimental data) as a function of the reference state FCD c_0^f and fixed osmole concentration c_0^n. Figure 3.5 shows that the model is able to provide a good fit for the experimental data for bathing solution concentrations in the $100-4000$mOsm range.

3.5 Discussion

We have used a triphasic model to investigate the swelling of brain tissue slices. The triphasic model is appropriate for modelling tissue swelling since it couples the effects of ion concentration and fluid pressure with elastic deformation of the tissue, allowing osmotic effects to drive tissue swelling. We have proposed an extension to the existing model (Lai *et al.*, 1991) by including a further non-permeating solute species, which directly exerts an osmotic pressure on the tissue (Ateshian *et al.*, 2006).

It has previously been proposed that exposure of intracellular FCD (leading to the Donnan effect) provides the physical driving force for swelling of brain tissue slices (Elkin *et al.*, 2010). However, we have shown that, within the bounds of physiological parameter values, the Donnan effect alone is insufficient to explain the magnitude of swelling observed experimentally (volume increases of 74% in isotonic solution). One possible explanation is that the elastic properties of the tissue are altered when the tissue is damaged. However the bulk modulus of the tissue would have to decrease to only 30 Pa (from a usual value of ≈ 400 Pa) for the Donnan effect to explain the magnitude of swelling in isotonic solution. Such a large effect is not supported by the experimental literature where, in fact, the modulus has been reported to increase. Furthermore, this reduction in bulk modulus does not explain the subsequent experimental data across a range of bathing solution concentrations.

We propose that the swelling of brain tissue slices is caused by an increase in osmotic pressure due to the existence of two different types of species: ions trapped in the tissue due to the FCD, and solutes unable to permeate through the tissue due to mechanical obstructions. Tissue swelling caused by non-permeating solutes alone is independent of the ionic concentration of the solution bath. It is the presence of the FCD that causes the ionic concentration of the bathing solution to affect the tissue volume, since the charged FCD interacts with ions to maintain electroneutrality. The presence of FCD explains why the slice volume depends upon the bathing solution concentration, whilst the presence of the non-permeating solutes explains why the tissue is swollen even in baths of very high concentrations (4000mOsm), where the presence of FCD results in minimal swelling. A

least squares fit gives the reference state FCD as c_0^f =11.6 mEq/l and the reference state fixed osmole concentration as c_0^n=0.09mOsm.

A reference state FCD of c_0^f =11.6 mEq/l is greater than the reference state FCD of c_0^f =4 mEq/l measured experimentally by assaying the GAG content of damaged brain tissue (Elkin *et al.*, 2010). However, the authors acknowledged that other macromolecules that were not tested for (such as DNA) may also contribute to the FCD; therefore it seems reasonable to expect the FCD to be greater than that measured in this experiment. In articular cartilage, FCD has been measured in the range 10−30 mEq/l (Lu and Mow, 2008) which is comparable in magnitude to the FCD we hypothesise in damaged brain tissue on the basis of Elkin's data.

Kawamata *et al.* (2007) measured a 91.5mOsm increase in osmolarity due to solutes in the core edemic region of *in vivo* rat brains. Our fit to the experimental data required a non-permeating solute concentration of only c_0^n=0.09mOsm. This large difference may occur because the majority of osmotically active molecules produced within the tissue are small enough to diffuse out of the tissue slice and equilibrate in concentration with the solution bath. Only those trapped within the tissue will contribute to the osmotic pressure difference. Nevertheless the required value of c_0^n is within physiological bounds.

The triphasic model has been validated experimentally for cartilage (Frijns *et al.*, 1997). Soft tissues such as the brain are structurally very different from cartilage, and as the proteoglycan concentration is much lower than cartilage it is not clear whether the tissue contains sufficient negative charges to have a non-negligible FCD. Our work agrees with the hypothesis of Elkin *et al.* (2010), that damaged brain tissue contains sufficient FCD to act as a triphasic material. However we propose that a further term must be considered, to represent the osmotic pressure caused by electrically neutral non-permeating solutes which themselves directly exert an osmotic pressure. These molecules may be released from the intracellular compartment, or produced due to abnormal cellular metabolism, when the tissue is damaged. As cartilage has a low cell density in comparison to other soft tissues, this term is not relevant in the original triphasic model.

Whilst we have shown that the volumetric response of damaged brain slices to changes in ionic bathing solution are consistent with the Donnan effect being present, to our knowledge this effect has not been discussed in the literature with regard to *in vivo* swelling. *In vivo* an exposed FCD would prevent the free movement of ions, which may have consequences for the formation and resolution of edema. Similarly an accumulation of non-permeating solutes could prolong edema if they cannot be cleared from the tissue. When tissue damage occurs in the *in vivo* brain these effects may well be difficult to isolate due to other osmotic effects, and it is only by careful slice experiments that this behaviour can be isolated and further understood.

Chapter 4

Blood brain barrier failure and edema

4.1 Introduction

An increase in the permeability of the blood brain barrier (BBB) is one of the causes of edema (*e.g.* Simard *et al.*, 2007; Kimelberg, 1995). When the permeability of the BBB increases, fluid moves more easily from capillaries into the tissue interstitum, which may lead to water accumulation and swelling. This is known as vasogenic edema. In this Chapter, we investigate the effect of an increase in BBB permeability to water on the swelling of brain tissue. We are particularly interested in understanding how a locally damaged region, with increased BBB permeability, can cause further damage to the surrounding tissue.

This chapter is structured as follows. In this introduction §4.1, we summarise the biological background to the problem. In §4.1.1, we summarise fluid transport in the healthy brain, and discuss the changes that occur following injury. As we are interested in understanding how a locally swollen region affects the surrounding tissue, §4.1.2 concerns the mechanisms by which mechanical changes can cause damage to previously healthy tissue. In §4.2 we present the modelling approach that we use to couple transvascular fluid flux with a biphasic model for soft tissues. We consider the biphasic model in a spherically symmetric geometry, since this is the simplest geometry that allows us to investigate the effect of a local region of increased BBB permeability. In §4.3 we investigate particular aspects of the model, the role of dynamics, finite deformations and boundary conditions, and discuss how the theoretical predictions of this model are applicable to the brain.

4.1.1 Fluid transport in the brain

In the healthy brain, there is a slow bulk circulation of interstitial fluid through the brain tissue. This fluid enters the tissue by filtering from capillaries into the tissue interstitum, crossing the BBB due to hydrostatic and osmotic pressure gradients (Rapoport, 1997). This fluid drains through the tissue into the cerebrospinal fluid (CSF) at the ventricles and subarachnoid space (SAS) (Redzic *et al.*, 2005): see Figure 4.1. In this healthy state the volume of fluid entering brain tissue from the capillaries is low: the average rate of fluid entering the brain tissue from the capillaries has been measured to be in the range 0.15-0.29μl/min per gram of brain tissue in the rat and rabbit, and is believed to be similar for humans (Abbott, 2004).

When brain tissue is damaged, the structure and function of the BBB may be impaired, leading to an increase in the permeability of the BBB to water (Unterberg *et al.*, 2004). This allows water to move more easily into the damaged region of tissue, causing an accumulation of fluid within the tissue (edema). Pressure gradients develop in the tissue (with the pressure decreasing with distance from the damaged regions), and edema can spread as fluid permeates through the brain tissue down these pressure gradients (Reulen *et al.*, 1977). Physiologically, experiments have shown that maximal edema takes at least 6 hours (and indeed up to 3 days) to develop in rats (Hatashita *et al.*, 1988), whilst monitoring of hospital patients indicates than maximal swelling occurs 3-5 days after injury in humans (Marmarou *et al.*, 2000).

When brain tissue is damaged, an increase in BBB permeability is not the only cause of edema (Simard *et al.*, 2007). Alongside increases in BBB permeability, changes in tissue osmolarity are observed (see §1.2.2); it is thought that these changes in the osmotic gradients within the tissue also drive fluid accumulation (Hatashita *et al.*, 1988; Kawamata *et al.*, 2007). Whilst it is evident that osmotic changes occur when brain tissue swells, in this Chapter we neglect osmotic effects in order to focus on the consequences of changes in BBB permeability for brain tissue swelling.

4.1.2 Mechanisms of tissue damage

As discussed in §1.2.3 of Chapter 1, there are two main mechanical mechanisms through which local edema can cause further damage to the surrounding tissue. Firstly, there is axonal stretch. Axons are the protrusions of neurons, which carry chemical and electrophysiological signals through the brain. Axons can be damaged by mechanical deformation, with the severity of the damage caused depending upon both the rate and magnitude of strain inflicted (Smith and Meaney, 2000). It has been shown that rapid deformations are particularly damaging (for example, Tang-Schomer *et al.* (2010) showed

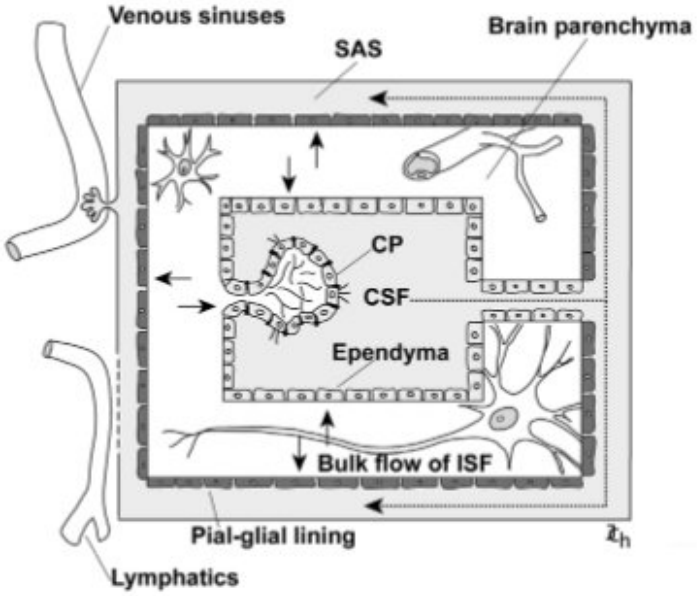

Figure 4.1: Schematic of the bulk fluid flow in the brain. CSF is produced at the choroid plexus (CP) in the ventricles, and flows through the ventricle system out to the SAS where it is reabsorbed into the venous system. There is also a bulk flow of interstitial fluid (ISF) through the brain parencyma, which drains into the CSF at the ventricles and SAS. Source: Redzic *et al.* (2005)

that stretching isolated axons at strain rates of 44s^{-1} to strains of up to 75% caused mechanical failure of the axons). However, as edema evolves over a slow time scale in comparison to rapid inertial deformations, we shall assume that it is the magnitude of strain rather than strain rates that cause damage in our model. If a local region of tissue swells, we would expect other regions of the tissue to be compressed and stretched, due to the constriction of the skull (see Figure 4.2).

The second mechanism of tissue damage is the mechanical stress within the tissue. Increased ICP is detrimental because it can cause compression of the vascular network (Dunn, 2002; Steiner and Andrews, 2006). If the brain suffers from reduced blood flow as a result of this compression then ischemia (lack of oxygen) may occur, ultimately leading to cell damage and death. The actual relationship between cerebral blood flow and intracranial pressure is complicated, because the brain is able to autoregulate its blood flow over a range of ICPs (by dilating or contracting the arteries that bring blood to the brain (Strandgaard *et al.*, 1973)). This autoregulation mechanism is difficult to quantify, and it is unclear whether this process could maintain blood flow locally if just a small region of the brain were damaged. We therefore simply postulate that compression of capillaries may lead to tissue damage.

Whilst the experimental literature typically discusses increased ICP as causing cap-

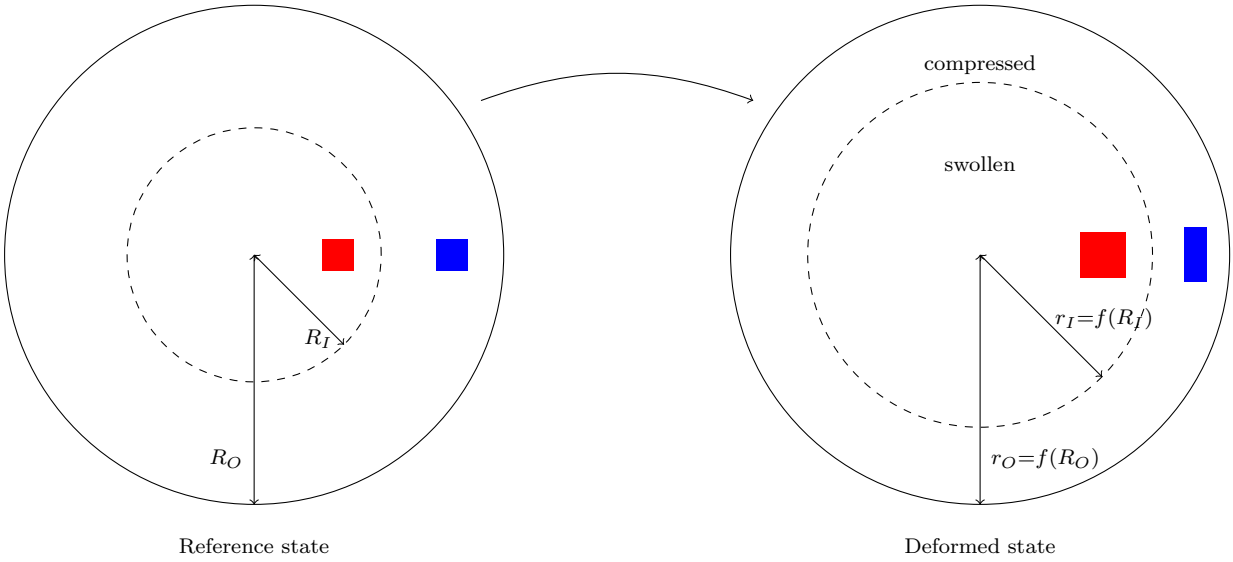

Figure 4.2: Schematic to illustrate how localised swelling within a confined region can result in both stretch and compression of tissue. The coloured regions show how a region which is square in the reference state may become expanded in both the circumferential and radial directions if swollen, but may expand in one direction and compress in the other if squeezed.

illary compression, we must consider what this means within our mixture theory modelling framework. In mixture theory the Cauchy stress is divided into two components, $\boldsymbol{\sigma} = \boldsymbol{\sigma}_e - p\mathbf{I}$, representing the elastic stress and pore pressure respectively. To our knowledge this framework has been used to model edema by only one other author (Nagashima *et al.*, 1990), who used the pore pressure p as a measure of tissue damage. However, we believe that the entire mixture stress acts to compress the capillaries, rather than just the component of the stress attributed to the pore pressure. Hence, we assume that the stress causing damage is related to the total (*i.e.* Cauchy) stress $\boldsymbol{\sigma}$.

In summary, we will consider two simple measures of 'damage' in our work. The first is 'strain damage', which is detrimental to brain tissue because it causes damage to axons (hence preventing the brain from functioning). Strain damage will be tracked by the extension of the mixture. The second is 'stress damage', which represents the extent to which the mixture will exert a compressive force on capillaries (leading to hypoxia and subsequent cell death). Stress damage will be tracked by the compressive stress within the mixture.

4.1.3 Overview of existing models

As we are interested to understand relationships between water accumulation (edema), stress, and strain within the tissue, we use a biphasic mixture approach. Brain tissue is treated as a mixture of solid and fluid phases, and a diffuse source term is incorporated throughout the mixture to represent transvascular fluid flux entering the brain tissue from capillaries. There is precedent for applying this modelling technique to represent brain tissue, and we discuss the most relevant literature here.

To our knowledge, the work of Nagashima *et al.* (1990) is the only attempt to apply this modelling approach to vasogenic edema. A realistic two-dimensional brain geometry was used (based upon a coronal segment of a cat brain), and the BBB permeability increased locally to simulate BBB damage. However, the choice of boundary conditions and parameter values is inconsistent with current literature. For example, the authors impose a no fluid flux boundary condition between the tissue and SAS, contradicting more recent understanding of fluid flow in the brain (Redzic *et al.*, 2005), and use a Young's modulus of $E \sim 10^4$Pa whilst recent experiments suggest that $E \sim 500$Pa is appropriate (Taylor and Miller, 2004).

A similar biphasic approach has been applied to model infusion into brain tissue. However the majority of authors neglect transvascular fluid flux ((for example Chen and Sarntinoranont, 2007; Wirth and Sobey, 2009)), which provides the source of edema fluid in vasogenic edema, and we have discussed these approaches more fully in §1.3.4. Smith and Humphrey (2007) incorporate transvascular fluid flux to investigate the effect of a brain tumour on infusion, because the BBB is more permeable in tumour than healthy tissue. They use a spherically symmetric model, similar to the geometry we choose, although they are primarily interested in understanding profiles of fluid flux within brain tissue (with application to advective drug delivery), rather than deformations and stresses.

All the models mentioned above use an infinitesimal version of the biphasic theory, which is valid only for small strains. However, studies (see for example Simard *et al.* (2007) and Walberer *et al.* (2008)) suggest that brain tissue undergoes relatively large deformations when it swells. We therefore develop a finite deformation framework, before recovering the small deformation limit.

Extensions to the biphasic approach include multiple network poroelastic models, whereby the capillaries are explicitly modelled as a further fluid network in addition to the ISF (Tully and Ventikos, 2011). However, this approach leads to a more complex set of governing equations, and introduces parameters that cannot be quantified from experimental data. In this chapter we do not explicitly consider fluid flow through the vasculature, as we are primarily interested in deformations and pressure changes within

the tissue itself.

4.2 Biphasic model for tissue damage

In this section we discuss the governing equations, geometry, and physiological parameter values appropriate to our model. We follow the biphasic modelling approach of Nagashima *et al.* (1990) and Smith and Humphrey (2007).

4.2.1 Governing equations

Brain tissue is modelled by a saturated biphasic mixture of two inherently incompressible phases: an elastic solid phase 's' and fluid phase 'w'. This is a simplification of the triphasic model presented in Chapter 2, which also considered the presence of solute species.

As the full triphasic model was presented in Chapter 2, here we summarise the governing equations. The tissue is described in the (stress free) reference configuration by the material coordinates $\mathbf{X}$, and after deformation is described by new coordinates $\mathbf{x} = \boldsymbol{\chi}(\mathbf{X}, t)$ (referred to as the current configuration). The tissue displacement $\mathbf{u}$ is given by the change in position,

$$\mathbf{u} = \mathbf{x} - \mathbf{X}, \tag{4.1}$$

and deformation gradient tensor $\mathbf{F}$ is defined as,

$$\mathbf{F} = \frac{\partial \boldsymbol{\chi}}{\partial \mathbf{X}} = \mathbf{I} + \frac{\partial \mathbf{u}}{\partial \mathbf{X}}, \tag{4.2}$$

where $J = \det(\mathbf{F})$ represents the change in volume due to deformation.

We assume the mixture is saturated so that,

$$1 = \phi^s + \phi^w. \tag{4.3}$$

To allow for transvascular water flux from capillaries into tissue, we incorporate a fluid source, denoted Q. The mass of the solid and fluid phases is conserved:

$$0 = \frac{\partial \phi^s}{\partial t} + \nabla \cdot (\mathbf{v}^s \phi^s), \tag{4.4}$$

$$Q = \frac{\partial \phi^w}{\partial t} + \nabla \cdot (\mathbf{v}^w \phi^w), \tag{4.5}$$

where Q (s^{-1}) is the source strength (the local source volume of fluid added per volume

of tissue per unit time). A constitutive form for the fluid source term Q is discussed in §4.2.2.

The movement of the fluid phase is driven by pressure gradients according to Darcy's law,

$$\phi^w(\mathbf{v}^w - \mathbf{v}^s) = -K\nabla p, \tag{4.6}$$

where K ($\mathrm{m^2Pa^{-1}s^{-1}}$) is the Darcy permeability of the mixture to interstitial fluid. Adding the mass conservation equations (4.4, 4.5), using the saturation condition (4.3), and substituting in Darcy's law (4.6), allows the volume fractions ϕ^w, ϕ^s and fluid velocity $\mathbf{v}^w$ to be eliminated. This yields a single equation for mass conservation of the mixture:

$$\nabla \cdot \mathbf{v}^s - \nabla \cdot (K\nabla p) = Q. \tag{4.7}$$

The mixture Cauchy stress $\boldsymbol{\sigma}$ is divided into two components so that $\boldsymbol{\sigma} = \boldsymbol{\sigma}_e - p\mathbf{I}$, where the effective Cauchy stress $\boldsymbol{\sigma}_e$ represents the elastic component of the stress and p is the pore pressure. The effective Cauchy stress is obtained from a strain energy function by $\boldsymbol{\sigma}_e = (1/J)\boldsymbol{F} \cdot \partial W/\partial \boldsymbol{F}$. Neglecting inertia and assuming no body forces, the mixture stress is divergence free,

$$\nabla \cdot (\boldsymbol{\sigma}_e - p\mathbf{I}) = \mathbf{0}. \tag{4.8}$$

Finally the velocity of the solid phase is related to the displacement,

$$\mathbf{v}^s = \left.\frac{\partial \mathbf{u}}{\partial t}\right|_{\mathbf{X}}. \tag{4.9}$$

Along with appropriate boundary and initial conditions, equations (4.7)-(4.9) constitute three equations for three unknowns: $\mathbf{u}$ (solid displacement), $\mathbf{v}^s$ (solid velocity) and p (pore pressure). However the form of the source strength Q requires some discussion, and we turn to this now.

4.2.2 Starling's law for transcapillary fluid exchange

The rate of water movement across the blood brain barrier from capillaries into tissue, Q, is dependent upon the hydrostatic and osmotic pressure differences between the plasma and interstitial fluid. Starling's law is typically used to model flux across a capillary wall

(Rapoport, 1997; Korthuis *et al.*, 2010):

$$Q = L_p \left[\Delta p - \sigma_{ions}\Delta\Pi_{ions} - \sigma_{oncotic}\Delta\Pi_{oncotic}\right], \tag{4.10}$$

where L_p ($\mathrm{Pa}^{-1}\mathrm{s}^{-1}$) is the volumetric flow rate across from the capillary network into the tissue, per unit volume of tissue per unit pressure difference, $\Delta p = p_{\mathrm{cap}} - p$ is the hydrostatic pressure jump across the capillary wall, and $\Delta\Pi_{ions}$, $\Delta\Pi_{oncotic}$ are the osmotic pressure differences due to ions and proteins respectively. The reflection coefficients $\sigma_{oncotic}$ and σ_{ions} represent the permeability of the capillary wall to a solute (a reflection coefficient of 1 means that the wall is totally impermeable to the particular solute, whilst a reflection coefficient of 0 means that the wall is totally permeable).

At this stage we neglect solute movement in the tissue, and assume that the osmotic pressures and reflection coefficients, along with capillary pressure, can be incorporated into a single constant parameter P_e. Then,

$$Q = L_p \left[P_e - p\right], \tag{4.11}$$

where $P_e := p_{cap} - [\sigma_{ions}\Delta p_{ions} + \sigma_{oncotic}\Delta p_{oncotic}]$ (Pa) is the effective driving pressure for fluid flow across the capillary wall, and p is the pore pressure in the tissue.

Substituting the Starling capillary source term (4.11) into the mass conservation equation (4.7) gives a mass conservation equation,

$$\nabla \cdot \mathbf{v}^s - \nabla \cdot (K\nabla p) = L_p(P_e - p). \tag{4.12}$$

The parameters in this equation, the capillary wall permeability L_p, driving pressure P_e and tissue hydraulic permeability K, could be considered as constants, or functions of other variables in the system. For example, spatial dependence could be used to represent material heterogeneities, or the tissue permeability K may be deformation dependent (as discussed in Chapter 2). In this Chapter, we assume that P_e and K are constant throughout the tissue, but allow L_p to be a function of position to simulate local BBB damage.

4.2.3 Geometry and boundary conditions

The system (4.8), (4.9) and (4.12) must be considered together with appropriate initial and boundary conditions. In this section we discuss appropriate boundary conditions.

To represent a local region of tissue we consider a spherically symmetric region of tissue, of radius H, which undergoes spherically symmetric deformations. Then the current ($\mathbf{x} = r\hat{\mathbf{e}}_{\mathbf{r}}$) and reference ($\mathbf{X} = R\hat{\mathbf{e}}_{\mathbf{R}}$) configurations are related by $r = f(R)$ (and

therefore $f(R) = R$ everywhere means that the system exhibits no deformation). Then in spherically symmetric co-ordinates, the deformation gradient tensor and dilation (4.2) are,

$$\mathbf{F} = \nabla_{\mathbf{X}}\mathbf{x} = \begin{pmatrix} f' & 0 & 0 \\ 0 & \dfrac{f}{R} & 0 \\ 0 & 0 & \dfrac{f}{R} \end{pmatrix}, \qquad J = \det(\mathbf{F}) = \frac{f^2 f'}{R^2}, \tag{4.13}$$

where $()'$ denotes differentiation with respect to R. The radial displacement is defined as $u(R) = f(R) - R$. The variables of interest are the pore pressure $p(R)$ and the radial displacement $u(R)$, corresponding to the governing equations (4.8) and (4.12), along with equation (4.9) relating the strain rate to the fluid velocity. The BBB permeability L_p is taken as a function of R, to allow the BBB to be increased locally to mimic regional damage.

As the BBB permeability L_p depend upon R, it makes sense to work in the Lagrangian frame. Therefore we rewrite the governing equations in Lagrangian coordinates, so that the problem can be solved on the reference domain. To rewrite the mass balance (4.12) in Lagrangian coordinates, we use the relations between the Eulerian and Lagrangian description of the gradient of a scalar field and divergence of a vector field,

$$\nabla_{\mathbf{x}}\phi = \mathbf{F}^{-T}\nabla_{\mathbf{X}}\phi, \qquad \nabla_{\mathbf{x}} \cdot \mathbf{g} = \frac{1}{J}\nabla_{\mathbf{X}} \cdot \left(J\mathbf{F}^{-1}\mathbf{g}\right), \tag{4.14}$$

where $\phi(\mathbf{x})$ and $\mathbf{g}(\mathbf{x})$ are arbitrary scalar and vector functions respectively. These can be obtained using the chain rule and Reynolds' transport theorem (Ogden, 1984). Hence we can use the identity $\nabla \cdot \nabla p = \nabla^2 p$ to rewrite the mass conservation equation (4.12),

$$\frac{1}{J}\nabla_{\mathbf{X}} \cdot \left(J\mathbf{F}^{-1}\mathbf{v}^s\right) - \frac{1}{J}\nabla_{\mathbf{X}} \cdot \left(J\mathbf{F}^{-T}\mathbf{F}^{-1}\left(\nabla_{\mathbf{X}}p\right)\right) = \bar{L}_p(\bar{P}_e - p), \tag{4.15}$$

where the solid velocity $\mathbf{v}^s$ is related to the rate of solid displacement by equation (4.9). The stress balance may be reformulated into a Lagrangian frame momentum equation (Howell *et al.*, 2009), so that

$$\nabla_{\mathbf{X}} \cdot \left(\mathbf{S}_e - pJ\mathbf{F}^{-T}\right) = 0, \tag{4.16}$$

where $\mathbf{S}_e = J\boldsymbol{\sigma}_e \cdot \mathbf{F}^{-T}$ is the effective first Piola-Kirchhoff stress.

For the boundary conditions, at the origin the system must exhibit symmetry:

$$\left.\frac{\mathrm{d}p}{\mathrm{d}R}\right|_{R=0} = 0, \qquad u|_{R=0} = 0. \tag{4.17}$$

As we are modelling just a region of tissue, rather than the full brain, the boundary conditions on the outer surface (at $R = H$) are more difficult to determine. We impose no displacement (representing that the tissue section is unable to move due to the skull and other brain structures) and a pressure dependent flux,

$$u(H) = 0, \qquad -K\frac{1}{f'}\left.\frac{\partial p}{\partial R}\right|_{R=H} = \Gamma\, p|_{R=H}\,, \tag{4.18}$$

where Γ is a parameter representing the ability of a fluid to be cleared from the tissue. This flux condition captures the observation that fluid drainage from the brain into the venous system occurs at a rate proportional to the pressure difference between brain and venous blood (Johanson, 2008). When considering a similar geometric setup to model an infusion test, other authors (eg. Chen and Sarntinoranont, 2007; Smith and Humphrey, 2007) have chosen to set $u = 0$, $p = 0$ on the outer boundary. That boundary condition models a scenario in which the outer boundary is sufficiently far from the infusion site that it is not affected, and it is not clear whether that assumption would be appropriate to edema. Note that in the limit of large Γ, (4.18) becomes equivalent to $p = 0$; we use the more general condition here to investigate how the pressure at the outer edge of the tissue is affected by the damage at the centre.

Non dimensionalisation

We non-dimensionalise the governing equations (4.16), (4.9) and (4.15), along with the boundary conditions (4.17) and (4.18). We rescale the variables,

$$\mathbf{x} = H\bar{\mathbf{x}}, \quad \mathbf{u} = H\bar{\mathbf{u}}, \quad p = (\lambda_s + 2\mu_s)\bar{p}, \quad t = \frac{H^2}{K(\lambda_s + 2\mu_s)}\bar{t}, \quad \mathbf{v}^s = \frac{K(\lambda_s + 2\mu_s)}{H}\bar{\mathbf{v}}^{\mathbf{s}}. \tag{4.19}$$

We choose the pressure scaling $\lambda_s + 2\mu_s$ to balance the pressure and strain in the stress balance (4.16): by this choice the dimensionless elastic parameters $\bar{\lambda_s} = \lambda_s/(\lambda_s + 2\mu_s)$, $\bar{\mu_s} = \mu_s/(\lambda_s + 2\mu_s)$ are of order 1. Time has been scaled using the poroelastic consolidation time scale. Then (dropping bars from the dimensionles variables) the mass conservation

and momentum balance governing equations may be rewritten,

$$\frac{1}{J}\nabla_{\mathbf{X}}\cdot\left(J\mathbf{F}^{-1}\mathbf{v}^s\right)-\frac{1}{J}\nabla_{\mathbf{X}}\cdot\left(J\mathbf{F}^{-T}\mathbf{F}^{-1}\left(\nabla_{\mathbf{X}}p\right)\right)=\bar{L}_p(\bar{P}_e-p), \tag{4.20}$$

$$\nabla_{\mathbf{X}}\cdot\bar{\mathbf{S}}_e=\nabla_{\mathbf{X}}\left(pJ\mathbf{F}^{-T}\right), \tag{4.21}$$

along with equation (4.9) (relating solid velocity and displacement rate) which remains unchanged:

$$\mathbf{v}^s=\left.\frac{\partial\mathbf{u}}{\partial t}\right|_{\mathbf{X}}. \tag{4.22}$$

The dimensionless Piola-Kirchhoff and Cauchy stress tensors are defined as $\bar{\mathbf{S}}_e=\mathbf{S}_e/(\lambda_s{+}2\mu_s)$ and $\bar{\boldsymbol{\sigma}}_e=\boldsymbol{\sigma}_e/(\lambda_s{+}2\mu_s)$ respectively. The symmetry boundary conditions at the origin (4.17) remain unchanged, whilst on the outer boundary (4.18) becomes

$$u(1)=0, \qquad -\frac{1}{f'}\left.\frac{\partial p}{\partial R}\right|_{R=1}=\bar{\Gamma}\,p|_{R=1}\,. \tag{4.23}$$

Dimensionless parameters are defined as,

$$\bar{\lambda_s}=\frac{\lambda_s}{(\lambda_s{+}2\mu_s)},\quad \bar{\mu_s}=\frac{\mu_s}{(\lambda_s{+}2\mu_s)},\quad \bar{L}_p=\frac{L_pH^2}{K},\quad \bar{P}_e=\frac{P_e}{(\lambda_s{+}2\mu_s)},\quad \bar{\Gamma}=\frac{\Gamma H}{K}. \tag{4.24}$$

Physically, $\bar{L}_p$ represents the ratio of the ease with which fluid can flow out from capillaries into tissue, versus the ease with which fluid can drain through the tissue over a distance H. Thus $\bar{L}_p\gg 1$ means that fluid can enter the tissue more easily than drain out, whilst $\bar{L}_p\ll 1$ means that fluid can drain out of the tissue more easily than it enters. The parameter $\bar{P}_e$ is the dimensionless driving pressure for transcapillary water movement, and $\bar{\Gamma}$ represents the ease with which fluid can flow out of the tissue boundary.

In §4.3 we shall investigate solutions to the model (4.20)-(4.23). However, first we discuss physiological parameter values relevant to this model.

4.2.4 Physiological parameter values

The elastic properties and hydraulic conductivity of brain tissue have been extensively investigated in the literature. The hydraulic permeability of brain tissue to water, K, is consistently found to be of order $10^{-12}-10^{-11}\mathrm{m}^2/\mathrm{Pa/s}$ (Chen and Sarntinoranont, 2007; Smillie *et al.*, 2005). For quasi-static deformations, the elastic parameters of brain tissue are approximately $\mu_s=216\mathrm{Pa}$, $\lambda_s=505\mathrm{Pa}$ (Taylor and Miller, 2004). The elastic parameters of brain tissue were discussed more thoroughly in §3.2.3 of Chapter 3.

Table 4.1: Summary of the dimensional parameters for the biphasic model of the brain. These values are discussed in §4.2.4. Throughout we take $H = 1$cm as a typical length scale in the system, as the maximum distance to the SAS or ventricles from within the brain tissue is of order of centimetres.

Dimensional			Dimensionless	
H	Radius of a tissue region	1cm	-	-
L_p	Capillary hydraulic permeability		$\bar{L}_p = L_p H^2/K$	
	Healthy:	10^{-9}–10^{-8}s^{-1}Pa^{-1}		0.1-1
	Damaged:	10^{-7}–10^{-6}s^{-1}Pa^{-1}		10-100
K	Tissue Darcy permeability	10^{-12}–10^{-11} m^{2}Pa^{-1}s^{-1}	-	-
μ_s, λ_s	Elastic parameters	216, 505 Pa	$\bar{\mu}_s = \mu_s/(\lambda_s+2\mu_s)$, $\bar{\lambda}_s = \lambda_s/(\lambda_s+2\mu_s)$	0.5, 0.25
P_e	Transvascular driving pressure	1000 Pa	$\bar{P}_e = P_e/\lambda_s+2\mu_s$	1
Γ	Permeability of the tissue boundary	††	$\bar{\Gamma} = \Gamma H/K$	††

†All pressures are given relative to the healthy SAS pressure

††As we are considering a local region of tissue in isolation, the appropriate value to use for the permeability of the tissue boundary is unknown. We consider a range of values for this parameter $\bar{\Gamma}$ in §4.3.3

There is less discussion in the literature of the capillary hydraulic permeability L_p, and therefore we consider this parameter in more depth. Recall that the hydraulic permeability L_p (Pa^{-1}s^{-1}) can be interpreted as the volumetric flow rate across from the capillary network into the tissue, per unit volume of tissue per unit pressure difference. In a compartment model of the brain, Rapoport (1978) uses 1.5×10^{-4}cm^{3}s^{-1}mmHg^{-1} as a bulk hydraulic permeability of the entire brain. Physically, this means the volumetric flow rate from the capillary network into the tissue, per unit pressure difference, for the entire brain (*i.e.* not per unit volume of tissue). To convert their value into our units, we divide by the brain volume: based upon a typical brain volume of 1500cm^3 this is yields to $L_p = 1 \times 10^{-7}$s^{-1}mmHg^{-1}. Bradbury (1985) summarised experimental results from the literature, noting that 0.8-1.5$\times10^{-9}$cm^3 s^{-1}mmH$_2$O^{-1} had been found for the hydraulic permeability per surface area of capillary. The typical capillary surface area per volume of brain tissue is 100-150cm^{2}g^{-1} in grey matter and one third that in white matter (Smith, 2003). Thus from the values of Bradbury (1985) we can estimate $L_p = 1-3\times10^{-6}$s^{-1}mmHg^{-1} in grey matter and $L_p = 3-10\times10^{-7}$s^{-1}mmHg^{-1} in white matter (note that 1mmHg=13.6mmH$_2$O). As these two approaches yield similar estimates for the capillary hydraulic permeability of healthy tissue, we take $L_p = 10^{-7}$–10^{-6}s^{-1}mmHg^{-1} (equivalent to 10^{-9}–10^{-8}s^{-1}Pa^{-1}). In damaged brain tissue, the capillary hydraulic permeability increases at least 100-fold (Rapoport, 1978).

The transvascular driving pressure P_e was defined as the capillary pressure less the osmotic pressure difference between blood and ISF. We use parameters of Rapoport (1997), but note that there is considerable uncertainty regarding this parameter (for example, the capillary pressure may not be constant everywhere). Per Rapoport (1997), the capillary pressure is 32mmHg greater than brain tissue pressure, and the osmotic

pressure difference across the BBB is 25mmHg. Thus the transvascular driving pressure is 7mmHg (approximately 1000Pa).

4.3 BBB failure in a local region of tissue

In this section, we present solutions to the biphasic model on a sphere, and discuss the role of dynamics, finite deformations, and boundary conditions.

4.3.1 Role of dynamics

In this section we consider a time-dependent model for swelling of a biphasic sphere, with constant capillary permeability $\bar{L}_p$ throughout. We are particularly interested in understanding the timescales which govern the behaviour of the system, because maximal edema is observed to occur after several days (Hatashita *et al.*, 1988; Marmarou *et al.*, 2000). If the model predicts that swelling would occur over a faster timescale, this would indicate that the dynamics must be governed by biological processes outside of the model.

We work with an infinitesimal deformation model which simplifies the governing equations, to allow us to focus on the dynamic evolution. In an infinitesimal elasticity framework, the Lagrangian ($\mathbf{X}$) and Eulerian ($\mathbf{x}$) co-ordinate systems are equivalent to leading order. The dimensionless governing equations (4.20) and (4.21) reduce to a coupled system for the displacement $\mathbf{u}$ and pore pressure p,

$$\frac{\partial}{\partial t}\left(\nabla \cdot \mathbf{u}\right) - \nabla^2 p = \bar{L}_p\left(\bar{P}_e - p\right), \tag{4.25}$$

$$\nabla p = \nabla \cdot \left[\bar{\lambda}_s \mathrm{tr}(\mathbf{e}) + 2\bar{\mu}_s \mathbf{e}\right], \tag{4.26}$$

where $\mathbf{e} = [\nabla\mathbf{u} + (\nabla\mathbf{u})^T]/2$ is the linear strain tensor, and we have substituted the infinitesimal stress tensor $\bar{\boldsymbol{\sigma}}_e = \bar{\lambda}_s \mathrm{tr}(\mathbf{e})\mathbf{I} + 2\bar{\mu}_s\mathbf{e}$ into the stress balance (4.26). We define $e = \mathrm{tr}(\mathbf{e}) = \nabla \cdot \mathbf{u}$ as a measure of local strain.

We impose the initial conditions that both pressure and displacement are zero initially,

$$u(r,0)=0, \qquad\qquad p(r,0)=0. \tag{4.27}$$

We choose the specific case $1/\bar{\Gamma} = 0$ for our boundary condition on the outer edge (4.23) (meaning that there is no resistance to fluid flow through the outer boundary), so that $u = 0$, $p = 0$ at $r = 1$, along with symmetry at the origin (4.17). In §4.3.3 we will investigate the effect of varying $\bar{\Gamma}$.

We choose these simple boundary and initial conditions to gain insight into the behaviour of the system. Trivially, it can be observed that if $\bar{L}_p = 0$ (*i.e.* the capillaries are

completely impermeable to water) then $p = 0$, $\mathbf{u} = \mathbf{0}$ is a solution that satisfies the specified boundary conditions. Therefore the set up we consider may be thought of as a region of undeformed tissue undergoing an instantaneous increase in capillary permeability at time $t = 0$.

From the dimensionless governing equations, we now identify the appropriate short and long time behaviour. Over both short ($t \ll 1$) and long ($t \gg 1$) timescales, we rescale the variables so that they are of order 1 in the regime that we are investigating. Upon substituting these rescaled variables into the governing equations, we can then identify which terms of the governing equations will dominate in each regime. This rescaling allows us to understand the effect of different parameters on the behaviour of the system.

Short time

The initial conditions (4.27) indicate that over short time, the pressure and displacement are small. This motivates the scalings,

$$t = \varepsilon \hat{t}, \qquad p = \varepsilon \hat{p}, \qquad \mathbf{u} = \varepsilon \hat{\mathbf{u}}, \tag{4.28}$$

for some $\varepsilon \ll 1$ where $\hat{t}$, $\hat{p}$, $\hat{u}$ are short time variables. Then the mass conservation governing equation may be written,

$$\frac{\partial}{\partial \hat{t}} \left(\nabla \cdot \hat{\mathbf{u}} \right) - \varepsilon \nabla^2 \hat{p} = \bar{L}_p \left(\bar{P}_e - \varepsilon \hat{p} \right). \tag{4.29}$$

Since $\varepsilon \ll 1$, equation (4.29) indicates that the dominant balance at short times is between the first term on the left hand side, and first term on the right hand side. Therefore for $t \ll 1$ we would expect the strain $e = \nabla \cdot \mathbf{u}$ to increase at a constant rate, $\bar{L}_p \bar{P}_e$. Hence,

$$\nabla \cdot \hat{\mathbf{u}} = \bar{L}_p \bar{P}_e \hat{t}, \tag{4.30}$$

for $t \ll 1$ (where we have used the initial condition $\mathbf{u} = \mathbf{0}$ at $t = 0$ to remove the constant of integration). The corresponding pressure is found by solving equation (4.26).

Long time

Over longer timescales, the system reaches a steady state. The time taken for the system to reach this steady state depends on the parameter regime of the system. The dimensionless parameter $\bar{L}_p = L_p H^2 / K$ represents the ratio of the ease at which fluid can enter the tissue from the capillary, relative to the ease with which fluid can drain out through the tissue a distance H to the boundary. We consider in particular the limits $\bar{L}_p \ll 1$

and $\bar{L}_p \gg 1$.

$\bar{L}_p \ll 1$

When $\bar{L}_p \ll 1$, the mixture is sufficiently permeable that water is able to drain out of the system at pressures below the capillary driving pressure $\bar{P}_e$. Thus we anticipate a dominant balance between the source of fluid entering from capillaries, and fluid drainage out through the tissue at steady state. We scale for long time,

$$t = \tilde{t}, \qquad p = \bar{L}_p \bar{P}_e \tilde{p}, \qquad \mathbf{u} = \bar{L}_p \bar{P}_e \tilde{\mathbf{u}}, \tag{4.31}$$

where $\tilde{t}$, $\tilde{p}$, $\tilde{u}$ are long time variables and find,

$$\frac{\partial}{\partial \tilde{t}} (\nabla \cdot \tilde{\mathbf{u}}) - \nabla^2 \tilde{p} = 1 - \bar{L}_p \tilde{p}. \tag{4.32}$$

Since $\bar{L}_p \ll 1$, this indicates that we can neglect the last term in (4.32) and the dominant balance is indeed between the flux of fluid draining out of the system and fluid entering the system from capillaries as anticipated. The pressure in the system will be of order $\bar{L}_p \bar{P}_e$. Furthermore, we would expect the system to evolve over an order 1 timescale, independent of $\bar{L}_p$.

$\bar{L}_p \gg 1$

When $\bar{L}_p \gg 1$ we expect the pressure to approach the capillary driving pressure $\bar{P}_e$, as we anticipate that at steady state the dominant balance in the mass conservation equation (4.25) will be between the two terms on the RHS. We instead scale for long time variables to reflect this expectation,

$$t = \bar{L}_p \tilde{t}, \qquad p = \bar{P}_e \tilde{p}, \qquad \mathbf{u} = \bar{P}_e \tilde{\mathbf{u}}, \tag{4.33}$$

so that

$$\frac{\partial}{\partial \tilde{t}} (\nabla \cdot \tilde{\mathbf{u}}) - \frac{1}{\bar{L}_p} \nabla^2 \tilde{p} = 1 - \tilde{p}. \tag{4.34}$$

Since $\bar{L}_p \gg 1$, at steady state the dominant balance in the above equation is between the terms on the right hand side. This implies that $\tilde{p} \approx 1$ (*i.e.* $p \approx \bar{P}_e$) at steady state. Furthermore, the time scaling indicates that the time taken for the system to reach equilibrium is proportional to $1/\bar{L}_p$.

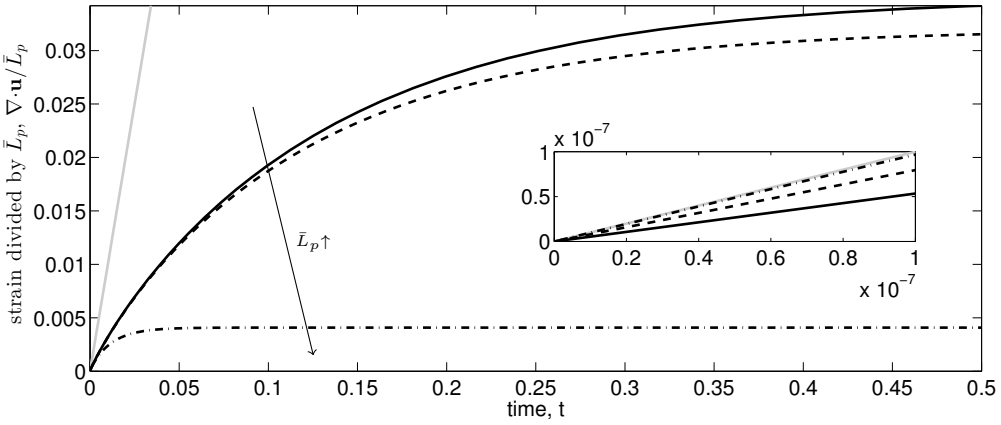

Figure 4.3: Black curves: strain scaled by $\bar{L}_p$, $\nabla \cdot \mathbf{u}/\bar{L}_p$, against time for a biphasic model with capillary source in a spherical geometry. The strain shown is at the centre of the sphere. Grey lines are $\bar{P}_e t$, and the inset figures show that for very short times strain satisfies (4.30). Parameter values are: $\bar{\lambda}_s = 0.5$, $\bar{\mu}_s = 0.25$, $\bar{P}_e = 1$, and curves are shown for $\bar{L}_p = 0.01$ (solid), $\bar{L}_p = 1$ (dashed) and $\bar{L}_p = 100$ (dot-dashed) with the arrow in direction of increasing $\bar{L}_p$. For each of these simulations the spatial domain [0, 1] was discretised into $N = 100$ gridpoints and the system was solved using the Method of Lines, as described in §4.3.1.

Validation of dimensional analysis

We now solve the time-dependent biphasic problem (4.25)-(4.26) numerically, and compare these numerical results to the predictions for the rate of evolution of the system from our dimensional analysis. In a spherically symmetric geometry, equations (4.25)-(4.26) may be rewritten,

$$(\bar{\lambda}_s + 2\bar{\mu}_s)\frac{\partial}{\partial r}\left(\frac{1}{r^2}\frac{\partial}{\partial r}\left(r^2 u\right)\right) = \frac{\partial p}{\partial r}, \tag{4.35}$$

$$\frac{\partial}{\partial t}\left(\frac{1}{r^2}\frac{\partial}{\partial r}\left(r^2 u\right)\right) - \frac{1}{r^2}\frac{\partial}{\partial r}\left(r^2\frac{\partial p}{\partial r}\right) = \bar{L}_p\left[\bar{P}_e - p\right], \tag{4.36}$$

where $u = \mathbf{u}\cdot\mathbf{e}_r$ is the radial displacement. We solve equations (4.35)-(4.36), subject to initial conditions $p(r,0)$=0 and $u(r,0)$=0, and boundary conditions $p(t,1)$=0, $u(t,1)$=0, numerically using the Method of Lines. The Method of Lines is a technique for solving partial differential equations, whereby the equations are discretised in space, with the time variable left continuous. This leads to a system of time-dependent ordinary differential equations, which can then be solved numerically or analytically. We discretise each governing equation in space using a second-order central finite difference method. This results in a system of differential algebraic equations, which we solved using the Matlab solver 'ode15s'.

In Figure 4.3 we show numerical results for the evolution of strain (at the centre of a sphere), for three different values of $\bar{L}_p$. The inset figures show that in each case the strain initially increases linearly with time, with slope $\bar{L}_p\bar{P}_e$. When $\bar{L}_p = 1$ and $\bar{L}_p = 0.01$ the time taken for the system to evolve to steady state equilibrium is similar, whilst for $\bar{L}_p = 100$ the system evolves to equilibrium very rapidly.

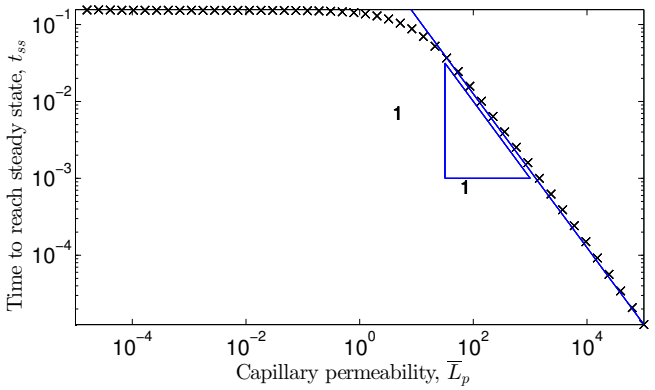

Figure 4.4: Plot showing the time taken for the pressure of a biphasic system to reach within $1/e$ of its steady state value, t_{ss}, as a function of the dimensionless capillary permeability $\bar{L}_p$. The crosses show results of these numerical simulations, whilst the solid curve is a line of best fit for $\bar{L}_p \gg 1$ such that $t_{ss} = 1.25/\bar{L}_p$.

We now test our assertion that if $\bar{L}_p \ll 1$ then the time taken for the system to evolve to equilibrium is of order 1 independent of $\bar{L}_p$, whilst if $\bar{L}_p \gg 1$ then the time taken to evolve to equilibrium is of order $1/\bar{L}_p$. Figure 4.4 shows the time taken for the pressure (at the centre of a sphere) to reach within $1/e$ of its equilibrium value, t_{ss}. As expected we observe that when $\bar{L}_p \ll 1$, t_{ss}=constant, whilst when $\bar{L}_p \gg 1$ then $t_{ss} \sim 1/\bar{L}_p$.

We now consider the relevance of these timescales to brain tissue swelling. In §4.2.3 we employed the poroelastic timescale, $\tau = H^2/K/(\lambda_s + 2\mu_s)$ to non-dimensionalise time. This takes values $\tau = 10^4 - 10^5$s (equivalent to 1 hour $-$ 1 day) for the physiological parameter values relevant to our system (see Table 4.1). Furthermore, in tissue with a damaged BBB, $\bar{L}_p = 10 - 100$.

In this section, we have shown that when $\bar{L}_p > 1$, the system will evolve over the dimensional time scale $t \sim \tau/\bar{L}_p$. Therefore the model suggests that tissue swelling due to a damaged BBB should evolve over a time scale of $\tau/\bar{L}_p = 10^2 - 10^4 s$ (1 minute $-$ 1 hour). However, maximal swelling is observed to develop over the time scale of days physiologically (Hatashita *et al.*, 1988; Marmarou *et al.*, 2000). Thus the time scale predicted by the model is more rapid than that observed biologically, suggesting that the rate of swelling is governed by biological processes (such as the rate at which the BBB becomes permeable) rather than physical processes. As it appears that this model is unable to offer insight into the rate of swelling, we neglect dynamics for the remainder of this chapter,

and instead focus on the final damaged equilibrium state.

4.3.2 Role of finite deformations

Previous authors have used a similar biphasic modelling approach to investigate the mechanical behaviour of brain tissue (Nagashima *et al.*, 1990; Smith and Humphrey, 2007), although a model valid for only infinitesimal deformations was used. We next investigate the difference in stress and strain distributions obtained when using an infinitesimal vs. finite deformation model.

We consider the effect of a local damaged region on the tissue, by simulating a local region of damage towards the centre of the tissue by imposing a step function for $\bar{L}_p(R)$:

$$\bar{L}_p(R) = \begin{cases} 10 & R < 0.2, \\ 0.1 & R > 0.2, \end{cases} \tag{4.37}$$

where these parameter values are chosen to reflect capillary permeability in tissue with a healthy and damaged tissue BBB respectively (see Table 4.1). As our dimensional analysis in §4.3.1 indicates that it is biological rather than mechanical processes which govern the timescale over which swelling develops, we consider only equilibrium solutions.

For the infinitesimal deformation model, the governing equations are (4.35) and (4.36) in steady state. For the finite-deformation governing equations, we substitute the spherically symmetric deformation gradient tensor (4.13) into the Lagrangian form of the governing equations (4.20, 4.21), and use standard spherical vector operators (for example Howell *et al.*, 2009). We then obtain the following equation for mass conservation at steady state,

$$-\frac{1}{J}\frac{1}{R^2}\frac{\partial}{\partial R}\left(\frac{R^2 J}{f'^2}\frac{\partial p}{\partial R}\right) = \bar{L}_p(R)(\bar{P}_e - p). \tag{4.38}$$

Similarly we write the Lagrangian stress balance (4.21)

$$0 = \frac{\mathrm{d}(S_{RR})}{\mathrm{d}R} + \frac{2(S_{RR} - S_{\Theta\Theta})}{R} - \frac{f^2}{R^2}\frac{\mathrm{d}p}{\mathrm{d}R}, \tag{4.39}$$

where S_{RR} and $S_{\Theta\Theta}$ are the diagonal components of the dimensionless Piola-Kirchhoff stress $\bar{\mathbf{S}}_e$.

In §2.3.3 of Chapter 2, we investigated the behaviour due to several strain energy functions. We showed that over moderate deformations (volume changes of up to 20%), the neo-Hookean, Fung and Ogden models show quantitatively similar behaviour for parameters relevant to the brain. Therefore, for simplicity we consider a neo-Hookean

strain energy. The components S_{RR} and $S_{\Theta\Theta}$ required for the stress balance (4.39) may be written as functions of the radial deformation $f(R)$:

$$S_{RR} = \frac{1}{f'}\left[\bar{\mu}_s(f'^2 - 1) + \bar{\lambda}_s J(J-1)\right], \tag{4.40}$$

$$S_{\Theta\Theta} = \frac{R}{f}\left[\bar{\mu}_s\left(\left(\frac{f}{R}\right)^2 - 1\right) + \bar{\lambda}_s J(J-1)\right]. \tag{4.41}$$

To solve these steady state governing equations for a step function for $\bar{L}_p(R)$, we use a multipoint boundary value solver in Matlab. Details are given in Appendix B.

In Figure 4.5, we compare profiles for the radial and compressive stretch and compressive stress through a region of tissue, obtained using the infinitesimal and finite deformation models. We observe that whilst the results show quantitatively different behaviour, qualitatively the behaviour is similar. This suggests that despite strains greater than 5% (typically assumed to be the greatest strains for which the infinitesimal model is valid), the infinitesimal theory can still offer insight into the behaviour of the tissue.

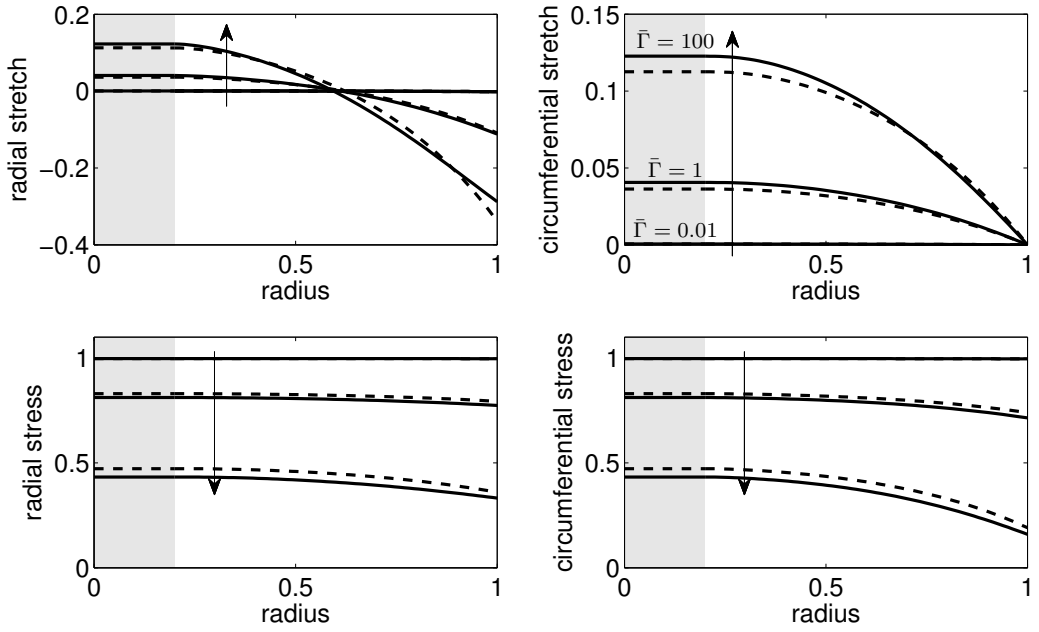

Figure 4.5: Profiles of stretch and compressive stress calculated using the finite deformation (solid curves) and infinitesimal deformation (dashed curves) models, for $\bar{\Gamma} = 0.01, 1, 100$ (arrow in direction of increasing $\bar{\Gamma}$). Profiles are shown for radial and circumferential stretch and stress, as these are the measures that we use as a proxy for tissue damage. We observe that the finite and infinitesimal models display qualitatively similar behaviour for all values of $\bar{\Gamma}$. Parameters: $\bar{P}_e = 1$, $\bar{\lambda}_s = 0.5$, $\bar{\mu}_s = 0.25$.

4.3.3 Role of boundary conditions

We are interested in two types of damage: 'strain damage', whereby the tissue is stretched (causing mechanical damage to axons), and 'stress damage', whereby the tissue stress could compress the capillary network (leading to reduced blood flow and hypoxia). As it is unclear what value of the parameter $\bar{\Gamma}$ (representing the ease with which fluid can flow out of the tissue in the CSF) is relevant to the brain, we are particularly interested to investigate how the value of $\bar{\Gamma}$ affects the type of damage caused.

In Figure 4.6 we show dilation, radial and circumferential strain, pore pressure and radial and circumferential compressive stress profiles through the tissue. Curves are shown for different values of the $\bar{\Gamma}$ parameter. The upper row of Figure 4.6 shows quantities associated with 'strain damage'. We observe that when $\bar{\Gamma}$ is large, so that fluid can easily flow from the tissue, larger strains occur in the tissue. The dilation profiles show that the inner region swells, whilst the outer region is compressed. However, considering the radial and circumferential strains shows that the entire tissue is stretched circumferentially, whilst the inner region expands and outer region contracts radially. When $\bar{\Gamma}$ is small, there is little strain in either direction and the tissue experiences little volume change. Therefore, Figure 4.6 suggests that strain damage to tissue is worsened when fluid can flow easily out of the tissue (*i.e.* for large $\bar{\Gamma}$.).

The lower row of Figure 4.6 concerns quantities associated with 'stress damage'. Note in particular that we have plotted the **compressive** radial and circumferential Cauchy stresses (corresponding to $-\mathbf{e}_r \cdot \boldsymbol{\sigma} \cdot \mathbf{e}_r$ and $-\mathbf{e}_\theta \cdot \boldsymbol{\sigma} \cdot \mathbf{e}_\theta$ respectively). Regardless of the value of $\bar{\Gamma}$, we observe that pore pressure approaches the driving pressure $\bar{P}_e$ (set equal to 1 in these simulations) in the center of the tissue. However, we observe that when $\bar{\Gamma}$ is smaller (so that fluid cannot easily flow from the tissue), the compressive stress experienced by the tissue is greater than when $\bar{\Gamma}$ is larger. This suggests that fluid being unable to escape from the tissue leads to an increase in the 'stress damage' experienced by the tissue. We note that this simple geometry does not lead to shear stress, which is an important cause of tissue damage.

Thus, Figure 4.6 suggests that there is a non-trivial balance between the stress and strain in the tissue. Figure 4.7 shows the maximum compressive stress and maximum strain occurring in the peripheral tissue with intact BBB ($0.2 < R < 1$), as a function of $\bar{\Gamma}$. If $\bar{\Gamma}$ is large, the peripheral tissue is subjected to large strains (due to pressure gradients through the tissue), yet the overall compressive stress experienced by the tissue is small. However if $\bar{\Gamma}$ is small (so fluid can only drain slowly out of the tissue) then the peripheral undergoes little strain (as pressure gradients are small), yet the compressive stress is high everywhere. This suggests that a local increase in capillary permeability could lead to peripheral tissue experiencing 'stress damage' or 'strain damage', with the

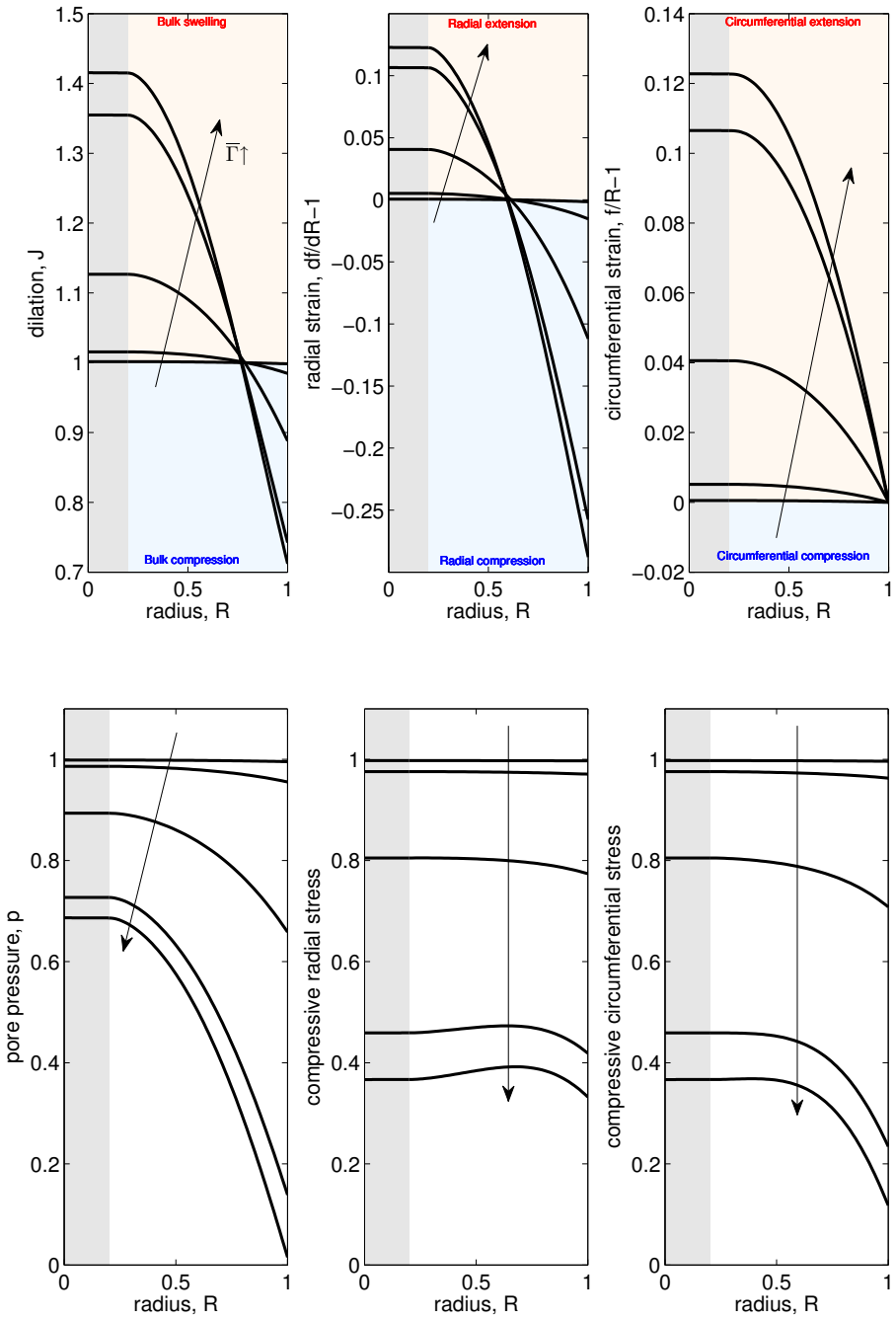

Figure 4.6: Solution profiles for the biphasic model with a local region of damage at the centre. Top row shows dilation ($J = f^2 f'/R^2$), radial strain ($f' - 1$) and circumferential strain ($f/R - 1$), whilst bottom row shows pore pressure (p), radial compressive stress ($-\mathbf{e}_r \cdot \boldsymbol{\sigma} \cdot \mathbf{e}_r$), and circumferential compressive stress ($-\mathbf{e}_\theta \cdot \boldsymbol{\sigma} \cdot \mathbf{e}_\theta$). Curves show profiles for tissue which has a damaged BBB towards the centre, so that capillary permeability is $\bar{L}_p$=10 for $0 < R < 0.2$ (grey shaded region), and $\bar{L}_p$=0.1 for $0.2 < R < 1$ (white shaded region). Each curve corresponds to a particular value of $\bar{\Gamma}$=0.01, 0.1, 1, 10, 100, with the arrows in the direction of increasing $\bar{\Gamma}$. Parameters: $\bar{P}_e = 1$, $\bar{\lambda}_s = 0.5$, $\bar{\mu}_s = 0.25$.

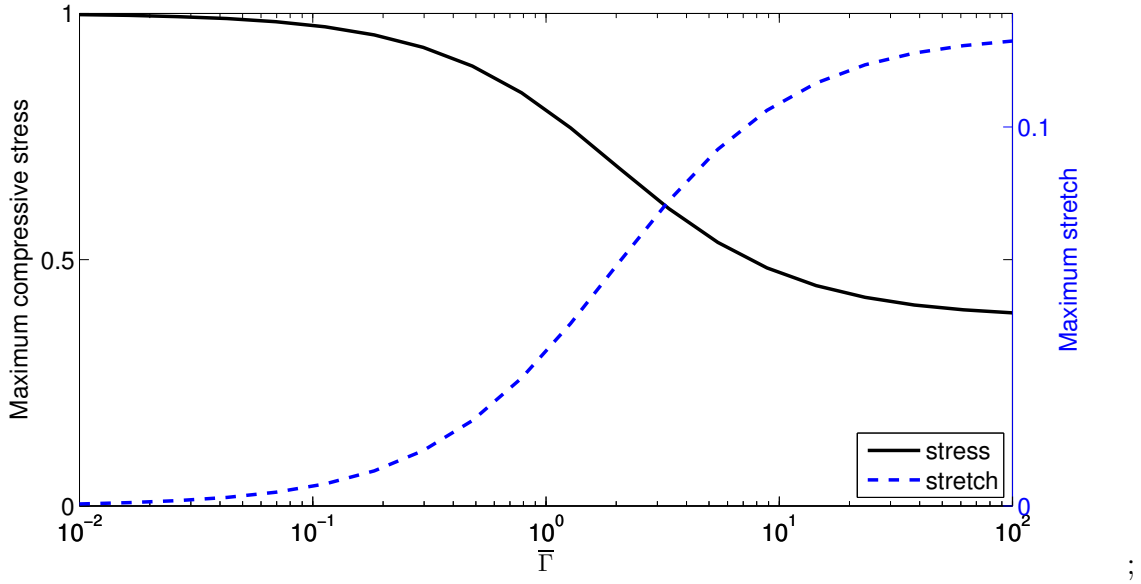

;

Figure 4.7: Maximum compressive stress (black solid curve, left axis) and maximum stretch (blue dashed curve, right axis) experienced by the peripheral tissue ($0.2 < R < 1$), as a function of $\bar{\Gamma}$. All parameters as in Figure 4.6

type of damage occurring depending on how fluid drains from the system.

4.4 Discussion

We have investigated a biphasic model for interstitial fluid flow through a region of brain tissue. Whilst we have used a simpler geometry than previous modelling attempts (Nagashima *et al.*, 1990), we are able to offer insight into the role of key parameters of the system. In particular, the dimensionless parameter $\bar{L}_p = L_p H^2/K$, representing the ease at which fluid can flow out of a capillary versus the ease at which fluid can permeate a distance H through the tissue, is important to the behaviour of the system. Physiological parameter values indicate that healthy brain tissue (with an intact BBB) operates in the regime $\bar{L}_p < 1$ whilst damaged brain tissue (with a more permeable BBB) operates in the regime $\bar{L}_p > 1$.

Dimensional analysis of the model suggests that when $\bar{L}_p \ll 1$ the pore pressure in the tissue remains low, whilst when $\bar{L}_p \gg 1$ the pore pressure can increase up to the capillary driving pressure. This observation offers an interesting insight into how changes in BBB permeability alone can lead to edema. Furthermore, through dimensional analysis we have shown that the timescale for swelling predicted by the model is more rapid than the timescale of edema formation observed experimentally. This suggests that the rate of edema formation is determined by biological factors outside the scope of this model

(such as the rate of breakdown of the BBB), rather than by mechanical factors alone.

Subsequently we considered steady state solutions for a spherical tissue, with an inner region with a damaged BBB ($\bar{L}_p > 1$), and outer healthy region ($\bar{L}_p < 1$). The aim here was to investigate whether a locally damaged region of tissue can have consequences for surrounding healthy tissue. Where fluid was able to flow freely out of the tissue at the outer boundary (*i.e.* the parameter $\bar{\Gamma}$, controlling the ease at which fluid could flow from the tissue, was large), large pressure gradients and strains were observed within the surrounding healthy tissue. Where fluid flux out of the tissue at the outer boundary was limited (low $\bar{\Gamma}$), the surrounding healthy tissue experienced high compressive stress (although the strains in the tissue remained low). This indicates that a local increase in capillary permeability can cause damage in surrounding healthy tissue, since both high stresses (which restrict blood flow) and deformations (which cause mechanical damage to axons) may be experienced.

In using the form $Q^w = L_p(P_e - p)$ for the source term for fluid transport from capillaries, we made two major assumptions. Firstly, we assumed that the transvascular driving pressure P_e is constant, and thereby that the capillary pressure and osmotic pressure difference across the BBB remain constant. The brain has an auto-regulation mechanism for blood flow, and is able to maintain flow to the brain over a range of intracranial pressures: therefore pressure in the vascular system may change during the onset of swelling. Additionally, increases in osmotic pressure of the brain tissue are observed during swelling. However, an advantage of our simplistic approach is that we are able to offer a clear insight into the parameters governing the behaviour of the model: when capillary permeability L_p is high the tissue pressure can increase up to the capillary driving pressure P_e, whilst when capillary permeability is low the system is less sensitive to this parameter.

Our second major assumption is that there is always enough fluid in the capillaries to allow the capillaries to act as a fluid source. If the compressive stresses in the tissue approach capillary pressure, we may expect that capillaries become compressed and hence less fluid to be available in the capillaries to enter the tissue. As discussed in §4.1.2 of the introduction, the danger of increased intracranial pressure is a reduction in blood flow. To explicitly model this effect, the capillary network could be modelled as a further fluid phase (for example, using the multi-network poroelastic approach of Tully and Ventikos (2011)), or the form of the transvascular fluid source (4.11) could be adapted to allow capillaries to close if they experience high compressive stress. We explore the concept of capillaries closing due to compressive stress further in Chapter 5. We note, however, that the constitutive form of our source term is actually compatible with the concept that less fluid enters the tissue as fluid pressure increases. In a 'worst case scenario', if the BBB

became completely permeable to solutes or solute concentrations equilibrate on either side of the BBB, the transvascular driving pressure P_e would be purely due to the capillary pressure. Thus as tissue pressure approaches capillary pressure, the pressure difference across the BBB ($P_e - p$), tends to 0. Consequently the capillary source, $Q^w = L_p(P_e - p)$, also becomes small.

In the brain, changes in tissue osmolarity are observed alongside edema. Throughout this chapter we have neglected osmotic effects, by encapsulating the osmotic pressure difference between capillary and brain in the transvascular driving pressure parameter P_e. Analysis of our mathematical model indicates that when the BBB is highly permeable ($\bar{L}_p > 1$), the model is sensitive to P_e; this suggests that inclusion of osmotic effects is important to gain a better understanding of brain edema. Incorporating osmotic effects, such as an accumulation of ions caused by an exposed FCD (as in Chapter 3), may also be necessary to fully capture the underlying behaviour of this system.

Chapter 5

Propagation of damage

5.1 Introduction

Local edema can cause tissue damage to propagate through healthy brain tissue (Gerriets *et al.*, 2004). This occurs because the swollen tissue occupies additional space within the brain, which can result in mechanical deformation, compression of blood vessels and high intracranial pressure (ICP) in the previously healthy tissue surrounding the swollen region. This surrounding tissue subsequently suffers from lack of blood flow, which leads to ischemia and ultimately cell death. This death could in turn lead to further swelling and hence the propagation of damage that is the subject of this chapter. A schematic of this process is shown in Figure 5.1.

Craniectomy (the removal of a portion of the skull) is a procedure performed to reduce high pressure in the brain, and improve blood flow in a swollen brain (Cooper *et al.*, 2011). The idea is that the brain is allowed to increase in volume so that the adverse compression caused by swelling can be (partially) removed. An interesting experimental paper of Walberer *et al.* (2008) highlighted the consequences of the space occupying effect of edema, by comparing the spread of edema in rats with a craniectomy to those with an intact skull. A stroke was induced in one hemisphere, and the volume of infarcted (dead) tissue and midline shift[1] were measured after 5 and 24 hours. At both time points, the rats that had undergone craniectomy showed less midline shift, and had a smaller volume of infarcted tissue than those with an intact skull. The authors suggest that the craniectomy contributed to a better outcome because the brain tissue could swell outwards, preventing the regional compression of blood vessels to the area surrounding the originally infarcted region. However, craniectomy is also associated with negative outcomes, due to the additional stretching and deformation of neurons.

In this chapter, we aim to develop a mathematical model to investigate the propaga-

[1]Midline shift measures how far the centreline of the brain, between the two hemispheres, has moved.

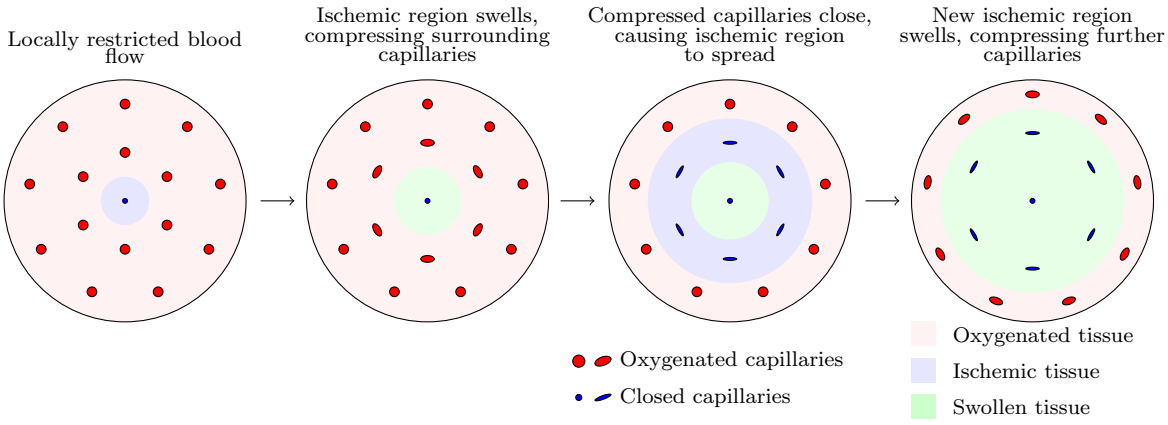

Figure 5.1: Schematic of the mechanism by which local ischemia can cause the ischemic region to propagate through the brain

tion of damage through the brain. We are particularly interested to understand whether changing the boundary conditions on the outer edge of our domain, to represent either the intact skull or a craniectomy, can affect how far damage propagates through the brain.

5.2 Mathematical modelling approach

In chapter 3, we investigated mechanisms for tissue damage, whereby intracellular FCD is exposed in damaged brain tissue. This exposed FCD induces an ion concentration difference between the damaged tissue and its surroundings (the Donnan effect), resulting in an osmotic pressure difference, water accumulation, and hence swelling.

In this chapter, we incorporate the exposure of intracellular FCD into a coupled model for the deformation of, and oxygen distribution through, a region of tissue. The tissue will be modelled as a triphasic mixture (consisting of a charged solid, fluid, and positive and negative ion phases) together with a diffusion-uptake model for the oxygen concentration within the tissue. Capillaries are located throughout the tissue, and provide a source of oxygen when they are open. We model the effect of deformation on oxygen supply by assuming that capillaries close when they experience a compressive stress above a critical threshold. The oxygen distribution then feeds back into the tissue mechanics, as we assume that the tissue becomes infarcted and develops an FCD wherever the oxygen concentration falls below a critical threshold.

We shall use an equilibrium model to describe both the tissue mechanics and oxygen distribution. This is appropriate because our earlier calculations have shown that the timescales for water, ion and oxygen movement through the tissue are significantly shorter than the timescale for the evolution of edema observed experimentally. This suggests that it is the rate of tissue damage, for example the rate at which ischemic tissue dies

and exposes the intracellular FCD, rather than mechanical effects (such as the rate of interstitial fluid movement, or oxygen diffusion), that govern the evolution of edema.

To examine this hypothesis, we employ an iterative model for the evolution of edema. At stage n, we compute the region within which the capillaries are expected to be compressed. Subsequently in stage $n+1$ we close these capillaries, find the new infarcted region within which the oxygen concentration has fallen below a critical threshold, and recompute the stresses in the tissue with the new FCD distribution. This iteration process is discussed in detail in §5.2.5. Beforehand, in §5.2.1, we discuss the model geometry that we shall use, and in §5.2.2 and §5.2.3 we discuss governing equations for an equilibrium triphasic model and diffusion-uptake of oxygen on a deformable domain.

5.2.1 Geometry

On first thought, it is natural to consider investigating a one-dimensional Cartesian geometry. However, in this geometry the stress balance, $\nabla \cdot \boldsymbol{\sigma} = \mathbf{0}$, can be integrated to yield that the compressive Cauchy stress, $-\boldsymbol{\sigma}$, is constant throughout the tissue. Therefore, regardless of the presence of an inhomogeneous distribution in FCD, a one-dimensional Cartesian co-ordinate system is unable to capture spatial gradients of stress and pressure that are observed following local edema (Reulen *et al.*, 1977). Furthermore such a model would be unable to capture the propagation of damage through the tissue, since either the entire tissue would be sufficiently compressed that no capillaries receive oxygen, or the entire tissue would receive sufficient oxygen.

The subtlety is not present in a spherically symmetric geometry and so we consider a spherically symmetric region of tissue, of outer radius H. This is the simplest geometry that is able to reproduce the spatial variations in compressive stress that are observed in the brain. The tissue is bathed in a fluid of ionic concentration c^*, with reference pressure $p = 0$, representing the cerebrospinal fluid (CSF) that surrounds the brain. We assume that capillaries are evenly spaced throughout the tissue a distance H_{cap} apart. Hence there are $N = H/H_{cap}$ capillaries in the domain $R \in [0, H]$, with the first capillary at radius $R = H_{cap}/2$, and the ith capillary at position $R_{cap_i} = (i - 1/2)H_{cap}$ $(i = 1 \dots N)$. We will not model the mechanical behaviour of the capillaries, but rather treat each capillary as a point source of oxygen. We note that the spherically symmetric geometry means that the capillaries are actually 'rings' of capillary rather than individual vessels.

5.2.2 Mechanics

The tissue is described in the Lagrangian (reference) configuration by the material coordinates $\mathbf{X} = R\hat{\mathbf{E}}_r$, and in the Eulerian (current) configuration by $\mathbf{x} = r\hat{\mathbf{e}}_r$. To investigate

the mechanical deformation of the tissue, we seek a spherically symmetric deformation of the form $r = f(R)$. Then $\hat{\mathbf{E}}_r = \hat{\mathbf{e}}_r$ and the deformation gradient tensor may be written

$$\mathbf{F} = \nabla_{\mathbf{X}}\mathbf{x} = \begin{pmatrix} f' & 0 & 0 \\ 0 & \dfrac{f}{R} & 0 \\ 0 & 0 & \dfrac{f}{R} \end{pmatrix}, \qquad J = \det(\mathbf{F}) = \frac{f^2 f'}{R^2}, \tag{5.1}$$

where $'$ denotes differentiation with respect to R. This is the same geometry used to investigate the effect of blood brain barrier failure in Chapter 4 (*cf.* §4.2.3).

We assume that the tissue consists of a triphasic mixture with a charged solid phase, fluid phase, and positive and negative ion species in solution. At each iteration the reference state FCD, $c_0^f(R)$, will be determined from the steady state oxygen distribution given a certain level of damage (see §5.2.5).

The governing equations for a triphasic mixture at equilibrium were discussed in Chapters 2 and 3, and we recap them here. The stress balance reads,

$$\nabla \cdot \boldsymbol{\sigma}_e = \nabla p, \tag{5.2}$$

where p is the pore pressure and $\boldsymbol{\sigma}_e$ is the effective stress, which is related to a strain energy function $W(\boldsymbol{F})$ by $\boldsymbol{\sigma}_e = (1/J)\boldsymbol{F} \cdot \partial W/\partial \boldsymbol{F}$. The Cauchy stress is $\boldsymbol{\sigma} = \boldsymbol{\sigma}_e - p\mathbf{I}$

As the mixture is at equilibrium, there is no fluid flux through the tissue. Thus the chemical potential of solvent (refer to equation (2.21)) is constant, so that the pore pressure is proportional to the osmotic pressure,

$$p = RT\left[(c^+ + c^-) - c^*\right], \tag{5.3}$$

where R is the ideal gas constant, T the absolute temperature, and c^+, c^-, c^* the concentrations of positive and negative ions in the tissue, and the bathing solution, respectively. At equilibrium the concentrations c^+, c^- are determined by the Donnan equilibrium (see §2.3.2),

$$c^+ + c^- = \sqrt{c^{*2} + c^{f\,2}}, \tag{5.4}$$

where c^f is the FCD. As this FCD is attached to the solid phase, the FCD is dependent upon the deformation of the solid phase,

$$c^f = \frac{\phi_0^w c_0^f(R)}{J - 1 + \phi_0^w}, \tag{5.5}$$

where ϕ_0^w is the reference state fluid volume fraction.

We now eliminate p, c^f, c^+ and c^- from equations (5.2)-(5.5) to yield a single differential equation for the deformation $f(R)$. Combining equations (5.2)-(5.4), we find that the divergence of the effective stress tensor balances with the gradient of the osmotic pressure,

$$\nabla \cdot \boldsymbol{\sigma}_e = RT\nabla \left(\sqrt{c^{*2} + \left(\frac{\phi_0^w c_0^f(R)}{J - 1 + \phi_0^w} \right)^2} \right). \tag{5.6}$$

We observe that the effective stress $\boldsymbol{\sigma}_e$ and dilation J are both functions of the deformation. Thus equations (5.2)-(5.5) are replaced by a single equation for $f(R)$ governing the displacement of the system.

Equation (5.6) contains derivatives in the Eulerian configuration. We map the equations into the Lagrangian configuration so that the system may be solved on the fixed reference domain $R \in [0, H]$ rather than the deformed current domain. The stress balance may be reformulated into a Lagrangian frame momentum equation (*e.g.* Howell *et al.*, 2009) so that,

$$\nabla_{\mathbf{X}} \cdot \mathbf{S}_e = RT\nabla_{\mathbf{X}} \cdot \left(J\mathbf{F}^{-\mathbf{T}} \sqrt{c^{*2} + \left(\frac{\phi_0^w c_0^f(R)}{J - 1 + \phi_0^w} \right)^2} \right), \tag{5.7}$$

where $\mathbf{S}_e$ is the effective first Piola-Kirchhoff stress tensor, related to the effective Cauchy stress by $\boldsymbol{\sigma}_e = (1/J)\mathbf{S}_e \cdot \mathbf{F}^T$.

To close the problem, we must determine suitable boundary conditions for $f(R)$. At $R = 0$, we impose no displacement. On the outer boundary, $R = H$, we impose either no displacement (representing an intact brain) or free swelling (representing a craniectomy), *i.e.* we have,

$$f|_0 = 0, \qquad \begin{cases} f|_H = H, & \text{(intact skull)} \\ \hat{\mathbf{e}}_r \cdot \boldsymbol{\sigma}|_H \cdot \hat{\mathbf{e}}_r = 0, & \text{(craniectomy)} \end{cases} \tag{5.8}$$

where $\hat{\mathbf{e}}_r$ is a unit normal in the radial direction and

$$\boldsymbol{\sigma} = \boldsymbol{\sigma}_e - RT \left(\sqrt{c^{*2} + \left(\frac{\phi_0^w c_0^f(R)}{J - 1 + \phi_0^w} \right)^2} - c^* \right), \tag{5.9}$$

is the Cauchy stress.

Once the deformation has been determined, the stress $\boldsymbol{\sigma}(R)$ is known everywhere. We must now determine the damage. To do so, we define a critical stress, σ_{crit}, the compressive stress at which we assume capillaries are compressed and cease to function, and $\sigma_{max}(R)$, the maximum compressive stress locally within the tissue. Since we are considering a spherically symmetric geometry, $\sigma_{max}(R)$ is equal to the maximum of the radial and circumferential components of the compressive Cauchy stress,

$$\sigma_{max}(R) := \max(-(\hat{\mathbf{e}}_r \cdot \boldsymbol{\sigma} \cdot \hat{\mathbf{e}}_r), -(\hat{\mathbf{e}}_\theta \cdot \boldsymbol{\sigma} \cdot \hat{\mathbf{e}}_\theta)). \tag{5.10}$$

Note that in the definition of the Cauchy stress, $\boldsymbol{\sigma} = \boldsymbol{\sigma}_e - p\mathbf{I}$, a positive stress is tensile. Thus we take the maximum of the negative components of the stress to determine the maximum compressive stress.

5.2.3 Oxygen

We now consider the governing equation for oxygen transport. We denote the oxygen concentration by $\mathcal{C}$. At steady state, the diffusion-uptake equation for oxygen concentration within the tissue is

$$0 = D\nabla^2\mathcal{C} - R(\mathcal{C}), \tag{5.11}$$

where D is the diffusion coefficient of oxygen and $R(\mathcal{C})$ is an uptake term, which represents the oxygen used by the tissue in, for example, respiration. Uptake of oxygen in tissue is typically modelled by Michaelis-Menton term (Keener and Sneyd, 1998)

$$R(\mathcal{C}) = \frac{V_m\mathcal{C}}{\mathcal{C} + k_m}, \tag{5.12}$$

where V_m and k_m are constants representing the maximal uptake rate of oxygen, and the oxygen concentration at which the uptake rate falls to $V_m/2$, respectively.

As the system must be solved on a deformable domain, we also map the governing equation for oxygen concentration (5.11) onto the Lagrangian domain,

$$0 = D\frac{1}{J}\nabla_{\mathbf{X}} \cdot \left[J\mathbf{F}^{-T}\mathbf{F}^{-1}\left(\nabla_{\mathbf{X}}\mathcal{C}\right)\right] - R(\mathcal{C}), \tag{5.13}$$

where the relations between the Eulerian and Lagrangian description of the gradient of a scalar field and divergence of a vector field (equation (4.14) of Chapter 4) have been used.

Recall that the N capillaries are located at positions $R_{cap_i} = (i-1/2)H_{cap}$ $(i = 1 \ldots N)$ (see §5.2.1). For the oxygen model, we impose boundary conditions at $R = 0$, $R = H$,

and on each capillary $R = R_{cap_i}$. At the origin ($R = 0$) we have symmetry, and we assume no oxygen flux out of the tissue boundary ($R = H$). Thus,

$$\left.\frac{\mathrm{d}\mathcal{C}}{\mathrm{d}R}\right|_0 = 0, \qquad\qquad \left.\frac{\mathrm{d}\mathcal{C}}{\mathrm{d}R}\right|_H = 0. \tag{5.14}$$

We allow each capillary to be either open or closed, depending upon the mechanical stress within the tissue at that point. Then,

$$\begin{cases} \mathcal{C}|_{R_{cap,i}} = \mathcal{C}_{cap}, & \text{if the } i\text{th capillary is open,} \\ [\mathcal{C}]_{R_{cap,i}} = 0 = \left[\dfrac{1}{f'}\dfrac{\mathrm{d}\mathcal{C}}{\mathrm{d}R}\right]_{R_{cap,i}}, & \text{if the } i\text{th capillary is closed,} \end{cases} \tag{5.15}$$

for $i = 1 \dots N$, where $[\mathcal{C}]_R = \mathcal{C}_{R^+} - \mathcal{C}_{R^-}$ denotes the jump at position R. This means that we assume the tissue oxygen concentration $\mathcal{C}$ is equal to the capillary oxygen concentration $\mathcal{C}_{cap}$ if the capillary is open, whilst the presence of the capillary has no effect on the tissue oxygen concentration if the capillary is closed.

We define a critical oxygen concentration, $\mathcal{C}_{crit}$, below which the tissue is assumed to become ischemic and infarcted, causing exposure of intracellular FCD. This coupling between the mechanics of and oxygen concentration in the tissue is discussed in §5.2.5.

5.2.4 Non dimensionalisation

We rescale the variables $f(R)$ and $\mathcal{C}(R)$, using the radius of the tissue region H as the length scale and the concentration of oxygen in capillaries $\mathcal{C}_{cap}$ as the oxygen scale,

$$R = H\bar{R}, \qquad\qquad f = H\bar{f}, \qquad\qquad \mathcal{C} = \mathcal{C}_{cap}\bar{\mathcal{C}}. \tag{5.16}$$

Then (dropping the bars from dimensionless variables) we rewrite the oxygen governing equation (5.11) with a Michaelis-Menton uptake term (5.12) as,

$$\frac{1}{J}\nabla_{\mathbf{X}} \cdot \left[J\mathbf{F}^{-T}\mathbf{F}^{-1}\left(\nabla_{\mathbf{X}}\mathcal{C}\right)\right] = \frac{\bar{V}_m\mathcal{C}}{\mathcal{C} + \bar{k}_m}, \tag{5.17}$$

and the Euler equation (5.7) is

$$\nabla_{\mathbf{X}} \cdot \mathbf{S}_e = \nabla_{\mathbf{X}} \cdot \left(J\mathbf{F}^{-\mathbf{T}} \sqrt{\bar{c}^{*2} + \left(\frac{\phi_0^w \bar{c}_0^f}{J - 1 + \phi_0^w}\right)^2} \right), \tag{5.18}$$

where we have chosen the same pressure scaling as in Chapter 4, so that the new effective Piola-Kirchhoff stress is defined by $\bar{\mathbf{S}}_e = \mathbf{S}_e/(\lambda_s+2\mu_s)$. The other dimensionless quantities are defined as follows:

$$\bar{V}_m = \frac{H^2 V_m}{D}, \qquad \bar{k}_m = \frac{k_m}{\mathcal{C}_{cap}}, \qquad \bar{c}^* = \frac{RTc^*}{\lambda_s + 2\mu_s}, \qquad \bar{c}_0^f(R) = \frac{RTc_0^f(R)}{\lambda_s + 2\mu_s}. \tag{5.19}$$

The dimensionless critical stress threshold and critical oxygen threshold are defined as

$$\bar{\sigma}_{crit} = \frac{\sigma_{crit}}{\lambda_s + 2\mu_s}, \qquad \bar{\mathcal{C}}_{crit} = \frac{\mathcal{C}_{crit}}{\mathcal{C}_{cap}}. \tag{5.20}$$

The dimensionless boundary conditions are given in §5.2.5.

5.2.5 Iterative approach for propagation

Initially, we prescribe some radius of damage, $R_{(1)}$, representing the region of tissue within which blood flow is restricted following an initial injury, *e.g.* a stroke. We are interested to find how far the damage can propagate without any externally imposed damage.

We close the capillaries in the region $R < R_{(1)}$, and find the location of ischemic tissue, by solving for the oxygen distribution (§5.2.3) within the tissue. The ischemic tissue is defined to be the region with oxygen levels below the critical oxygen threshold $\bar{\mathcal{C}}_{crit}$. In this ischemic tissue, we impose an FCD (since the cells in this region are assumed to have died, and have exposed their intracellular FCD). We then solve for the deformation of the tissue with this FCD distribution (§5.2.2).

If there is some radius $R_{(2)} > R_{(1)}$, such that the maximum compressive stress σ_{max} exceeds the critical threshold $\bar{\sigma}_{crit}$ for all $R < R_{(2)}$, we define $R_{(2)}$ as the new damage radius (otherwise, we set $R_{(2)} = R_{(1)}$, meaning that damage does not propagate). For the next iteration we close capillaries within $R < R_{(2)}$, and follow the same procedure.

We define $R_{(n+1)}$ as the radius of damage after n iterations, and $R_{(\infty)}$ as the radius of damage when propagation is halted. Each iteration represents the time taken for ischemic tissue to die and expose its intracellular FCD. We call this iterative procedure the 'coupled oxygen-mechanics damage model'; we now outline this process in a schematic (Figure 5.2), and present the governing equations at the nth iteration.

Schematic of the iteration process

Step 0 Initially healthy tissue

All tissue has sufficient oxygen (so that $\mathcal{C} > \bar{\mathcal{C}}_{crit}$ everywhere)

No FCD present. The tissue is in a stress free reference state.

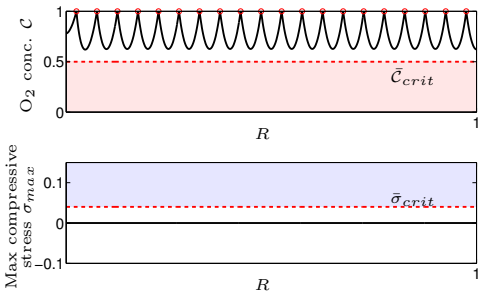

Step 1 Choose some initial radius of damage $R_{(1)}$

a) Close all capillaries within $R \leq R_{(1)}$ and compute new steady oxygen profile

b) Impose FCD wherever the oxygen concentration $\mathcal{C}$ falls below the critical value $\bar{\mathcal{C}}_{crit}$ (hatched region), and compute associated stress profile

c) Define $R_{(2)}$ as the radius at which $\sigma_{max} = \bar{\sigma}_{crit}$. This is the new 'damage radius', representing the radius within which the capillaries are compressed beyond the critical level at which blood flow ceases.

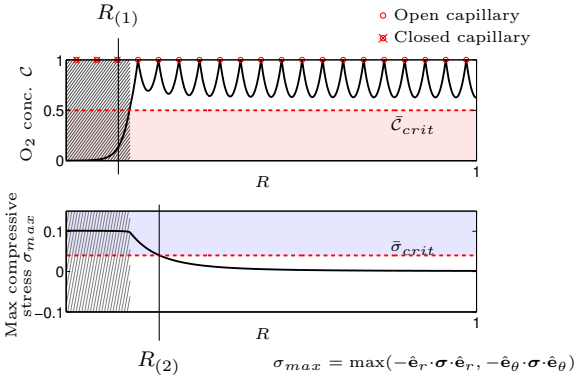

⋮

Step n

a) Close all capillaries within the new damage radius $R \leq R_{(n)}$ and compute the new oxygen profile

b) Impose FCD wherever the oxygen concentration falls below the critical value $\mathcal{C} < \bar{\mathcal{C}}_{crit}$ (hatched region), and compute new stress profile

c) Define $R_{(n+1)}$ as the radius at which $\sigma_{max} = \bar{\sigma}_{crit}$.

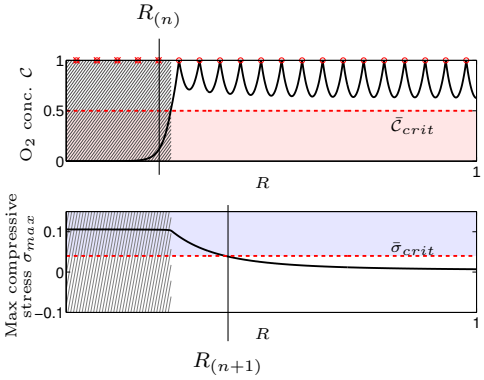

Figure 5.2: Schematic showing the iteration stages of the coupled oxygen-mechanics damage model

Governing equations for the coupled oxygen-mechanics damage model

At step $n = 1$, we choose $R_{(1)}$ to be the initial radius of damage, and set $f_{(0)}(R) \equiv R$ everywhere (to represent that the tissue is not deformed initially).

Step a): Find the oxygen distribution $\mathcal{C}_{(n)}(R)$

We find the oxygen concentration profile at step n, $\mathcal{C}_{(n)}(R)$, by solving the steady diffusion-uptake equation for oxygen concentration (5.13). This equation can be rewritten, assuming spherical symmetry, as

$$\frac{\mathrm{d}^2\mathcal{C}_{(n)}}{\mathrm{d}R^2} + \left(\frac{2f'_{(n-1)}}{f_{(n-1)}} - \frac{f''_{(n-1)}}{f'_{(n-1)}}\right)\frac{\mathrm{d}\mathcal{C}_{(n)}}{\mathrm{d}R} = f'^2_{(n-1)}\frac{\bar{V}_m\mathcal{C}_{(n)}}{\mathcal{C}_{(n)} + \bar{k}_m}, \tag{5.21}$$

along with boundary conditions,

$$\left.\frac{\mathrm{d}\mathcal{C}_{(n)}}{\mathrm{d}R}\right|_0 = 0, \quad \left.\frac{\mathrm{d}\mathcal{C}_{(n)}}{\mathrm{d}R}\right|_1 = 0, \quad \begin{cases} \mathcal{C}_{(n)}\big|_{R_{cap,i}} = 1, & \text{if } R_{cap,i} > R_{(n)}, \\ \left[\mathcal{C}_{(n)}\right]_{R_{cap,i}} = 0 = \left[\dfrac{1}{f'_{n-1}}\dfrac{\mathrm{d}\mathcal{C}_{(n)}}{\mathrm{d}R}\right]_{R_{cap,i}}, & \text{if } R_{cap,i} \le R_{(n)}, \end{cases} \tag{5.22}$$

where $R_{cap,i}$ is the position of the ith capillary (§5.2.1). The last boundary condition in (5.22) is a mathematical representation of the assumption that if the capillaries are closed (*i.e.* if they are located within the damaged region $0 < R < R_{(n)}$) then they do not alter the flux or concentration of oxygen through them. However, if the capillaries are open ($R_{(n)} < R < 1$) then they fix the concentration at that point to be 1. Note that the oxygen profile is solved on the deformed domain computed in the previous iteration (and hence $f_{(n-1)}$ appears in these governing equations).

Equation (5.21), along with boundary conditions (5.22), are solved using a multipoint boundary value solver, '*bvp5c*', in Matlab.

Step b): Find the tissue deformation $f_{(n)}(R)$

We impose an FCD $c^f_{0\,(n)}(R)$ wherever the oxygen concentration $\mathcal{C}_{(n)}$ falls below the critical value $\bar{\mathcal{C}}_{crit}$,

$$c^f_{0\,(n)}(R) = \begin{cases} \bar{c}^f_{0\,I}, & \text{where } \mathcal{C}_{(n)}(R) \le \bar{\mathcal{C}}_{crit}, \\ 0, & \text{where } \mathcal{C}_{(n)}(R) > \bar{\mathcal{C}}_{crit}, \end{cases} \tag{5.23}$$

where $\bar{c}^f_{0\,I}$ is a constant parameter representing the FCD of infarcted tissue.

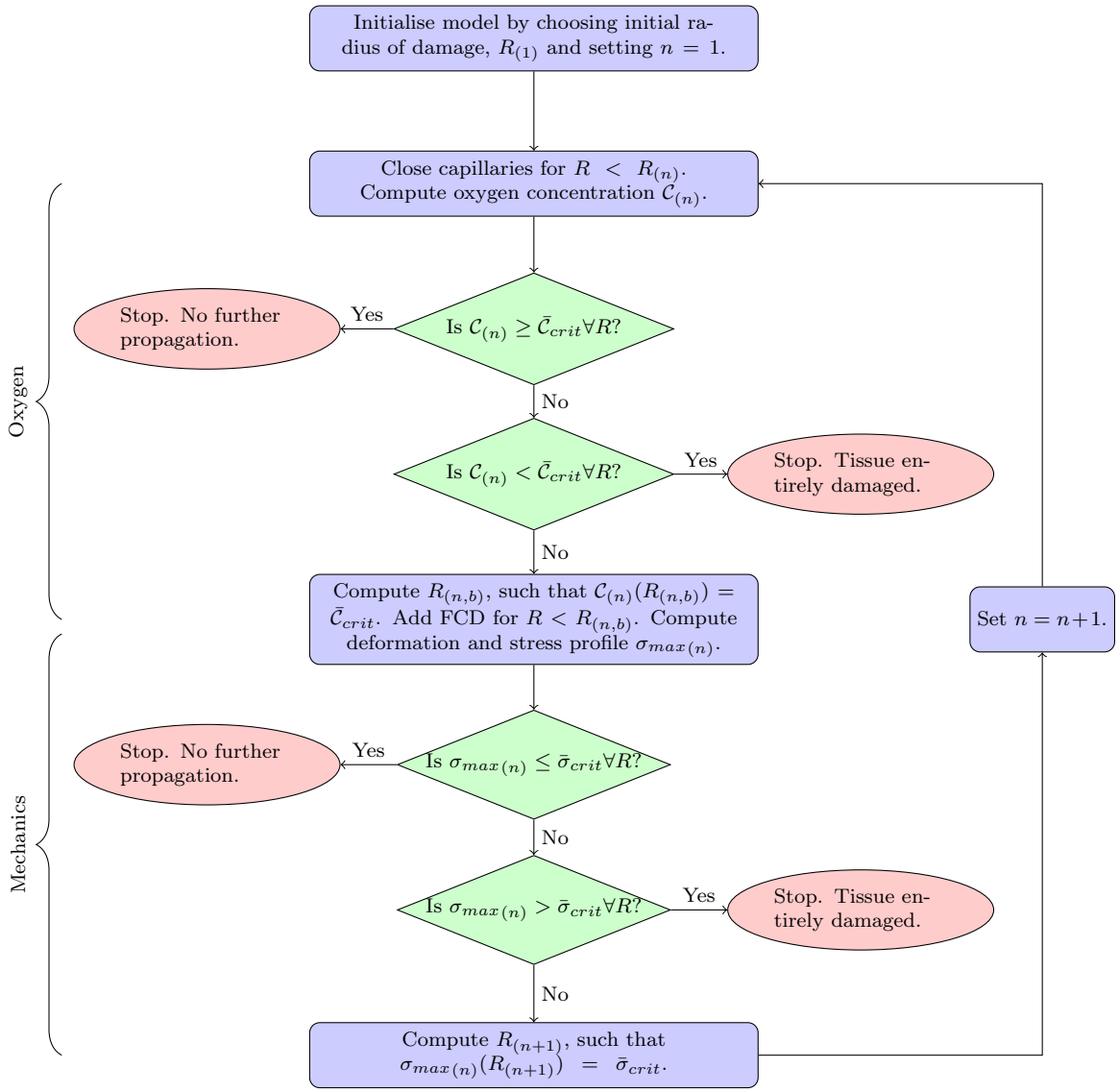

Figure 5.3: A flow chart to show the stages of the coupled oxygen-mechanics damage model. The governing equations are given in §5.2.5.

If $\mathcal{C}_{(n)} > \bar{\mathcal{C}}_{crit}$ everywhere then the tissue receives sufficient oxygen everywhere. Then there is no propagation (and hence we cease the iterations). If $\mathcal{C}_{(n)} < \bar{\mathcal{C}}_{crit}$ everywhere then the entire tissue is ischemic and we set the radius of ischemic tissue, $R_{b(n)} = 1$. Otherwise, let us define $R_{b(n)}$ as the value of R such that $\mathcal{C}_{(n)} = \bar{\mathcal{C}}_{crit}$ [2].

Then, since the FCD is constant within each of the regions $0 < R < R_{b(n)}$ and $R_{b(n)} < R < 1$, the governing equation (5.18) can be solved with a constant FCD in each region. Boundary conditions must be applied at the interface between the damaged and healthy regions at $R = R_{b(n)}$ (equation (5.29)). In a spherically symmetric geometry the radial component of the governing equation $\nabla_{\mathbf{X}} \cdot \mathbf{S}_{(n)} = \mathbf{0}$ may be written as

$$\frac{-f_{(n)}^2 c^{f\,2}}{R^2(J_{(n)} - \phi_0^s)\sqrt{c^{*2} + c^{f\,2}}} \left[\frac{f_{(n)}^2 f''_{(n)}}{R^2} + \frac{2 f_{(n)} f'^2_{(n)}}{R^2} - \frac{2 f_{(n)}^2 f'_{(n)}}{R^3} \right] = \frac{\mathrm{d}(S_{RR(n)})}{\mathrm{d}R} + \frac{2(S_{RR(n)} - S_{\Theta\Theta(n)})}{R}, \tag{5.24}$$

where c^f is given by (5.5), $J_{(n)} = f_{(n)}^2 f'_{(n)}/R$, and $S_{RR(n)}$ and $S_{\Theta\Theta(n)}$ are the diagonal components of the effective Piola-Kirchhoff stress $\mathbf{S}_{e(n)}$. Note that in the outer region ($R_{b(n)} < R < 1$), the FCD $c^f \equiv 0$ and thus the LHS of equation (5.24) is zero.

In §2.3 we showed that, for physiological parameters related to the brain, the Fung, Ogden and neo-Hookean strain energy functions exhibit similar stress-strain behaviour up to ≈50% volume increase (see Figure 2.3). Thus we use a neo-Hookean stress tensor in this Chapter, such that,

$$S_{RR(n)} = \frac{1}{f'_{(n)}} \left[\bar{\mu}_s (f'^2_{(n)} - 1) + \bar{\lambda}_s J_{(n)} (J_{(n)} - 1) \right], \tag{5.25}$$

$$S_{\Theta\Theta(n)} = \frac{R}{f_{(n)}} \left[\bar{\mu}_s \left(\frac{f_{(n)}^2}{R^2} - 1 \right) + \bar{\lambda}_s J_{(n)} (J_{(n)} - 1) \right]. \tag{5.26}$$

The Cauchy stress $\boldsymbol{\sigma}_{(n)}$ is defined as

$$\boldsymbol{\sigma}_{(n)} = \boldsymbol{\sigma}_{e(n)} - \left[\sqrt{\bar{c}^{*2} + \left(\frac{\phi_0^w c_{0\,(n)}^f(R)}{J_{(n)} - 1 + \phi_0^w} \right)^2} - \bar{c}^* \right], \tag{5.27}$$

where the effective Cauchy stress $\boldsymbol{\sigma}_{e(n)}$ is related to the effective Piola-Kirchhoff stress $\boldsymbol{\sigma}_e = (1/J)\mathbf{S}_e \cdot \mathbf{F}^T$. Note from equation (5.27) that in the absence of FCD ($c_0^f = 0$), the Cauchy and effective Cauchy stresses are equal.

[2] In practice, there is only one such value (see Figure 5.4).

The boundary conditions for $f_{(n)}$ consist of no displacement at the origin,

$$f_{(n)}\big|_0 = 0, \tag{5.28}$$

along with continuity of displacement and radial stress at the interface between the damaged and non-damaged region $R = R_{b(n)}$,

$$\left[f_{(n)}\right]_{R_{b(n)}} = 0, \qquad \left[\hat{\mathbf{e}}_r \cdot \boldsymbol{\sigma}_{(n)} \cdot \hat{\mathbf{e}}_r\right]_{R_{b(n)}} = 0. \tag{5.29}$$

Note that if $R_{b(n)} = 1$ (*i.e.* the entire tissue has insufficient oxygen, so that $c_0^f(R) = \bar{c}_{0I}^f$ everywhere), then this boundary condition (5.29) is unnecessary. At the outer boundary $R = 1$ we impose either no displacement or no stress,

$$f_{(n)}\big|_1 = 1, \qquad \text{or} \qquad \hat{\mathbf{e}}_r \cdot \boldsymbol{\sigma}_{(n)} \cdot \hat{\mathbf{e}}_r\big|_1 = 0. \tag{5.30}$$

The governing equation (5.24), along with boundary conditions (5.28)-(5.30), is solved using a multipoint boundary value solver, '*bvp5c*', in Matlab.

Step c): Find the new damage radius, $R_{(n+1)}$

We now consider the maximum compressive stress $\sigma_{max(n)}(R) := \max(-(\hat{\mathbf{e}}_r \cdot \boldsymbol{\sigma}_{(n)} \cdot \hat{\mathbf{e}}_r), -(\hat{\mathbf{e}}_\theta \cdot \boldsymbol{\sigma}_{(n)} \cdot \hat{\mathbf{e}}_\theta))$. We shall show in §5.4 that $\sigma_{max(n)}(R)$ is a monotonic decreasing function over $R_{(n)} < R < 1$; thus there are three possible cases:
i) $\sigma_{max(n)} < \bar{\sigma}_{crit}$ for all $R_{(n)} < R < 1$: the damage does not propagate further, and $R_{(n+1)} = R_{(n)}$.
ii) $\sigma_{max(n)} = \bar{\sigma}_{crit}$ for some $R_{(n)} < R < 1$: we define $R_{(n+1)}$ such that $\sigma_{max(n)}\big|_{R_{(n+1)}} = \bar{\sigma}_{crit}$.
iii) $\sigma_{max(n)} > \bar{\sigma}_{crit}$ for all $R_{(n)} < R < 1$: the entire tissue is damaged; we set $R_{(n+1)} = 1$.
We repeat steps (a) to (c) for step $n+1$ and iterate. A summary of this process is shown in Figure 5.3.

5.3 Critical oxygen concentration thresholds

In this section, we focus on the coupling between oxygen and mechanics. Subsequently in §5.4 we shall focus on the mechanics.

5.3.1 Parameter values

Values of relevant parameters are shown in Table 5.1. We emphasise that the intercapillary distance H_{cap} is fixed physiologically, and the only spatial parameter that we vary is

H, the radius of the tissue region.

Table 5.1: Parameter values

Parameter	Description	Value	Reference	Dimensionless	Value
H	Radius of tissue region	‡		n/a	
Mechanics					
λ_s , μ_s	Elastic parameters	216, 505 Pa	Cheng and Bilston (2007)	$\bar{\lambda_s} = \lambda_s/(\lambda_s + 2\mu_s)$,	0.3
				$\bar{\mu_s} = \mu_s/(\lambda_s + 2\mu_s)$	0.78
c^*	Bathing ionic solutions	300mOsm	Elkin *et al.* (2010)	$\bar{c^*} = RTc^*/(\lambda_s + 2\mu_s)$	750
c_0^f	Damaged tissue FCD (ref. state)	11.6mOsm	Lang *et al.* (2014)	$\bar{c_0^f} = RTc_0^f/(\lambda_s + 2\mu_s)$	40
ϕ_0^w	Ref state tissue water	0.8	Hrabětová *et al.* (2002)	ϕ_0^w	0.8
σ_{crit}	Critical compressive stress	◇		$\bar{\sigma}_{crit} = \sigma_{crit}/(\lambda_s + 2\mu_s)$	*
Oxygen					
H_{cap}	Inter-capillary spacing	40μm	Pardridge (1997)	$\bar{H}_{cap} = H_{cap}/H$	‡
D	Diffusion coefficient of O_2	1.5×10^{-9}m^2/s	Homer *et al.* (1983.) Ganfield *et al.* (1970)	n/a	
$\mathcal{C}_{cap}$	Capillary O_2 concentration	0.05-0.1mM	†	n/a	
$\mathcal{C}_{crit}$	Critical O_2 concentration	0.02mM	††	$\bar{\mathcal{C}}_{crit} = \mathcal{C}_{crit}/\mathcal{C}_{cap}$	0.2-0.4
V_m	Maximal rate of O_2 uptake	0.1mM/s	Secomb *et al.* (2000)	$\bar{V}_m = H^2V_m/D/\mathcal{C}_{cap}$	‡
k_m	Michaelis constant for O_2 uptake	5×10^{-3}mM	Secomb *et al.* (2000)	$\bar{k_m} = k_m/\mathcal{C}_{cap}$	0.01

◇ This parameter is unknown.

† In the brain, the oxygen concentration of arterial blood (entering the brain) is 80-100mmHg, and the oxygen concentration of ventricular blood (leaving the brain) is 30-40mmHg (Secomb *et al.*, 2000; Erecińska and Silver, 2001). Therefore we assume that the capillary oxygen concentration falls between these values.

†† The critical value of oxygen tension in the brain is threshold below which we assume that tissue has insufficient oxygen and dies. Patients will be given treatment if their brain oxygen level falls below 20mmHg (Narotam *et al.*, 2009), and a mean oxygen tension in brain tissue of 19mmHg has been associated with poor outcome (Dhawan and DeGeorgia, 2012). Therefore we take $\mathcal{C}_{\text{crit}}$ =20mmHg.

‡ We shall consider several values of tissue radius, H, in our results. See figure captions for values.

5.3.2 Capillary closure and ischemia

In Figure 5.4 we show oxygen concentration profiles through healthy tissue, for stages 0 (healthy tissue) and 1 (some capillaries closed) of the iteration process explained in §5.2.5. We have chosen a small region of tissue (with radius equal to just 5 times the inter-capillary distance, $H = 5H_{cap}$) to ensure that the local oxygen distribution can be seen clearly. The grey region shows the range of physiological values for $\bar{\mathcal{C}}_{crit}$, as determined from a literature review (see Table 5.1).

We observe that for the parameters we consider: (a) when all capillaries are open the tissue has sufficient oxygen everywhere. If a single capillary is closed (case (b)), so that $0 < R_{(1)} < H_{cap}$, a region of tissue around the capillary will become ischemic provided the oxygen concentration $\mathcal{C}$ falls below the critical value $\bar{\mathcal{C}}_{crit}$ in some inner region. This will occur provided that $\bar{\mathcal{C}}_{crit} \gtrsim 0.25$ (see dashed line in Figure 5.4(b)). However, if at least 2 capillaries are closed (case (c)) then the oxygen concentration will always fall below $\bar{\mathcal{C}}_{crit}$ in an inner region.

Whilst these observations are true for the particular parameters considered (Table 5.1), the general trend will be the same for other physiological parameter values. This is

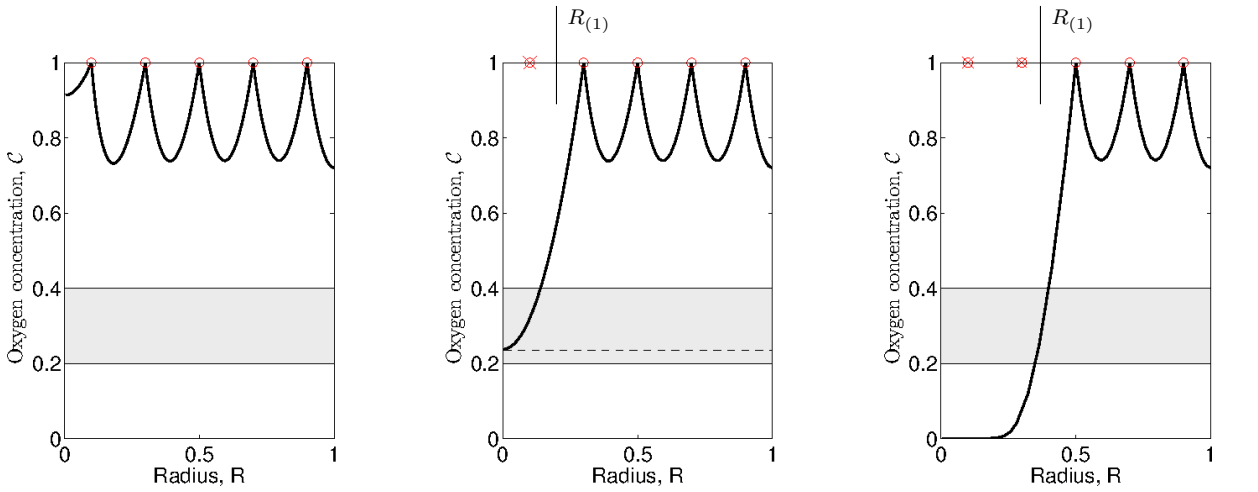

a) Healthy tissue b) One capillary blocked c) Two capillaries blocked

Figure 5.4: Results for oxygen concentration $\mathcal{C}$, at steps 0 (healthy tissue) and 1 (capillaries located within $R < R_{(1)}$ closed) of the procedure described in Section 5.2.5. The initial damage radius $R_{(1)}$ is chosen so that 1 capillary is closed in (b), and two capillaries are closed in (c). The grey region indicates the physiological range of the critical oxygen concentration, $\bar{\mathcal{C}}_{crit}$. Red circles show the position of open capillaries, crossed red circles the position of closed capillaries. Parameters: $H = 5H_{cap}$, see Table 5.1 for all other parameter values.

because brain cells have a high oxygen requirement, and therefore oxygen cannot travel more than a few inter-capillary distances through the brain (Secomb *et al.*, 2000).

Thus, Figure 5.4 indicates that, provided an initial stroke blocks blood supply to a region of tissue with radius greater than $\approx 2\times$ inter-capillary distance, then this initial capillary closure will always lead to the tissue becoming locally ischemic.

5.3.3 Relevance to the tissue length scale

In Figure 5.4, we showed that the oxygen concentration profile in a very small tissue region (with radius 5 $\times$ the inter-capillary distance, H_{cap}). In reality, we are more concerned with propagation on the length scale of a brain (cm's).

We observe from Figure 5.4 that when a capillary is closed, whilst the oxygen concentration $\mathcal{C}$ will be above $\bar{\mathcal{C}}_{crit}$ for some distance away from the closed capillary, this distance is on the scale of the inter-capillary spacing $\bar{H}_{cap}$. Therefore the precise value of the critical oxygen concentration $\bar{\mathcal{C}}_{crit}$ will only change the location of the infarcted tissue (and hence the location in which we impose an FCD), over a distance of the order of the inter-capillary distance. As a result, we conclude that the details of the oxygen diffusion and uptake are relatively unimportant over the tissue length scale. This leads us to compare two models: the coupled oxygen-mechanics damage model described in

§5.2.5, (which accounts for the oxygen transport) and a 'simplified mechanics-only damage model' which does not explicitly include the details of oxygen transport. We describe the mechanics-only damage model now.

The mechanics-only damage model

In the mechanics-only damage model, we do not model the tissue oxygen concentration, and hence do not consider the closure of capillaries. Instead, we assume that any tissue experiencing a critical stress above $\bar{\sigma}_{crit}$ at stage n becomes ischemic (and hence exposes intracellular FCD) at stage $n+1$. Initially, we impose some initial radius of damage, $R_{(1)}$, and in subsequent steps, we take the value of $R_{(n)}$ from the previous step. At step n, we impose an FCD,

$$c^f_{0\,(n)}(R) = \begin{cases} \bar{c^f_{0\,I}}, & R < R_{(n)}, \\ 0, & R \geq R_{(n)}, \end{cases} \tag{5.31}$$

and solve equation (5.24) in each of the region $0 < R < R_{(n)}$ and $R_{(n)} < R < 1$, along with the boundary conditions (5.28) at $R = 0$, (5.30) at $R = 1$, and at $R_{(n)}$:

$$\left[f_{(n)}\right]_{R_{(n)}} = 0, \qquad \left[\hat{\mathbf{e}}_r \cdot \boldsymbol{\sigma}_{(n)} \cdot \hat{\mathbf{e}}_r\right]_{R_{(n)}} = 0, \tag{5.32}$$

where the Cauchy stress $\boldsymbol{\sigma}_{(n)}$ is given by (5.27). We then define the maximum compressive stress as $\sigma_{max\,(n)}(R) := \max(-(\hat{\mathbf{e}}_r \cdot \boldsymbol{\sigma}_{(n)} \cdot \hat{\mathbf{e}}_r), -(\hat{\mathbf{e}}_\theta \cdot \boldsymbol{\sigma}_{(n)} \cdot \hat{\mathbf{e}}_\theta))$, and find $R_{(n+1)}$ such that $\sigma_{max\,(n)}\big|_{R_{(n+1)}} = \bar{\sigma}_{crit}$ as described in step (c) of the coupled oxygen-mechanics damage model (§5.2.5). This procedure is explained in Figure 5.5, and a flow chart of the stages shown in Figure 5.6.

Step 0 Initially healthy tissue
No FCD present. The tissue is in a stress free reference state.

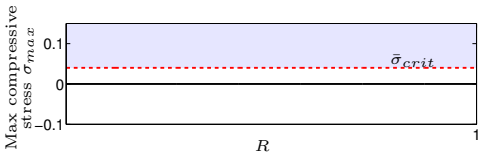

Step 1 Choose some initial radius of damage $R_{(1)}$

a) Impose FCD within $R \leq R_{(1)}$ (hatched region), and compute new stress profile

b) Define $R_{(2)}$ as the radius at which $\sigma_{max_1} = \bar{\sigma}_{crit}$. This is the new 'damage radius', representing the radius within which the tissue is infarcted.

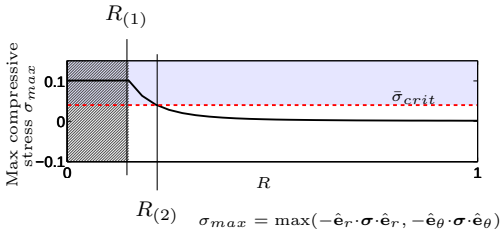

;

Step n

a) Impose FCD within the new damage radius $R \leq R_{(n)}$, and compute new stress profile

b) Define $R_{(n+1)}$ as the radius at which $\sigma_{max(n)} = \bar{\sigma}_{crit}$.

c) Repeat this step until either $R_{(n+1)} = R_{(n)}$ (damage propagation is halted) or $R_{(n+1)} = 1$ (the entire tissue is damaged).

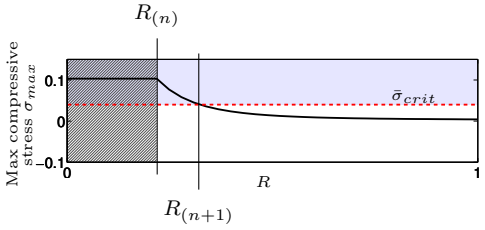

Figure 5.5: Schematic showing the iteration stages of the simplified mechanics-only damage model

Comparison of mechanics-only and coupled oxygen-mechanics damage models

In Figure 5.7, we compare results of the coupled oxygen-mechanics damage model and mechanics-only damage model, with no-displacement outer boundary conditions (equation 5.8). We consider domains of radius 10 and 30 times the inter-capillary distance H_{cap}. The results show the value of $R_{(n+1)}$, as a function of $R_{(n)}$, for each of the two models. We observe that the models display a similar trend of results. The major difference is that the results of the oxygen-mechanics model change in discrete steps (corresponding to the closure of individual capillaries), whilst the mechanics-only damage model yields a smooth curve (since FCD is being exposed continuously as the deformation increases, and not in response to capillary closure).

The agreement between the models improves as further capillaries are added. This is because inclusion of the oxygen model increases resolution on the order of the dimensionless inter-capillary spacing $\bar{H}_{cap} = H_{cap}/H$, which becomes smaller as the domain length H increases. This indicates that on domains of the size we are interested ($H \approx 1$cm), inclusion of the oxygen model will not affect the results.

Thus, from herein, we consider the mechanics-only damage model for simplicity.

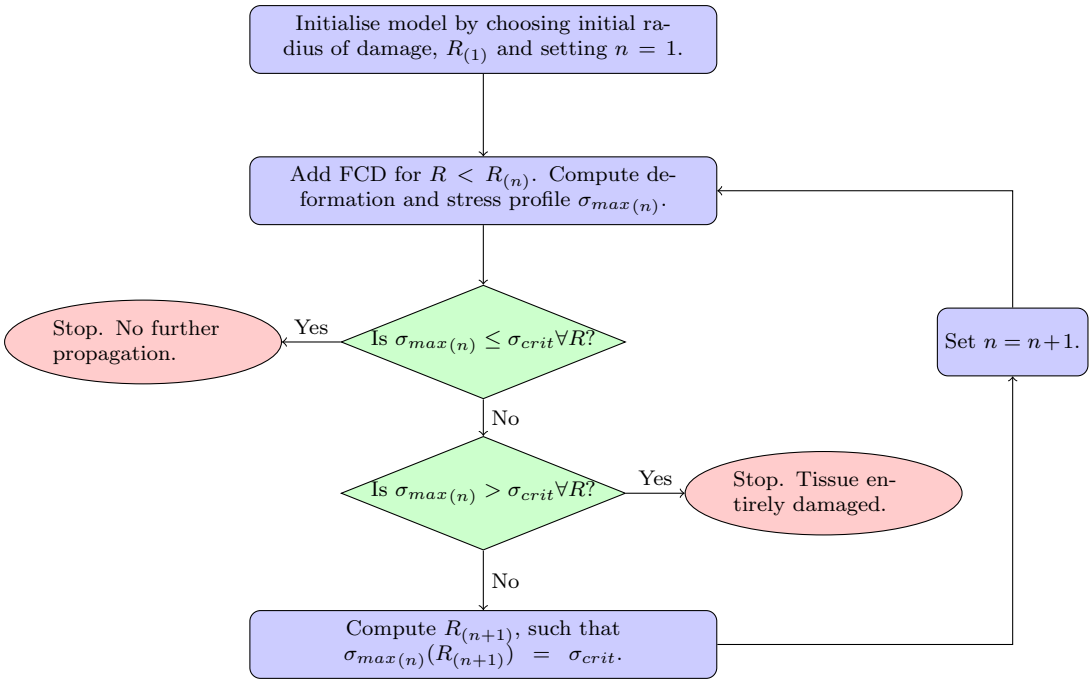

Figure 5.6: A flow chart to show the stages of the mechanics-only damage model.

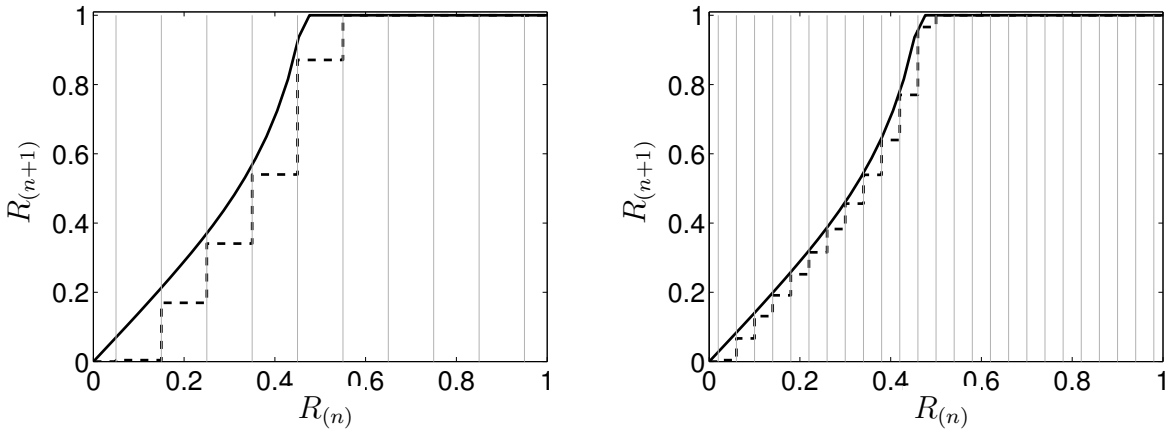

(a) 10 capillaries (H=0.4mm)

(b) 30 capillaries (H=1.2mm)

Figure 5.7: A comparison of the new damage radius $R_{(n+1)}$ as a function of the previous damage radius $R_{(n)}$, computed using the coupled oxygen-mechanics damage model (dashed curves) and the reduced mechanics-only damage model (solid curves), for no-displacement outer boundary conditions. Results are shown for two different domain lengths H. The grey lines show the positions of capillaries. The coupled oxygen-mechanics damage model exhibits discrete steps, because the oxygen concentration profile remains unchanged until an additional capillary is closed. Parameters: H as given in each caption, $\bar{C}_{crit} = 0.2$, see Table 5.1 for all other parameter values.

5.4 Critical stress thresholds

We now investigate the conditions under which damage propagates using the mechanics-only damage model. In particular, we are interested in understanding how the critical stress at which we assume the vessels become compressed, $\bar{\sigma}_{crit}$, and the choice of boundary conditions applied at the outer surface, affect propagation.

Here, we use a numerical approach to investigate results in finite elasticity. Subsequently, in §5.5 we consider an infinitesimal deformation model, which allows us to find an algebraic expression relating $R_{(n+1)}$ to $R_{(n)}$.

5.4.1 Free swelling versus no displacement boundary conditions

We consider two different boundary conditions on the outer surface: no displacement, to represent an intact skull, and no stress, to represent craniectomy (see equation (5.8)).

In Figure 5.8, we show profiles of the compressive stress and stretch in the radial and circumferential directions, for both of these boundary conditions. We observe that in both cases the compressive stress is greatest in the central infarcted region ($0 < R < R_{(1)}$), and is equal for both radial and circumferential components in this region. The radial compressive stress decreases with radius in the healthy tissue ($R_{(1)} < R < 1$), and is always positive (showing that the tissue is compressed radially). The circumferential compressive stress is negative in the healthy tissue ($R_{(1)} < R < 1$), meaning that the tissue is in circumferential tension. These observations correspond to the stretch profiles, which show that the tissue is always stretched in the circumferential direction, but is radially stretched in the central infarcted region and radially compressed in the surrounding region.

When a smaller region is damaged ($R_{(1)} = 0.2$), the stress and strain profiles are similar regardless of the boundary conditions. This is because the healthy region is sufficiently large that the stress decays through the healthy tissue and there is little deformation of the tissue at the outer boundary. Thus in this case the boundary conditions on the outer surface have little effect on the behaviour of the tissue. However, if a larger region is damaged (for example, $R_{(1)} = 0.6$), the radial stress within the healthy region is higher under no-displacement boundary conditions than no-stress: the confinement caused by the boundary is then felt by the tissue.

5.4.2 Criteria for propagation

We now consider the criteria which allow damage to propagate through the tissue. We observe from Figure 5.8 a general trend, namely that the radial component of compressive

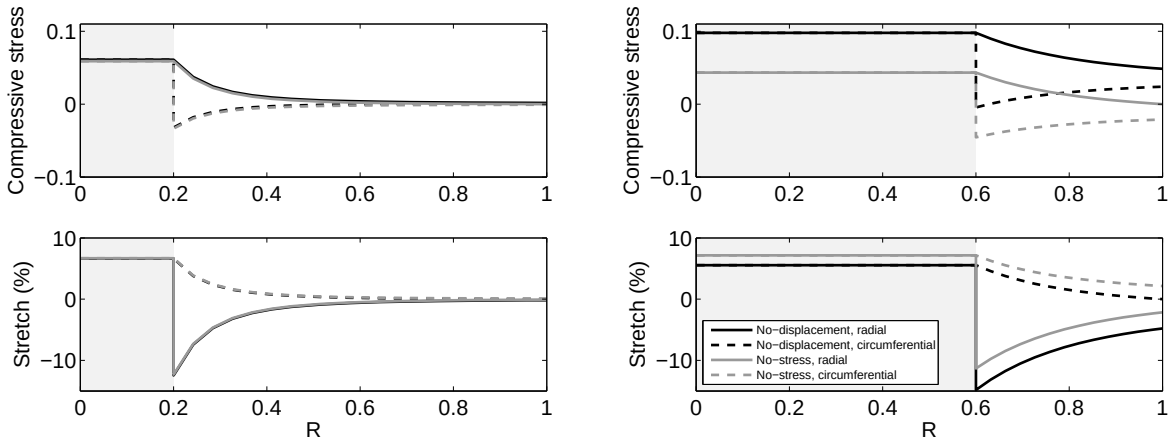

(a) Initial damage radius $R_{(1)} = 0.2$ (b) Initial damage radius $R_{(1)} = 0.6$

Figure 5.8: Figures showing how a particular FCD distribution (grey shaded region) affects the compressive stress (upper) and stretch (lower) distributions within a spherically symmetric region of tissue. Solid and dashed curves represent radial and circumferential values respectively: radial stretch is given by $(f' - 1)$ whilst circumferential stretch is given by $(f/R - 1)$. The black curves show no-displacement boundary conditions, whilst the grey curves show no-stress boundary conditions. Parameters: $H = 1$cm, all other parameters in Table 5.1.

stress is always greater than or equal to the circumferential component. Furthermore, we observe that the radial compressive stress is constant within the infarcted region ($R < R_{(1)}$), continuous, and monotonically decreasing within the healthy region ($R > R_{(1)}$). Therefore, at any given iteration, damage will propagate into the healthy tissue if the maximum radial compressive stress is greater than the critical stress ($\max(-\mathbf{e}_r \cdot \boldsymbol{\sigma} \cdot \mathbf{e}_r) > \bar{\sigma}_{crit}$), and will not propagate if the maximum radial compressive stress is less than or equal to the critical stress ($\max(-\mathbf{e}_r \cdot \boldsymbol{\sigma} \cdot \mathbf{e}_r) \leq \bar{\sigma}_{crit}$).

In Figure 5.9 we show a regime diagram of the critical stress $\bar{\sigma}_{crit}$ against the initial radius of damage $R_{(1)}$, and illustrate where in the phase space damage will propagate. The curve separating the regions is $\max(-\mathbf{e}_r \cdot \boldsymbol{\sigma} \cdot \mathbf{e}_r) = \bar{\sigma}_{crit}$. The arrows illustrate that for a particular critical stress, damage will propagate outwards until it reaches the damage radius for which $\max(-\mathbf{e}_r \cdot \boldsymbol{\sigma} \cdot \mathbf{e}_r) = \bar{\sigma}_{crit}$, or until the entire tissue is damaged. The points (a), (b) and (c) are chosen to highlight the difference between these two types of boundary condition. At (a), damage propagates for both conditions. However, the damage propagates to the boundary of the tissue under no-displacement conditions, whilst it is halted under no-stress conditions. At (b), damage propagates only under no-displacement conditions. At (c), the critical stress $\bar{\sigma}_{crit}$ is sufficiently high that damage does not propagate for either case.

In Figure 5.10, we show the evolution of the compressive radial stress profiles through

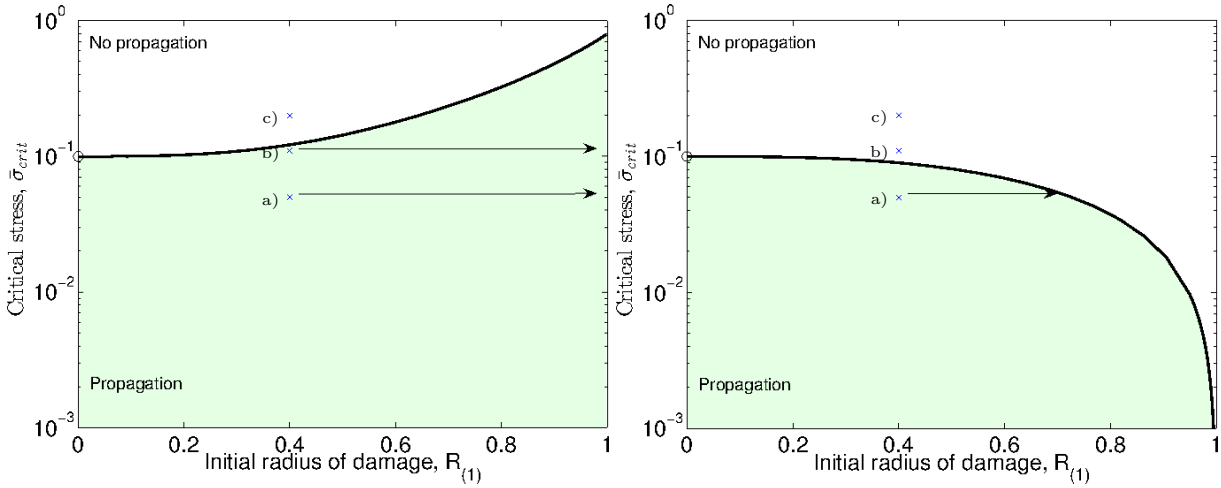

(a) No-displacement boundary condition (b) No-stress boundary condition

Figure 5.9: Regime diagram showing the regions in the parameter space of initial radius of damage $R_{(1)}$ and critical compressive stress threshold $\bar{\sigma}_{crit}$ for which damage will propagate. Damage will propagate whenever parameters are chosen to be in the green region. The black line dividing the regions is $\max(-\mathbf{e}_r \cdot \boldsymbol{\sigma} \cdot \mathbf{e}_r) = \bar{\sigma}_{crit}$. Parameters: $H = 1$cm, all other parameters in Table 5.1. Points (a), (b) and (c) are chosen to highlight the behaviour of the system (see text), and correspond to $R_{(1)} = 0.4$, $\bar{\sigma}_{crit} = 0.05, 0.12, 0.2$ respectively. The open circles at $R = 0$ are used to clarify that the limit $R_{(1)} \to 0$ is singular in the sense that an arbitrarily small amount of FCD will lead to a finite stress.

the tissue. The parameters $R_{(1)}$ and $\bar{\sigma}_{crit}$ are chosen to correspond with (a), (b) and (c), marked by blue crosses in Figure 5.9. We observe that our predictions based upon this regime diagram (Figure 5.9) are correct. When $\bar{\sigma}_{crit} = 0.05$ (Figure 5.10a), for $R_{(1)} = 0.4$, the initial maximum compressive stress is greater than the critical stress threshold $\bar{\sigma}_{crit}$ and thus propagation occurs for both boundary conditions. For no-stress boundary conditions, propagation halts once the radius of damage is approximately 0.7, whilst for no-displacement the entire tissue is finally damaged. When $\bar{\sigma}_{crit} = 0.12$ (Figure 5.10b), no propagation occurs for the no-stress boundary conditions, whilst propagation does occur for the no-displacement case. Finally, when $\bar{\sigma}_{crit} = 0.2$ (Figure 5.10c), for $R_{(1)} = 0.4$ the maximum compressive stress is below the critical stress threshold $\bar{\sigma}_{crit}$ for both sets of boundary conditions, and thus no propagation occurs in either case.

Figure 5.11 shows $R_{(2)}$ and $R_{(\infty)}$ as functions of the initial damage radius $R_{(1)}$, for the three values of critical stress ($\bar{\sigma}_{crit} = 0.05, 0.12, 0.2$) investigated in Figure 5.10. For no-displacement boundary conditions, comparing the upper and lower plots we observe that if propagation is initiated, then damage will propagate through the entire tissue. At each critical stress $\bar{\sigma}_{crit}$ there is some critical initial radius ${R_{(1)}}_{crit}$ such that damage is initiated (and hence propagates through the whole tissue) when as $R_{(1)} > {R_{(1)}}_{crit}$. However, for

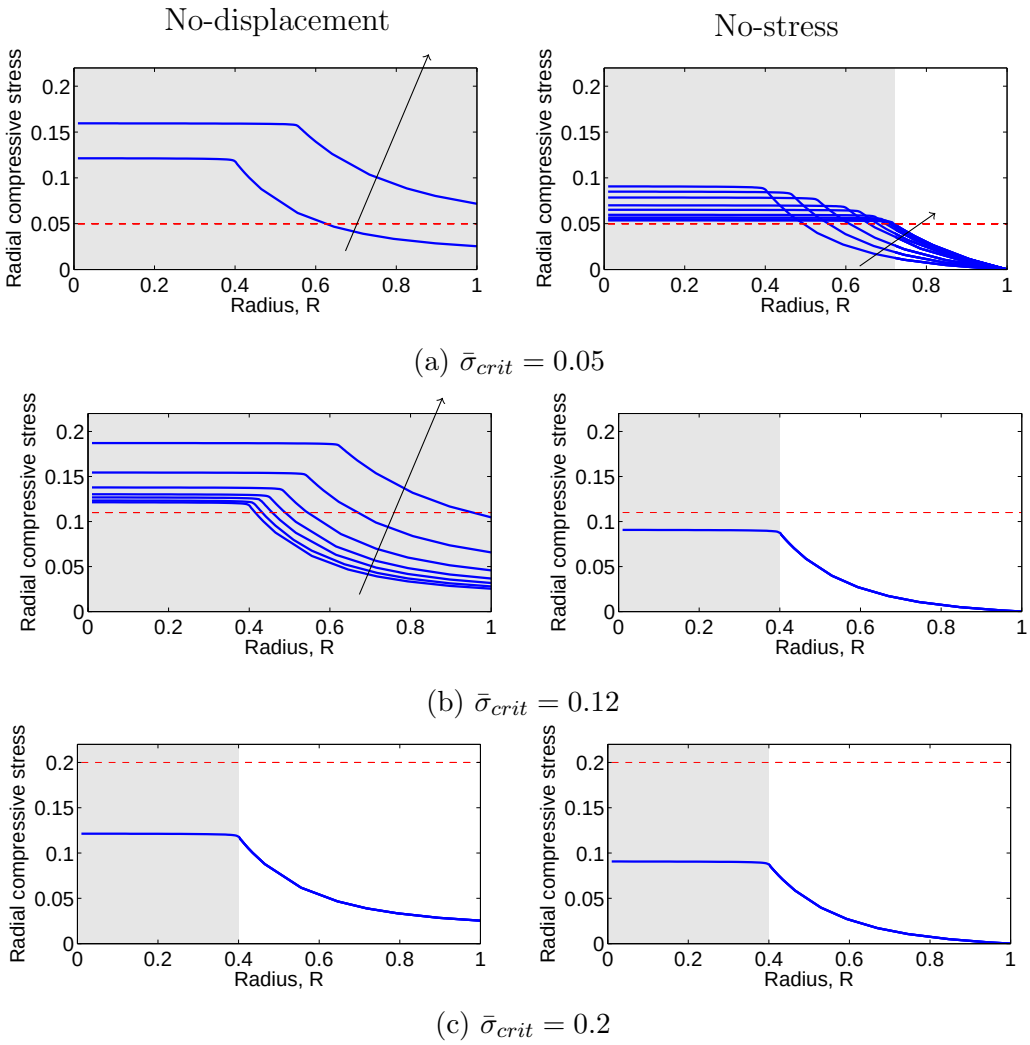

(a) $\bar{\sigma}_{crit} = 0.05$

(b) $\bar{\sigma}_{crit} = 0.12$

(c) $\bar{\sigma}_{crit} = 0.2$

Figure 5.10: Figure showing profiles of the radial compressive stress ($-\mathbf{e}_r \cdot \boldsymbol{\sigma} \cdot \mathbf{e}_r$) through a sphere of tissue at successive iterations, for three different values of $\bar{\sigma}_{crit}$. Each solid curve corresponds to a single iteration, with arrows in the direction of increasing number of iterations, and the red dashed lines corresponding to $\bar{\sigma}_{crit}$. The grey shaded region shows the final radius of damage, $R_{(\infty)}$. No-displacement boundary condition is shown in the left column, and no-stress in the right column. Parameters: $R_{(1)} = 0.4$, $H = 1$cm, all other parameters in Table 5.1.

the no-stress boundary conditions, the larger of the two critical stresses ($\bar{\sigma}_{crit} = 0.12, 0.2$) do not allow damage to propagate, whilst the lowest ($\bar{\sigma}_{crit} = 0.05$) allows damage to propagate up to $R_{(\infty)} \sim 0.7$.

The observation that damage is halted under no-stress boundary conditions, yet propagates through the entire tissue under no-displacement boundary conditions, is consistent with the experimental results of Walberer *et al.* (2008). They showed that following an initial ischemic stroke the final size of damaged region is greater in animals who had not undergone a craniectomy. Our results provide a possible mechanical explanation for these

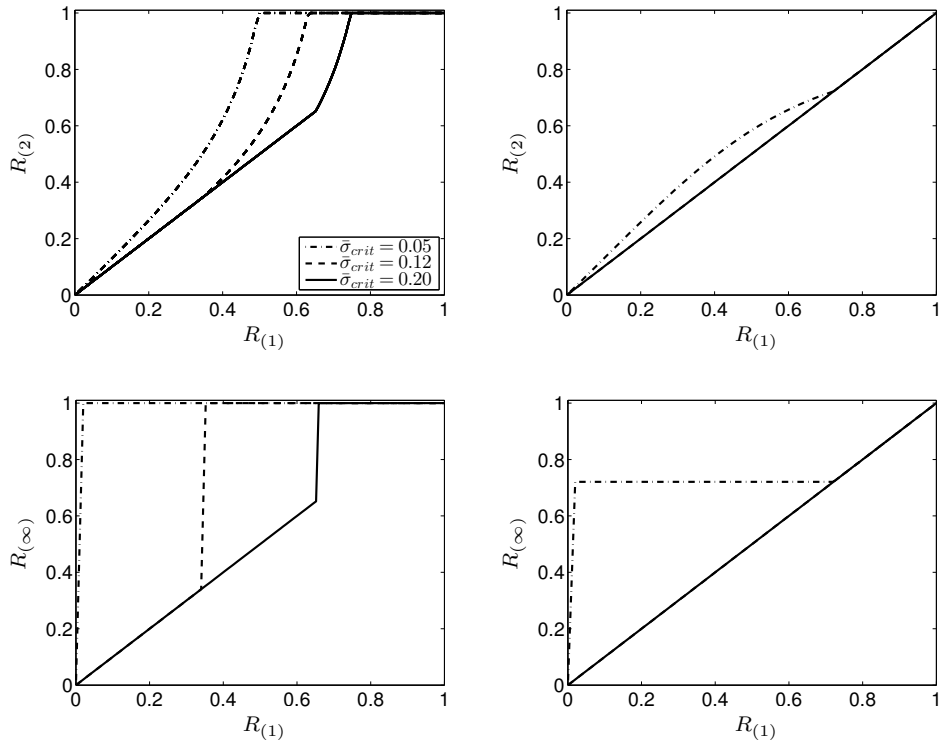

(a) No-displacement (b) No-stress

Figure 5.11: Map of $R_{(1)}$ to $R_{(2)}$ (upper figures) and $R_{(1)}$ to $R_{(\infty)}$ (lower figures), for (a) no-displacement and (b) no-stress boundary conditions. Dot-dashed curves correspond to $\bar{\sigma}_{crit} = 0.05$, dashed curves to $\bar{\sigma}_{crit} = 0.12$, and solid curves to $\bar{\sigma}_{crit} = 0.2$. In (b), the solid and dashed curves overlap. Parameters: $H = 1$cm, all other parameters in Table 5.1.

experimental results.

5.4.3 Stress damage versus stretch damage

Up to this point, we have only considered compressive stress as a mechanism of damage in the tissue. Using this measure, our results indicate that craniectomy always leads to a better outcome, as the relief of stress prevents propagation of damage. However, in cohort studies of human patients, Cooper *et al.* (2011) observed that whilst a decompressive craniectomy reduces intracranial pressure, the procedure actually leads to more unfavourable outcomes for patients (such as death, vegetative state, or severe disability). They propose that this is because the craniectomy causes axonal stretch and leads to neural injury. As discussed in §1.2.3, the degree of axonal damage depends on both the magnitude and the rate of stretch. However, experimental studies indicate that strains above $\approx$15% can lead to electrophysiological and structural damage to axons (Bain and Meaney, 2000).

We therefore consider a second measure of damage, stretch damage, for both sets of boundary conditions. Since stretch damage is believed to result directly from stretch of axons, Figure 5.12 shows the maximum stretch in the healthy tissue ($R > R_{(n)}$) after successive iterations, as a function of the initial damaged radius $R_{(1)}$. We observe that the maximum stretch is greater for no-stress boundary conditions, for all values of the initial radius of damage $R_{(1)}$. This is because the no-stress boundary conditions allow the tissue to stretch outwards. Thus, a craniectomy may not always lead to the beneficial consequences that might be expected when studying only propagation. Instead it may be necessary to consider a trade-off between preventing ischemic damage propagation and minimising stretch damage to axons.

5.5 Analytic iteration scheme for a linear elastic model

In this final section, we continue to investigate the mechanics-only damage model (described in §5.3.3), but now we further simplify it by using governing equations valid for infinitesimally small deformations. The assumption of small deformations allows the governing equation (5.24) and boundary conditions (5.28), (5.30), (5.32) to be simplified enough that analytical solutions for the displacement, stretch and stress may be obtained at each iteration.

We are especially interested in the relations between the initial radius of damage, $R_{(1)}$ and the final damage radius $R_{(\infty)}$. In the infinitesimal framework we will show that in terms of the initial damage radius $R_{(1)}$, we are able to find $R_{(2)}$ and $R_{(\infty)}$ algebraically.

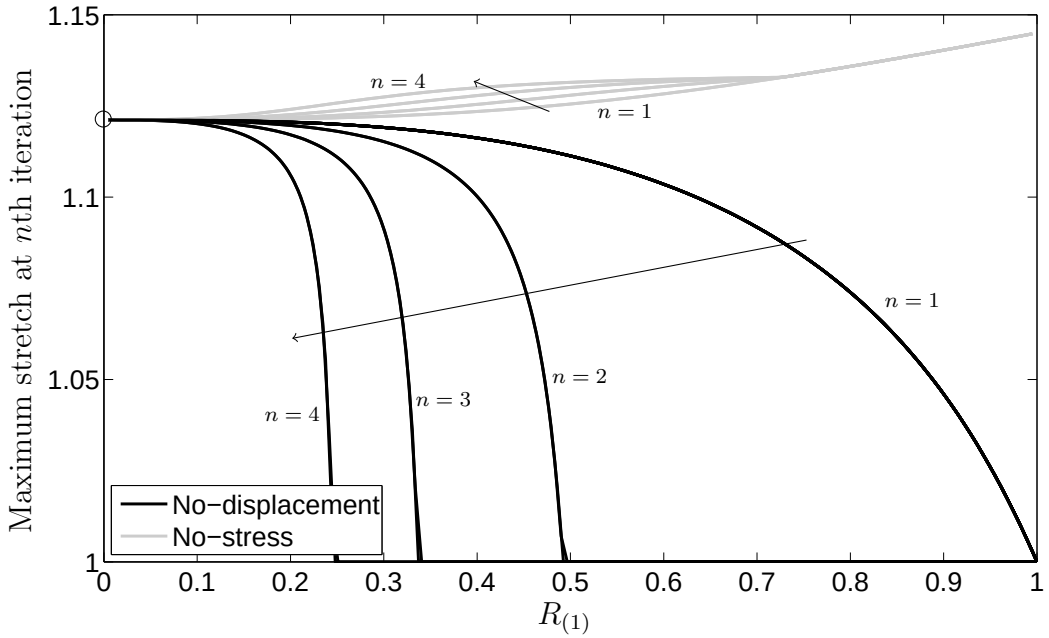

Figure 5.12: Figure showing the maximum stretch in the healthy tissue ($R_{(n)} < R < 1$) at successive iterations, as a function of the initial damage radius $R_{(1)}$. To calculate the maximum stretch we take the local maximum of the radial stretch ($f'_{(n)} - 1$) and circumferential stretch ($f_{(n)}/R - 1$). Black curves show no-displacement boundary conditions and grey curves show no-stress boundary conditions, with the arrows in the direction of successive iterations. Parameters: $H = 1$cm, $\bar{\sigma}_{crit} = 0.05$, all other parameters in Table 5.1.

This simplification allows us to investigate analytically the importance of different model parameters and boundary conditions on these propagation effects.

5.5.1 Inner and outer solutions

In the infinitesimal framework, deformations are assumed to be small and thus the Eulerian (r) and Lagrangian (R) frames are the same to leading order.

At the nth iteration we have a particular damage radius $R_{(n)}$, such that $\bar{c}_0^f = \bar{c}_{0\,I}^f$ for $0 \leq r \leq R_{(n)}$ (the inner region), and $\bar{c}_0^f = 0$ for $R_{(n)} < r \leq 1$ (the outer region). Let us consider each of these regions separately. We define $u_{I(n)}(r)$, $u_{O(n)}(r)$ as the radial displacement in the inner and outer regions respectively. In each region the linear strain tensor is defined $\mathbf{e}_{i(n)} = \mathrm{diag}[\mathrm{d}u_{i(n)}/\mathrm{d}r, u_{i(n)}/r, u_{i(n)}/r]$, and the dilation as,

$$e_{i(n)} = \mathrm{tr}(\mathbf{e}_{i(n)}) = \frac{1}{r^2}\frac{\partial}{\partial r}\left(r^2 u_{i(n)}\right), \qquad (i = I, O), \tag{5.33}$$

We use the infinitesimal stress tensor for the effective Cauchy stress (see Appendix A), so that $\boldsymbol{\sigma}_{ei(n)} = \bar{\lambda}_s e_{i(n)}\mathbf{I} + 2\bar{\mu}_s \mathbf{e}_{i(n)}$. In infinitesimal deformation elasticity, the osmotic term in the Cauchy stress tensor (5.9) may be linearised. Then,

$$\boldsymbol{\sigma}_{i(n)} = \boldsymbol{\sigma}_{ei(n)} - \left[\sqrt{\bar{c}_{0\,i}^{f\;2} + \bar{c}^{*2}} - \bar{c}^* - \left(\frac{\bar{c}_{0\,i}^{f\;2}}{\phi_0^w \sqrt{\bar{c}_{0\,i}^{f\;2} + \bar{c}^{*2}}}\right) e_{i(n)}\right]\mathbf{I}, \tag{5.34}$$

where $\bar{c}_{0\,I}^f$ is a constant in the inner region, and $\bar{c}_{0\,O}^f = 0$ in the outer region.

In each region the stress satisfies $\nabla \cdot \boldsymbol{\sigma}_{i(n)} = \mathbf{0}$. Substituting in the Cauchy stress, (5.34), we find that

$$0 = \frac{\partial}{\partial r}\left(\frac{1}{r^2}\frac{\partial}{\partial r}\left(r^2 u_{i(n)}\right)\right), \tag{5.35}$$

in both the inner and outer regions. The general solution of equation (5.35) is,

$$u_{i(n)} = a_{i(n)} r + \frac{b_{i(n)}}{r^2}, \tag{5.36}$$

where $a_{i(n)}$ and $b_{i(n)}$ are constants that must be determined from the boundary conditions.

At the origin, we have a no-displacement boundary condition,

$$u_{I(n)}\big|_0 = 0, \tag{5.37}$$

which immediately gives $b_{I(n)} = 0$. At the boundary between the outer and inner region,

both the radial component of stress and the displacement must be continuous. Thus,

$$u_{I(n)}\big|_{R_{(n)}} = u_{O(n)}\big|_{R_{(n)}}, \qquad \hat{\mathbf{e}}_r \cdot \boldsymbol{\sigma}_{I(n)}\big|_{R_{(n)}} \cdot \hat{\mathbf{e}}_r = \hat{\mathbf{e}}_r \cdot \boldsymbol{\sigma}_{O(n)}\big|_{R_{(n)}} \cdot \hat{\mathbf{e}}_r. \tag{5.38}$$

At the outer edge, we apply either no-displacement or no-stress,

$$u_{O(n)}\big|_1 = 0, \qquad \text{or} \qquad \hat{\mathbf{e}}_r \cdot \boldsymbol{\sigma}_{O(n)}\big|_1 \cdot \hat{\mathbf{e}}_r = 0. \tag{5.39}$$

We may now substitute the general expression for the displacement (5.36) into the boundary conditions (5.37)-(5.39) to determine the unknown coefficients $a_{i(n)}$, $b_{i(n)}$. Once $u_{i(n)}$ is determined, it is a simple matter to determine $\boldsymbol{\sigma}_{i(n)}$ and hence the region of r for which the maximal compressive stress $\sigma_{max(n)} > \bar{\sigma}_{crit}$. We consider the cases of no-displacement and no-stress boundary conditions separately.

5.5.2 No-displacement outer boundary (intact skull)

We first consider the no-displacement outer boundary condition ($u_{O(n)}\big|_1 = 0$). Using equation (5.36) and boundary conditions (5.37)-(5.39) we find that the solutions for the inner and outer displacement may be written

$$u_{I(n)} = A_{(n)} \left(\frac{1}{R_{(n)}^3} - 1 \right) r, \qquad u_{O(n)} = A_{(n)} \left(\frac{1}{r^2} - r \right), \tag{5.40}$$

where the value of $A_{(n)}$ depends on $R_{(n)}$ according to

$$A_{(n)} := A(R_{(n)}) = \frac{\alpha_1 R_{(n)}^3}{\alpha_2 - 3R_{(n)}^3 \alpha_3}, \tag{5.41}$$

where the constants α_1, α_2, α_3 are given by,

$$\alpha_1 = \sqrt{\bar{c}_{0I}^{f\,2} + \bar{c}^{*2}} - \bar{c}^*, \qquad \alpha_2 = 3\bar{\kappa}_s + 4\bar{\mu}_s + 3\alpha_3, \qquad \alpha_3 = \frac{\bar{c}_{0I}^{f\,2}}{\phi_0^w \sqrt{\bar{c}_{0I}^{f\,2} + \bar{c}^{*2}}}, \tag{5.42}$$

and $\bar{\kappa}_s = \bar{\lambda}_s + 2/3\bar{\mu}_s$ is the dimensionless bulk modulus. Using the general form of the Cauchy stress tensor (5.34), the maximal compressive stress (see 5.10) in the tissue is,

$$\sigma_{max(n)}(r) = \begin{cases} \alpha_1 - 3A_{(n)} \left(\bar{\kappa}_s + \alpha_3 \right) \left(\dfrac{1}{R_{(n)}^3} - 1 \right), & r \le R_{(n)}, \\ A_{(n)} \left(3\bar{\kappa}_s + \dfrac{4\bar{\mu}_s}{r^3} \right), & r > R_{(n)}. \end{cases} \tag{5.43}$$

Equation (5.43) shows that at every step of the iteration, the maximum compressive Cauchy stress is constant within the inner region ($0 < r < R_{(n)}$), and monotonic decreasing in the outer region ($R_{(n)} < r < 1$). This trend agrees well with the numerical results obtained in §5.4.2 (see Figure 5.10) for the finite elasticity case.

For some radius of damage $R_{(n)}$, we now consider the damage radius following one iteration, $R_{(n+1)}$. Following the procedure described in §5.3.3, there are three cases to consider. Firstly, if the maximal compressive stress in the tissue $\sigma_{max(n)}(r)$ is below the critical stress $\bar{\sigma}_{crit}$ everywhere, then damage does not propagate and $R_{(n+1)} = R_{(n)}$. Secondly, if there is some value of $R_{(n+1)}$ such that $R_{(n)} < R_{(n+1)} < 1$ and $\sigma_{max(n)}(R_{(n+1)}) = \bar{\sigma}_{crit}$, then the damage will propagate up to that value. Thirdly, if the compressive stress $\sigma_{max(n)}(r)$ exceeds the critical stress $\bar{\sigma}_{crit}$ everywhere, then the entire tissue is damaged and hence $R_{(n+1)} = 1$.

Which of these three cases we are in depends on the size of $R_{(n)}$, relative to two length scales r_a and r_b,

$$r_a = \left(\frac{\alpha_2 \bar{\sigma}_{crit} - 4\alpha_1 \bar{\mu}_s}{3(\alpha_1 \bar{\kappa}_s + \alpha_3 \bar{\sigma}_{crit})} \right)^{1/3}, \qquad r_b = \left(\frac{\alpha_2 \bar{\sigma}_{crit}}{4\alpha_1 \bar{\mu}_s + 3(\alpha_1 \bar{\kappa}_s + \alpha_3 \bar{\sigma}_{crit})} \right)^{1/3}, \tag{5.44}$$

which are the values of $R_{(n)}$ such that $\sigma_{max(n)}(R_{(n)}) = \bar{\sigma}_{crit}$ and $\sigma_{max(n)}(n) = \bar{\sigma}_{crit}$ respectively. These three cases can be summarised as,

$$R_{(n+1)} = \begin{cases} R_{(n)}, & \text{for } R_{(n)} \leq r_a \\ \left(\dfrac{(r_b^3 - r_a^3) R_{(n)}^3}{r_b^3(1 - r_a^3) - R_{(n)}^3(1 - r_b^3)} \right)^{1/3}, & \text{for } r_a < R_{(n)} \leq r_b \\ 1, & \text{for } R_{(n)} > r_b \end{cases} \tag{5.45}$$

where the middle line in equation (5.45) is obtained by finding the value of $R_{(n+1)}$ such that $\sigma_{max(n)}(R_{(n+1)}) = \bar{\sigma}_{crit}$ in equation (5.43). This iterative map is shown in Figure 5.13.

Ultimately given some initial radius of damage, $R_{(1)}$, we are interested in finding $R_{(\infty)}$, the final radius of damage. We thus consider fixed points R^* of the iterative map (5.45), by seeking solutions to (5.45) such that $R^* = R_{(n)} = R_{(n+1)} \forall n \geq 1$. It is trivial to observe that R^* can take all values less than or equal to r_a, and also 1. However, R^* cannot take any values between r^a and 1 [3].

[3] If $r_a < R_{(n)} \leq r_b$, then using the iterative map (5.45) for no-displacement boundary conditions we can show,

$$R_{(n+1)}^3 - R_{(n)}^3 = R_{(n)}^3 \left(\frac{(1 - r_b^3)(R_{(n)}^3 - r_a^3)}{r_b^3(R_{(n)}^3 - r_a^3) + (r_b^3 - R_{(n)}^3)} \right). \tag{5.46}$$

Since $r_a < R_{(n)} \leq r_b$, both the denominator and numerator in the above expression are positive, and

We now consider the final radius of damage, $R_{(\infty)}$, for a given initial radius of damage $R_{(1)}$. If $R_{(1)} \leq r_a$, then $R_{(1)}$ is a fixed point of the map; damage does not propagate and trivially $R_{(\infty)} = R_{(1)}$. Rearranging the expression (5.45), we find that if $r_a < R_{(n)} \leq r_b$ then $R_{(n+1)} > R_{(n)}$ (see footnote 3). Thus if $r_a < R_{(1)} \leq r_b$ then the damage radius $R_{(n)}$ will increase at each iteration until $R_{(n)} > r_b$, following which $R_{(n+1)}$ reaches a fixed point so that $R_{(\infty)} = 1$; propagation is halted as the entire tissue is damaged. Finally, if $r_b < R_{(1)} \leq 1$ then $R_{(\infty)} = 1$. Thus,

$$R_{(\infty)} = \begin{cases} R_{(1)}, & \text{if } R_{(1)} \leq r_a, \\ 1, & \text{if } R_{(1)} > r_a. \end{cases} \tag{5.47}$$

This result agrees qualitatively with the results of the numerical simulations in finite elasticity, which showed that for no-displacement boundary conditions, if damage is initiated then the damage will continue to propagate through the entire tissue. In this linear case, we have shown algebraically that propagation will be initiated provided $R_{(1)} > r_a$. Furthermore, if $R_{(n)} > r_a$ then $R_{(n+1)}$ is always greater than $R_{(n)}$. Thus propagation continues until the entire tissue is damaged.

5.5.3 No-stress outer boundary (craniectomy)

We now consider the no-stress outer boundary condition ($\hat{\mathbf{e}}_r \cdot \boldsymbol{\sigma}_{O(n)}\big|_1 \cdot \hat{\mathbf{e}}_r = 0$). Using equation (5.36) and boundary conditions (5.37)-(5.39) we find that the solutions for the inner and outer displacement may be written,

$$u_{I(n)} = B_{(n)} \left(\frac{4\bar{\mu}_s}{3\bar{\kappa}_s} + \frac{1}{R_{(n)}^3} \right) r, \qquad u_{O(n)} = B_{(n)} \left(\frac{4\bar{\mu}_s}{3\bar{\kappa}_s} r + \frac{1}{r^2} \right), \tag{5.48}$$

where $B_{(n)}$ is a function of $R_{(n)}$ defined by,

$$B_{(n)} := B(R_{(n)}) = \frac{\bar{\kappa}_s \alpha_1 R_{(n)}^3}{\bar{\kappa}_s \alpha_2 + 4\bar{\mu}_s \alpha_3 R_{(n)}^3}, \tag{5.49}$$

the constants α_1, α_2, α_3 are given by equation (5.42).

Using the general form of the Cauchy stress tensor (5.34), we can also write the

therefore $R_{(n+1)}^3 - R_{(n)}^3 > 0$. Hence, $R_{(n+1)} > R_{(n)}$ if $r_a < R_{(n)} \leq r_b$, and thus there are no fixed points in $r_a < R_{(n)} \leq r_b$.

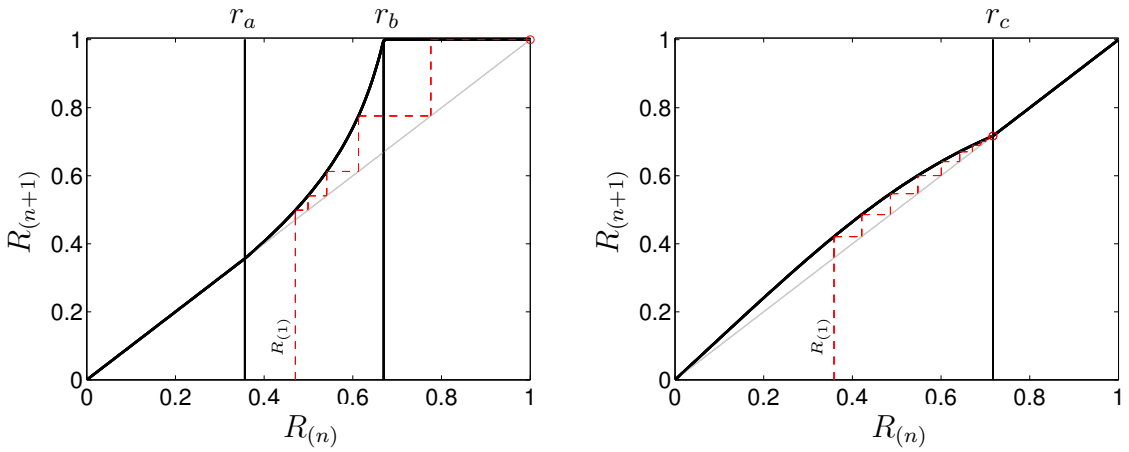

(a) No-displacement (b) No-stress

Figure 5.13: Black curves show plots of the iterative relationships between $R_{(n)}$ and $R_{(n+1)}$, given by a) equation (5.45), for no-displacement boundary conditions, and b) equation (5.52) for no-stress boundary conditions. The vertical black lines show the critical values of $R_{(n)}$ found in equations (5.44) and (5.51), while the grey lines show $R_{(n+1)} = R_{(n)}$. The dashed red lines show the damage radius at successive iterations, beginning at a particular $R_{(1)}$; we observe that a) the final damage radius $R_{(\infty)} = 1$, and b) the final damage radius $R_{(\infty)} = r_c$, agreeing with the predictions made in equations (5.47) and (5.53). Parameters: a) $\bar{\sigma}_{crit} = 0.1$, b) $\bar{\sigma}_{crit} = 0.05$, all other parameters are as in Table 5.1.

maximum compressive Cauchy stress in each of the inner and outer regions,

$$\sigma_{max(n)}(r) = \begin{cases} \alpha_1 - 3\left(\bar{\kappa}_s + \alpha_3\right) B_{(n)}\left(\dfrac{4\bar{\mu}_s}{3\bar{\kappa}_s} + \dfrac{1}{R_{(n)}^3}\right), & r \leq R_{(n)}, \\ 4\bar{\mu}_s B_{(n)}\left(\dfrac{1}{r^3} - 1\right), & r > R_{(n)}. \end{cases} \tag{5.50}$$

Again, we observe that $\sigma_{max(n)}$ is constant for $r \leq R_{(n)}$ and monotonic decreasing for $r > R_{(n)}$, consistent with the stress profiles shown in Figure 5.10 for the finite elasticity case.

We now consider the relationship between the radius of damage at the nth iteration, $R_{(n)}$, and the radius of damage after a further iteration, $R_{(n+1)}$. We find that there is a value r_c,

$$r_c = \left(1 - \frac{\bar{\sigma}_{crit}(\bar{\kappa}_s\alpha_2 + 4\bar{\mu}_s\alpha_3)}{4\bar{\mu}_s\left(\bar{\kappa}_s\alpha_1 + \bar{\sigma}_{crit}\alpha_3\right)}\right)^{1/3}, \tag{5.51}$$

such that $\sigma_{max(n)}(R_{(n)}) \geq \bar{\sigma}_{crit}$ if $R_{(n)} \leq r_c$ and $\sigma_{max(n)}(R_{(n)}) < \bar{\sigma}_{crit}$ if $R_{(n)} > r_c$. Note

that $r_c < 1$. We find an expression for $R_{(n+1)}$,

$$R_{(n+1)} = \begin{cases} \left(\dfrac{4\bar{\mu}_s B_1}{\bar{\sigma}_{crit} + 4\bar{\mu}_s B_1} \right)^{1/3}, & R_{(n)} \leq r_c, \\ R_{(n)}, & R_{(n)} > r_c, \end{cases} \tag{5.52}$$

where the uppermost line in equation (5.52) is obtained by setting $\sigma_{max(n)}(R_{(n+1)}) = \bar{\sigma}_{crit}$ in equation (5.50), and r_c is the value of $R_{(n)}$ such that $\sigma_{max(n+1)}(R_{(n)}) = \bar{\sigma}_{crit}$. This iterative map is shown in Figure 5.13. We observe that if $\bar{\sigma}_{crit} > 4\bar{\mu}_s\alpha_1/\alpha_2$ then there are no positive values for r_c. In this case no propagation can occur, since then $R_{(n+1)} = R_{(n)}$ for all positive $R_{(n)}$.

Finally, we consider the fixed points R^* of the map (5.52), in order to identify the relationship between the initial damage radius $R_{1)}$ and the final damage radius $R_{(\infty)}$. By seeking solutions of (5.52) for which $R^* = R_{(n+1)} = R_{(n)} \forall n \geq 1$, we find that there are no fixed points that take values less than r_c (since $R_{(n+1)} > R_{(n)}$ if $R_{(n)} < r_c$), but observe that all radial values greater than r_c are fixed points. Furthermore, rearrangement of equation (5.52) gives that $R_{(n+1)} \leq r_c$ if $R_{(n)} \leq r_c$. Thus,

$$R_{(\infty)} = \begin{cases} r_c, & \text{if } R_{(1)} \leq r_c, \\ R_{(1)}, & \text{if } R_{(1)} > r_c. \end{cases} \tag{5.53}$$

Expression (5.53), shows that if the initial damage radius $R_{(1)} < r_c$, then damage will propagate up to r_c. However if $R_{(1)} \geq r_c$ then no propagation will occur. Therefore, provided $r_c < 1$, damage will not propagate through the entire tissue. This result agrees qualitatively with observations made in §5.4.2 for the finite deformation case.

5.5.4 Comparison of infinitesimal and finite results

In §5.4.2 we investigated propagation effects using the mechanics-only damage iteration process and finite deformation elasticity. We showed that under no-displacement outer boundary conditions, if damage is initiated then the radius of damage will continue at each iteration until the entire tissue is damaged. However under no-stress outer boundary conditions, damage does not propagate through the tissue. In §5.5.2 and §5.5.3 we showed analytically that these observations are also observed in infinitesimal elasticity. In this final section, we compare results of the finite and infinitesimal models.

In Figure 5.14, we compare the maps of $R_{(2)}$ as a function of $R_{(1)}$ calculated using the finite (see §5.4.2) and infinitesimal (equations (5.45), (5.52)) models. Results are shown for two different values of $\bar{\sigma}_{crit}$. We observe that the curves have similar shapes, although

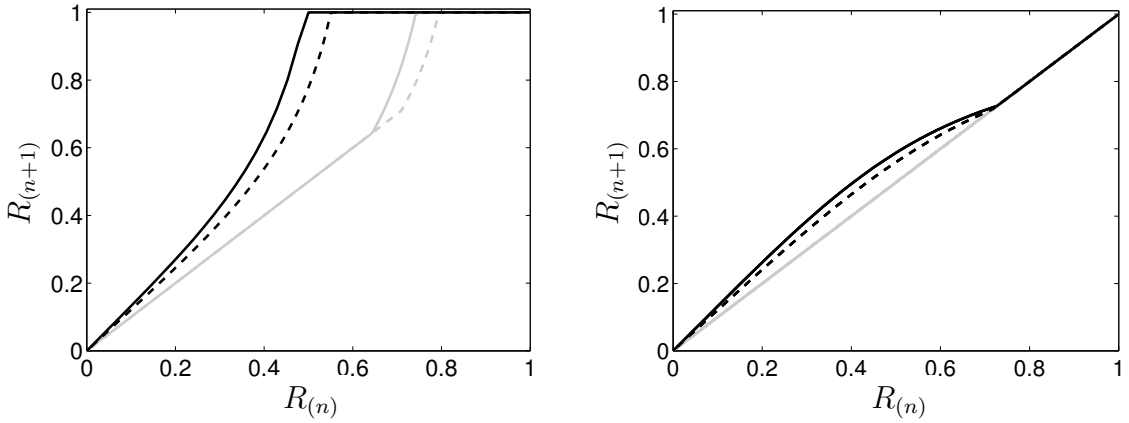

(a) No-displacement (b) No-stress

Figure 5.14: Comparison of maps from $R_{(n)}$ to $R_{(n+1)}$ computed using the analytic, infinitesimal elasticity approach (dashed curves) and numerical, finite elasticity approach (solid curves). Parameters: $\bar{\sigma}_{crit} = 0.2$ (grey) and $\bar{\sigma}_{crit} = 0.05$ (black). In (b), the solid and dashed grey curves overlap. All other parameters are as in Table 5.1.

the curves computed for infinitesimal deformations fall below of those for finite. This indicates that the maximum compressive stress in the tissue is smaller when computed using a infinitesimal rather than finite deformation model.

In Figure 5.15 we show profiles of radial compressive stress and radial stretch through the tissue, calculated using both the finite and infinitesimal models. The upper curves show results for $\bar{c}^f_{0I} = 40$, which is the value used throughout this chapter (see Table 5.1). We observe that, as expected, the compressive stress calculated using the infinitesimal deformation model falls slightly below that calculated using the finite deformation model. However, if $\bar{c}^f_{0I}$ is reduced to 10, so that smaller deformations are induced, the finite and infinitesimal results are indistinguishable on the scale of this plot. This confirms that the finite deformation model does indeed reduce to the infinitesimal under small deformations.

For the simulations in this chapter we have used a neo-Hookean constitutive law for the stress-strain relationship of the mixture, which exhibits similar behaviour to the infinitesimal tensor under the magnitudes of strain that we have investigated (see Figure 2.3). If we had chosen a constitutive law with a different stress-strain relationship, for example a Fung law with unphysiological strain-stiffening parameter $c = 16.5$ Pa, then we would not expect the finite and infinitesimal deformation models to display similar behaviour at large strains.

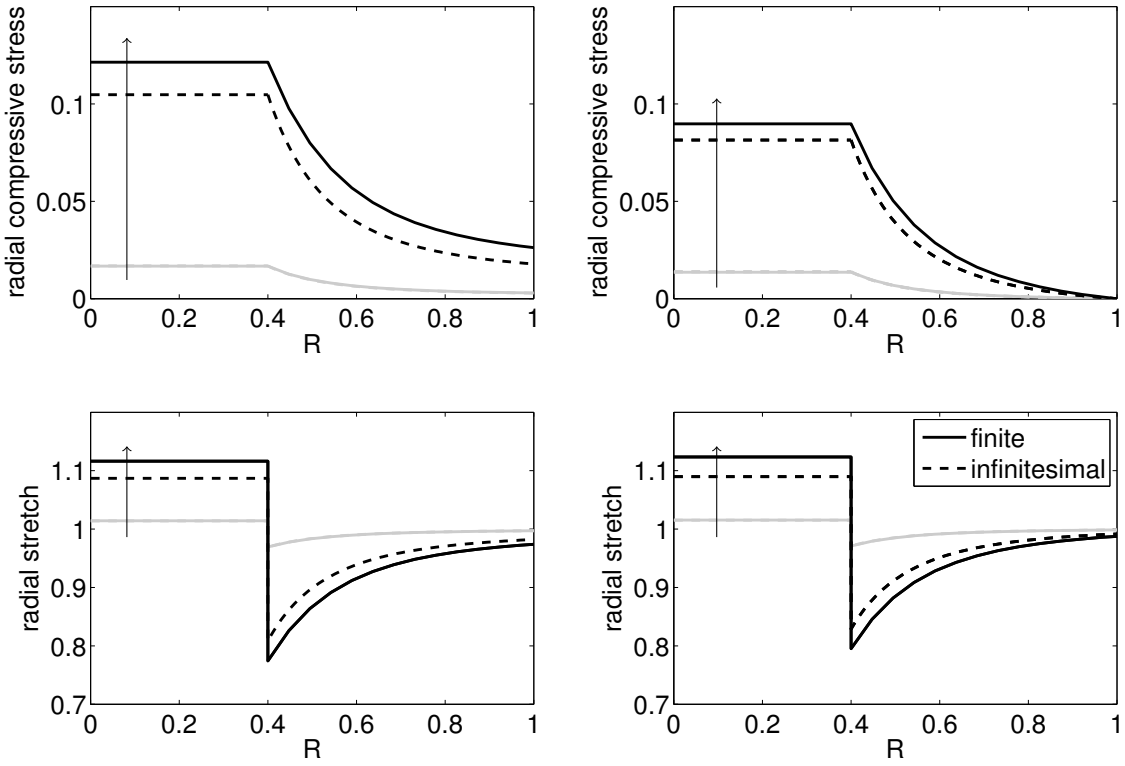

(a) No-displacement (b) No-stress

Figure 5.15: Comparison of radial stress ($-\hat{\mathbf{e}}_r \cdot \boldsymbol{\sigma} \cdot \hat{\mathbf{e}}_r$) and stretch ($f' - 1$ for the finite case, u' for the infinitesimal case) profiles using the computational finite approach (solid curves) and the analytical infinitesimal approach (dashed curves). We show profiles for $\bar{c}^f_{0I} = 10$ (grey) and $\bar{c}^f_{0I} = 40$ (black), with arrows in direction of increasing $\bar{c}^f_{0I}$. When $\bar{c}^f_{0I} = 10$, the finite and infinitesimal curves are indistinguishable on the scale of this plot.

5.6 Discussion

We have formulated a model to investigate the propagation of damage, caused by edema, through brain tissue. Our model couples a diffusion-uptake equation for oxygen, with a triphasic model for the tissue mechanics. Swelling is driven by exposure of intracellular FCD, assumed to be a consequence of low oxygen concentrations.

We have used a simple model for diffusion and uptake of oxygen in the tissue, and assumed that capillaries act as an oxygen source of fixed concentration when they are open. With this simple model, we have shown that explicitly modelling the oxygen concentration within the tissue is relatively unimportant at the tissue scale. Indeed, qualitatively similar results may be obtained by assuming that tissue becomes infarcted if it experiences a compressive stress above the critical value, leading to exposure of intracellular FCD.

Our model indicates that damage will propagate further through the tissue when the skull is intact than when a craniectomy is performed. This result agrees with the experimental results of Walberer *et al.* (2008), who showed that performing a craniectomy prior to stroke resulted in a smaller infarcted region in rats. However we have also shown that, despite the final volume of damage being smaller, the remaining tissue experiences a greater stretch if a craniectomy is performed.

We have made simplistic assumptions for the levels of stress and oxygen which result in damage propagation. For oxygen we have assumed that all open capillaries contain oxygen at a fixed concentration, and that when tissue oxygen concentration falls below a threshold $\mathcal{C}_{crit}$ the tissue becomes ischemic. However, thresholds for ischemia are often defined in terms of the rate of blood flow per volume of brain tissue, and a more complex model coupling oxygen extraction to blood flow (for example Østergaard *et al.*, 2013) may produce interesting results. For the mechanics of capillary closure, we assume that capillaries close when compressive stress in the tissue exceeds a certain level σ_{crit}. A more sophisticated model could be developed to couple the swelling of the tissue to capillary collapse. To our knowledge a model of this type do not exist for edema, but similar models have been developed, for example, to investigate capillary collapse in growing tumours (MacLaurin *et al.*, 2012).

Representing a craniectomy by imposing no-stress over the entire tissue surface is highly simplistic. Medically, only a small region of skull is removed when a craniectomy is performed. Furthermore, it is unlikely that the brain tissue truly experiences free swelling when the skull is removed, since there are layers of membrane on the surface of the brain which remain intact when a craniectomy is performed. To investigate more realistic boundary conditions, future work could incorporate a more complex geometry.

Our approach to studying the consequences of a craniectomy has been purely mechanical. There are multiple factors beyond mechanics which may affect clinical decisions as to whether a craniectomy is performed (*e.g.* risks of metabolic disturbances or infection (Fisher and Garcia, 1996)). However, to our knowledge this is the first mathematical model to investigate the mechanical propagation of brain tissue edema, and further biological factors could be incorporated in future work.

Chapter 6

Discussion

6.1 Key findings

In this thesis, we have used a mixture theory approach to investigate the causes and consequences of brain tissue swelling. We considered three particular problems, motivated by experimental observations in swelling brain tissue.

Firstly, in Chapter 3 we investigated the swelling of brain tissue slices. Experimental results of Elkin *et al.* (2010) showed that dead brain tissue slices swell by $\approx 74\%$ in an isotonic solution bath, and that reducing the ionic concentration of the bath results in greater swelling, whilst increasing the ionic concentration of the bath leads to decreased swelling. We investigated mechanisms that could explain these results.

Elkin *et al.* (2010) proposed that brain tissue swelling is caused by intracellular FCD becoming exposed when brain cells are damaged. This FCD leads to an increased ion concentration in the tissue (in the relation to the ionic bath) due to the Donnan effect, leading to osmotic pressure gradients that drive water movement into the tissue and cause swelling. We showed that the osmotic pressure generated by the Donnan effect alone is insufficient to explain the swelling observed experimentally. Instead, we hypothesise that the observed swelling is due to a combination of the Donnan effect, and an accumulation of non-permeating (electrically) neutral solutes within the tissue.

Secondly, in Chapter 4 we focussed on blood brain barrier (BBB) failure and edema. We identified a key parameter, the dimensionless BBB permeability, as critical to whether edema can develop. Under physiological conditions this parameter is small and the tissue experiences little deformation. However if the BBB permeability increases 100-fold, as occurs in brain edema, then tissue pressure increases and the tissue undergoes swelling and deformation.

While other authors (see Nagashima *et al.*, 1990, for example) have investigated the effect of a specified change in BBB permeability within a specific, realistic geometry,

we adopted a more systematic and general approach. For simplicity we considered a spherically symmetric geometry, and considered dynamics, the importance of finite deformations, and the role of boundary conditions in turn. Physiological edema develops more slowly than the timescales suggested by the model, indicating that the dynamic evolution of edema is governed by biological rather than physical effects. Other authors (see Nagashima *et al.*, 1990; Smith and Humphrey, 2007, for example) use an infinitesimal deformation approach to study the effects of BBB permeability increases; our comparison of modelling results from infinitesimal and finite models showed that these approaches yield qualitatively similar results, suggesting that an infinitesimal elasticity approach is sufficient to represent this system. Investigating the role of boundary conditions showed that the permeability of the tissue boundary to fluid has a great effect on the type of damage incurred in the tissue. A more permeable boundary results in the build up of large pressure gradients within the tissue (resulting in greater deformations) whilst a less permeable boundary causes a build up of stress within the tissue. Future work could investigate physiological mechanisms of edema fluid drainage within the brain, to identify which of these cases would be expected.

Thirdly, in Chapter 5 we proposed a coupled model for the oxygen distribution within, and mechanical swelling of, brain tissue. We made simplistic, but physiologically reasonable, assumptions about the coupling between the oxygen and mechanics, in assuming that capillaries close when they experience compressive stress over a critical threshold, and that tissue dies when it experiences an oxygen concentration below a critical threshold. To our knowledge, this is the first mathematical model that attempts to capture the phenomena of damage propagation in a swollen brain.

We showed that, if an initial region of damage is prescribed, the extent of damage propagation is greater if the tissue is subject to no-displacement boundary conditions (representing an intact skull) compared to no-stress boundary conditions (representing a craniectomy). These observations agree with the experimental results of Walberer *et al.* (2008), who showed that following an ischemic stroke, the final volume of damage was smaller in rats who had first been given a craniectomy. However, we also showed that the tissue experiences greater deformation when a craniectomy is performed, which may explain why a craniectomy does not reliably lead to more successful outcomes in patients.

6.2 Future directions

In this section, we discuss some of the directions and extensions that could be explored in future work.

Perhaps the biggest simplification we have made in the development of our models

has been on the geometries used. Throughout this thesis, we have modelled regions of brain tissue using simple cuboid or spherically symmetric geometries, and assumed that the tissue is homogeneous and isotropic. These simple geometries allowed analytical or simple numerical progress to be made. However, they do not allow for the shear stresses that the tissue would experience in pathophysiological swelling and craniectomy, and they also neglect the inhomogeneous, anisotropic nature of brain tissue (due to axonal tracts, and regional distributions of white and grey matter). Extending the model to a three dimensional, realistic brain geometry (see Nagashima *et al.*, 1990; Zhang *et al.*, 2004, for example) would allow realistic strain and stress distributions to be explored. However, to solve a triphasic model in this geometry would likely require the application of the finite element method (Sun *et al.*, 1999), adding to the numerical complexity of solutions and disallowing any analytical insight.

Surgically, a small region of skull is removed when a craniectomy is performed. This can lead to tearing and stretching of the tissue close to the skull opening. In Chapter 5, we used a simple boundary condition (no stress over the entire boundary) to represent a craniectomy. In a fully three dimensional geometry, a local craniectomy could be incorporated by changing the boundary conditions in just a local region of tissue, to further investigate the deformations caused by a craniectomy.

A further simplification was that we have not explicitly modelled the vascular network here. In Chapter 4, we explored the role of the blood brain barrier (BBB) and assumed that the vascular network acts as a source of edema fluid, with the rate of fluid flow across the BBB proportional to the pressure difference between the capillary and tissue. In Chapter 5 we investigated the concept that compressive stresses, due to edema, can cause capillaries to close (leading to ischemia and lack of oxygen). In both cases, we assumed that the pressure in the capillaries remained constant. This is a significant simplification, as the cerebral arteries autoregulate blood flow (by dilating or contracting) in response to changes in perfusion pressure (the difference between arterial pressure and intracranial pressure).

The relationship between cerebral blood flow and cerebral perfusion pressure, known as the autoregulation curve, is well documented in the biological literature (see Steiner and Andrews, 2006; Strandgaard *et al.*, 1973, for example). To incorporate a more realistic representation of the vasculature, a constitutive relation between local capillary pressure and local tissue pressure could be imposed (to allow cerebral blood flow to respond to changes in tissue pressure), based upon the autoregulation curve. An alternative approach could use multiple fluid network poroelasticity, based upon the approach of Tully and Ventikos (2011), so that the vasculature is modelled as a separate fluid network. This would allow fluid transfer between the vasculature and interstitial space to be modelled

explicitly.

Along with compressive stress, we have also considered the role of damage due to axonal stretch. We have made simplifying assumptions about the role of axonal stretch, assuming that greater tissue stretch correlates with greater axonal damage. However, experiments show that both the strain and strain rate affect the damage experienced by deformed axons. In a similar vein, it would be interesting to explore the rate at which the brain tissue swells outwards following a craniectomy. This may offer insight into the optimal timings of a craniectomy, with a view to reducing both the strain and strain rate to which the axons are exposed.

In summary, we have investigated mathematical models that couple the underlying pathophysiological causes of edema together with the mechanical deformations that occur in damaged brain tissue. To understand the complex behaviour of the brain requires coupling between systems from the subcellular to the organ scale. Our work offers some initial directions as to how the biological and mechanical aspects of the brain's behaviour may be integrated, and our results provide a basis for future research into the mechanics of brain edema.

Appendix A

Constitutive laws for strain energy functions

In this Appendix we summarise the strain energy functions and associated Cauchy stress tensors that are used throughout this work. These constitutive laws have been chosen because others have used them to represent brain tissue.

We only consider strain energy functions of isotropic materials. Throughout, λ_s and μ_s are the Lamé parameters. $\mathbf{F}$ is the deformation gradient tensor, $J = \det \mathbf{F}$ the volume change, $\mathbf{E} = (\mathbf{F} \cdot \mathbf{F}^T - \mathbf{I})/2$ the strain tensor, $\mathbf{u}$ the displacement, and λ_1, λ_2, λ_3 are the principal stretches.

Infinitesimal Stress Tensor

The infinitesimal stress tensor is valid only for small deformations, where the deformation is small compared to other length scales in the system. In this case the strain tensor may be approximated by a linear function of the displacement, $\mathbf{e} = (\nabla \mathbf{u} + \nabla \mathbf{u}^T)/2$, and the general form of the strain tensor is,

$$\boldsymbol{\sigma}_e = \lambda_s \mathrm{tr}(\mathbf{e}) \boldsymbol{I} + 2\mu_s \mathbf{e}. \tag{A.1}$$

Neo-Hookean

A neo-Hookean material is typically used for rubber-like materials. The general form of the strain energy function for a compressible neo-Hookean material is,

$$W = \frac{\mu_s}{2}(\lambda_1^2 + \lambda_2^2 + \lambda_3^2 - 3) + f(J) \tag{A.2}$$

where $f(J)$ is a function such that $f(1) = 0$. This $f(J)$ is referred to as the volumetric term and accounts for the compressibility of the material; the condition $f(1) = 0$ is required so that the volumetric term does not contribute when there is no volume change.

Two common forms of the volumetric component are a logarithmic term (p.162 (Bonet and Wood, 1997)),

$$f(J) = -\mu_s \ln J + \frac{\lambda_s}{2}(\ln J)^2, \tag{A.3}$$

or an algebraic (Ogden, 1984),

$$f(J) = -\mu_s \ln J + \frac{\lambda_s}{2}(J-1)^2. \tag{A.4}$$

For the logarithmic volumetric component the Cauchy stress tensor is,

$$\boldsymbol{\sigma}_e = \frac{\mu_s}{J}\left(\mathbf{F}\cdot\mathbf{F}^{\mathbf{T}} - \mathbf{I}\right) + \frac{\lambda_s}{J}\ln(J)\boldsymbol{I}. \tag{A.5}$$

whilst for the algebraic,

$$\boldsymbol{\sigma}_e = \frac{\mu_s}{J}\left(\mathbf{F}\cdot\mathbf{F}^{\mathbf{T}} - \boldsymbol{I}\right) + \lambda_s(J-1)\boldsymbol{I}. \tag{A.6}$$

Ogden

An Ogden type hyperelastic model is used to describe the behaviour of brain tissue by García and Smith (2009), applied to infusion tests. The strain energy function for a compressible, isotropic N family Ogden material takes the form (Ogden, 1984),

$$W = \sum_{n=1}^{N} \frac{\mu_n}{\alpha_n}\left(\lambda_1^{\alpha_n} + \lambda_2^{\alpha_n} + \lambda_3^{\alpha_n}\right) + f(J) \tag{A.7}$$

where α_i and μ_i are material constants, and the volumetric term $f(J)$ is a function of J such that $f(1) = 0$. Following García and Smith (2009) we choose

$$f(J) = -\sum_{n=1}^{N} \mu_n \ln(J) + \frac{\mu'}{2}(J-1)^2 \tag{A.8}$$

In addition to the Lamé parameters, the Ogden model requires additional material parameters α_i. The parameters of the Ogden model can be related to the Young's modulus

and Poisson ratio by,

$$E = (1+\nu)\sum_{n=1}^{N}\alpha_n\mu_n, \qquad \nu = \frac{\mu'}{2\mu' + \sum_{n=1}^{N}\alpha_n\mu_n}. \tag{A.9}$$

Thus for a one-family ($n = 1$) Ogden model, for a given Young's modulus E, Poisson ratio ν, and α_1, the remaining parameters μ' and μ_1 may be calculated by rearranging equations (A.9),

$$\mu_1 = \frac{E}{(1+\nu)\alpha_1}, \qquad \mu' = \frac{\alpha_1\mu_1}{1-2\nu}. \tag{A.10}$$

The neo-Hookean model (A.2) is a special case of the Ogden model (A.7): a one-family model with $\alpha_1 = 2$.

Fung

The Fung model was used by Elkin *et al.* (2010) to model the equilibrium behaviour of brain tissue slices in solution baths of differing concentrations. The general form of the strain energy function for a Fung elastic material is (Ateshian and Costa, 2009),

$$W = \frac{1}{2}b\left(e^{Q}-1\right), \tag{A.11}$$

where b is a material constant with units of stress and

$$Q = \frac{1}{4c}\left[\lambda_s(\mathrm{tr}\mathbf{B}-3)^2 + 2\mu_s(\mathrm{tr}(\mathbf{B}^2) - 2\mathrm{tr}\mathbf{B} + 3)\right], \tag{A.12}$$

where $\mathbf{B} = \mathbf{F}\cdot\mathbf{F}^T$ is the left Cauchy-Green deformation tensor and c is an additional elastic modulus (with units of stress) which determines the exponential rise. The stress tensor has the form,

$$\boldsymbol{\sigma}_e = \frac{1}{2J}e^{Q}\left[\lambda_s(\mathrm{tr}\mathbf{B}-3)\mathbf{B} + 2\mu_s(\mathbf{B}^2-\mathbf{B})\right]. \tag{A.13}$$

Appendix B

Numerical solution methods for a spherically symmetric, steady state, biphasic model

In this Appendix, we explain how we solve the steady-state biphasic problem (as described in §4.2 and §4.3.2 of Chapter 4) for a step function form of BBB permeability $\bar{L}_p(R)$, such that

$$\bar{L}_p(R) = \begin{cases} \bar{L}_{pI} & 0 < R < R_I, \\ \bar{L}_{pO} & R_I < R < 1, \end{cases} \tag{B.1}$$

where $\bar{L}_{pI}$ and $\bar{L}_{pO}$ are constants, representing the BBB permeability in the inner ($0 < R < R_I$) and outer ($R_I < R < 1$) regions respectively. We first discuss the infinitesimal deformation steady-state problem (4.25)-(4.26), and then proceed to the more complicated finite deformation steady-state problem (4.38)-(4.39).

Solution methods for infinitesimal deformations

The steady-state approximation to the governing equations (4.25)-(4.26), appropriate for the infinitesimal problem, may be solved exactly for the two-layer sphere problem. In each of the inner ($0 < r < \bar{r}_I$) and outer ($\bar{r}_I < r < 1$) regions, solutions for the displacement and pressure are of the form,

$$p = \bar{P}_e + \frac{1}{r}\left(A\cosh(lr) + B\sinh(lr)\right), \tag{B.2}$$

$$u = \frac{C}{r^2} + Dr + \frac{1}{r^2 l^2(\bar{\lambda}_s + 2\bar{\mu}_s)}\left[A\left(\cosh lr - lr\sinh lr\right) + B\left(\sinh(lr) - lr\cosh lr\right)\right], \tag{B.3}$$

where $l = \sqrt{\bar{L}_{pI}}$ in the inner region and $l = \sqrt{\bar{L}_{pO}}$ in the outer region. There are 8 constants (A, B, C and D in each region), which can be found from the symmetry boundary conditions at $r = 0$ (4.17), boundary conditions at the outer surface (4.23), and from matching the pressure, displacement, stress and fluid flux at the interface between the two regions ($r = \bar{r}_I$).

As an alternative approach, we can also solve the system numerically, using a multi-point boundary value problem solver in Matlab (*e.g.'bvp5c'*). Having verified our numerical solution method via a comparison with the analytical solution in the infinitesimal deformation case, we may then proceed to determine numerical solutions for the finite deformation case where an analytical solution is not possible.

To solve the infinitesimal equations numerically, we use the Matlab boundary value solver *'bvp5c'*. We introduce further variables m and n to write the steady-state system (4.25)-(4.26) as a set of ordinary first-order differential equations,

$$\frac{\mathrm{d}p}{\mathrm{d}r} = m, \tag{B.4}$$

$$\frac{\mathrm{d}u}{\mathrm{d}r} = n, \tag{B.5}$$

$$\frac{\mathrm{d}m}{\mathrm{d}r} = -\bar{L}(\bar{P}_e - p) - 2\frac{m}{r}, \tag{B.6}$$

$$\frac{\mathrm{d}n}{\mathrm{d}r} = m - 2\frac{n}{r} + 2\frac{u}{r^2}. \tag{B.7}$$

The boundary conditions can also be rewritten in the same notation to yield eight conditions. At the origin,

$$m|_0 = 0, \qquad u|_0 = 0, \tag{B.8}$$

and the outer edge,

$$m|_1 = -\bar{\Gamma}\, p|_1\,, \qquad u|_1 = 0. \tag{B.9}$$

Additionally, at the interface between the inner and outer regions, continuity of pressure, displacement, stress and fluid flux must be preserved. Thus,

$$[p]_{\bar{R}_I} = 0, \qquad [u]_{\bar{R}_I} = 0 \qquad [m]_{\bar{R}_I} = 0 \qquad [n]_{\bar{R}_I} = 0, \tag{B.10}$$

where $[]_{\bar{R}_I}$ denotes the change at $r = \bar{R}_I$.

We wish to solve this system on the domain $r \in [0, 1]$, yet the governing equations appear to be singular at $r = 0$ (due to the $1/r$ terms on the right hand side of equations (B.6) and (B.7). To overcome this, we consider the truncated domain $[\varepsilon, 1]$ for some

$\varepsilon \ll 1$. We replace the boundary conditions (B.8) at $r = 0$ with appropriate conditions at $r = \varepsilon$, which are determined as follows.

For $r \ll 1$, we represent each dependent variable as a Taylor expansion about $r = 0$,

$$p(r) = p_0 + rp_1 \ + \mathcal{O}(r^2), \tag{B.11}$$

$$u(r) = 0 \ + ru_1 \ + \mathcal{O}(r^2), \tag{B.12}$$

$$m(r) = 0 \ + rm_1 + \mathcal{O}(r^2), \tag{B.13}$$

$$n(r) = n_0 + rn_1 \ + \mathcal{O}(r^2), \tag{B.14}$$

where $p_i := p^{(i)}(0)/i!$ and similarly for u_i, m_i and n_i. Note that we have substituted in the boundary conditions at $r = 0$ (B.8), so that $u_0 = 0$ and $m_0 = 0$. Each of these expressions can be differentiated, to give,

$$\frac{\mathrm{d}p}{\mathrm{d}r}(r) = p_1 + 2rp_2 + \mathcal{O}(r^2), \tag{B.15}$$

along with equivalent expressions for the derivatives of u, m and n.

We now substitute the Taylor expansions (B.11)-(B.14) and their derivatives (*e.g.* B.15) into the governing equations (B.4)-(B.7) at $r = \varepsilon$, and evaluate each governing equation to leading order in ε. This yields two relationships for the leading-order terms in the expansions (B.11)-(B.14):

$$u_1 = n_0, \tag{B.16}$$

$$3m_1 = -\bar{L}(\bar{P}_e - p_0). \tag{B.17}$$

Substituting these expressions into the Taylor series for $u(r)$ (B.12) and $m(r)$ (B.13) at $r = \varepsilon$ gives leading-order boundary conditions at $r = \varepsilon$,

$$u|_\varepsilon = \varepsilon \, n|_\varepsilon \,, \qquad\qquad m|_\varepsilon = -\frac{\bar{L}\varepsilon}{3}(\bar{P}_e - p|_\varepsilon), \tag{B.18}$$

which replace the original conditions at $r = 0$ (B.8). These boundary conditions (B.18) are accurate up to order ε^2.

The system (B.4)-(B.7) can now be solved as a multipoint boundary-value problem on the domain $[\varepsilon, 1]$, with boundary conditions at $r = \varepsilon$ (B.18), $r = 1$ (B.9), and an internal boundary at $r = \bar{r}_I$ (B.10). Since we have approximations for the boundary conditions appropriate up to order ε^2, we expect our solution to show errors of order ε^2.

Figure B.1 shows the maximum absolute error of the numerical solution in comparison to the exact solution. The maximal error is calculated by subtracting the exact solution from the numerical solution at each gridpoint over the domain, and taking the maximum

value. The absolute and relative error of the Matlab boundary value solver *'bvp5c'* are set to be smaller than the values of ε tested, to ensure that we isolate only the errors introduced into the system by Taylor expanding close to $r = 0$. We see that the errors are indeed of order ε^2.

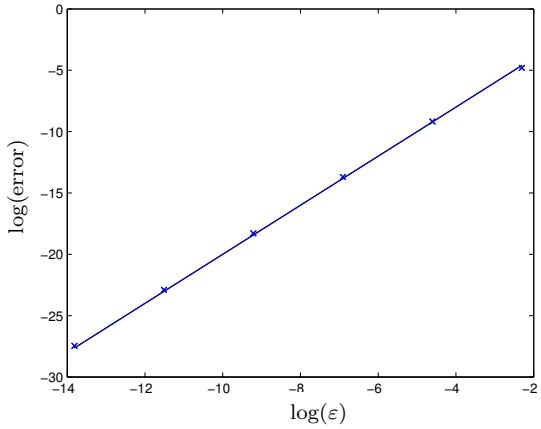

Figure B.1: Plot showing the maximum error introduced into solutions to the infinitesimal two-layered sphere system, when solved on a truncated domain $[\varepsilon, 1]$ using the Matlab boundary value solver *'bvp5c'* (crosses). The solid line has gradient 2, showing that the error is proportional to ε^2.

Numerical solutions for finite deformations

Having validated our numerical method, we now employ it to solve the finite deformation problem. We again define two new variables, so that the governing equations (4.38)-(4.39) may be written as a set of four coupled first-order nonlinear ordinary differential equations,

$$m(R) = \frac{\mathrm{d}p}{\mathrm{d}R}, \tag{B.19}$$

$$n(R) = \frac{\mathrm{d}f}{\mathrm{d}R}, \tag{B.20}$$

$$\frac{\mathrm{d}m}{\mathrm{d}R} = -\left[\frac{2n}{f} - \frac{1}{n}\frac{\mathrm{d}n}{\mathrm{d}R}\right]\frac{\mathrm{d}p}{\mathrm{d}R} - n^2 L_p\left(\bar{P}_e - p\right), \tag{B.21}$$

$$\frac{\mathrm{d}n}{\mathrm{d}R} = \frac{1}{A_1(R,f,n)}\left[A_2(R,f,n) - \frac{2(S_{RR} - S_{\Phi\Phi})}{R} + \frac{f^2}{R^2}m\right], \tag{B.22}$$

where,

$$
\begin{aligned}
A_1 &= \left[\mu_s\left(1+\frac{1}{n^2}\right)+\lambda_s\frac{f^4}{R^4}\right], \\
A_2 &= \lambda_s\left[\frac{1}{R^5}\left(4f^3n^2R-4f^4n\right)-\frac{1}{R^3}\left(2Rfn-2f^2\right)\right], \\
S_{rr} &= \frac{1}{n}\left[\mu_s(n^2-1)+\lambda_s J(J-1)\right], \\
S_{\theta\theta} &= \frac{R}{f}\left[\mu_s\left(\left(\frac{f}{R}\right)^2-1\right)+\lambda_s J(J-1)\right],
\end{aligned}
$$

(for a neo-Hookean strain energy function), with $J = f^2n/R^2$. Thus equations (B.19) - (B.22) constitute a set of 4 ODEs for the system.

As in the infinitesimal case, we observe that the above equations cannot be solved with the inbuilt Matlab solver at $R = 0$. Therefore, we again truncate the domain to $[\varepsilon, 1]$ (for some $\varepsilon \ll 1$), and similarly perform a Taylor expansion of each variable to obtain an approximation to the symmetry boundary conditions (4.17) at ε. Following the procedure explained above yields two boundary conditions at $R = \varepsilon$ to replace those at $R = 0$:

$$3\, m|_{\varepsilon} = -\varepsilon \bar{L_p}\,(n|_{\varepsilon})^2\,(\bar{P}_e - p|_{\varepsilon}), \tag{B.23}$$

$$f|_{\varepsilon} = \varepsilon\, n|_{\varepsilon}\,. \tag{B.24}$$

In addition, we have boundary conditions on the outer edge (4.23), and continuity of pressure, displacement, stress and fluid flux at the inner boundary $R = R_I$.

We can now again use the inbuilt Matlab boundary value solver, *'bvp5c'*. As the solver requires an initial guess to be input by the user, we input the solution to the linear problem as the initial guess for the nonlinear solutions.

Appendix C

Glossary of biological terms

Axons	Long slender projection of neurons, that transmit information (in the form of electrical signals) to other neurons and cells in the body.
Astrocytes	Cells that support the function of the brain. They perform many roles, such as providing nutrients to the neurons and maintaining the extracellular ion balance.
Blood brain barrier (BBB)	Interface separating the blood and brain tissue. This barrier is highly selective, allowing control of the composition of the ISF.
Cerebrospinal fluid (CSF)	Fluid that bathes the brain and spinal cord. It is located in the ventricles and subarachnoid space of the brain.
Contusion	A bruise. This is caused when capillaries are damaged, allowing blood to seep into the tissue.
Craniectomy	Neurosurgical procedure, in which a section of the skull is removed to help relieve increased intracranial pressure.
Cytotoxic edema	Swelling of individual cells. This is caused when cellular metabolism is disrupted, which prevents the cell from maintaining an osmotic equilibrium with the interstitial fluid, and allows water to accumulate in the cell.
Donnan effect	Where immobile FCD induces a greater osmotic pressure in the tissue than its surroundings.
Edema	Swelling of soft tissue due to excess fluid accumulation.
Fixed charge density (FCD)	A (usually negative) charge on the solid components (*e.g.* extracellular and intracellular matrix) of biological tissue.

Hydrocephalus	Abnormal accumulation of CSF in the ventricles (causing ventricle expansion and tissue deformation).
Infarction	Regional of tissue death, caused by lack of oxygen.
Interstitial fluid (ISF)	Solution that bathes and surrounds brain cells.
Ischemia	Inadequate blood supply to a local area due to blockage of blood vessels (leading to lack of oxygen).
Neurons	Electrically excitable cells that transmit information through the brain, via electrical and chemical signals.
Subarachnoid space (SAS)	Space between the membrane layers on the outer surface of the brain, containing CSF.
Vasogenic edema	Brain swelling caused by a breakdown of the BBB.
Ventricles	Communicating network of CSF-filled cavities, located within the brain.

Bibliography

N. J. Abbott. Evidence for bulk flow of brain interstitial fluid: significance for physiology and pathology. *Neurochem. Int.*, 45(4):545–552, 2004.

N. J. Abbott, L. Rönnbäck, and E. Hansson. Astrocyte-endothelial interactions at the blood-brain barrier. *Nat. Rev. Neurosci.*, 7:41–53, 2006.

N. J. Abbott, A. A. Patabendige, D. Dolman, S. Yusof, and D. Begley. Structure and function of the blood-brain barrier. *Neurobio. Dis.*, 37:13–25, 2010.

J. Astrup, B. K. Siesj, and L. Symon. Thresholds in cerebral ischemia - the ischemic penumbra. *Stroke*, 12(6):723–5, 1981.

G. A. Ateshian and K. D. Costa. A frame-invariant formulation of fung elasticity. *J. Biomech.*, 42(6):781–785, 2009.

G. A. Ateshian, M. Likhitpanichkul, and C. T. Hung. A mixture theory analysis for passive transport in osmotic loading of cells. *J. Biomech.*, 39(3):464–475, 2006.

Atkins. *Physical Chemistry*. OUP, 8th edition, 2006.

C. Ayata and A. H. Ropper. Ischaemic brain oedema. *J. Clin. Neurosci.*, 9(2):113–124, 2002.

A. C. Bain and D. F. Meaney. Tissue-level thresholds for axonal damage in an experimental model of central nervous system white matter injury. *J. Biomech . Eng.*, 122 (6):615–622, 2000.

P. J. Basser. Interstitial pressure, volume, and flow during infusion into brain tissue. *Microvasc Res.*, 44(2):143–65, 1992.

L. E. Bilston. Brain tissue mechanical properties. In K. Miller, editor, *Biomechanics of the Brain*, Biological and Medical Physics, Biomedical Engineering, pages 69–89. Springer New York, 2011. ISBN 978-1-4419-9996-2.

M. A. Biot. General theory of three-dimensional consolidation. *J. appl. phys.*, 12(2): 155–164, 1941.

J. Bonet and R. D. Wood. *Nonlinear Continuum Mechanics for Finite Element Analysis*. Cambridge University Press, 1997.

M. Bradbury. The blood-brain barrier. Transport across the cerebral endothelium. *Circulation research*, 57(2):213–222, 1985.

P. Brown, S. Davies, T. Speake, and I. Millar. Molecular mechanisms of cerebrospinal fluid production. *Neuroscience*, 129:955–968, 2004.

R. Burridge and J. B. Keller. Poroelasticity equations derived from microstructure. *J. Acoust. Soc. Am.*, 70:1140, 1981.

H. M. Byrne, J. R. King, D. S. McElwain, and L. Preziosi. A two-phase model of solid tumour growth. *Appl. Math. Lett.*, 16(4):567–573, 2003.

X. Chen and M. Sarntinoranont. Biphasic finite element model of solute transport for direct infusion into nervous tissue. *Ann. Biomed. Eng.*, 35(12):2145–2158, 2007.

S. Cheng and E. Bilston, L. Unconfined compression of white matter. *J. Biomech.*, 40 (1):117–124, 2007.

S. Cho, A. Wood, and M. Bowlby. Brain slices as models for neurodegenerative disease and screening platforms to identify novel therapeutics. *Curr. Neuropharmacol.*, 5(1): 19, 2007.

R. S. Chung, J. A. Staal, G. H. McCormack, T. C. Dickson, M. A. Cozens, J. A. Chuckowree, M. C. Quilty, and J. C. Vickers. Mild axonal stretch injury in vitro induces a progressive series of neurofilament alterations ultimately leading to delayed axotomy. *J. Nneurotrauma*, 22(10):1081–1091, 2005.

D. J. Cooper, J. V. Rosenfeld, L. Murray, Y. M. Arabi, A. R. Davies, P. D'Urso, T. Kossmann, J. Ponsford, I. Seppelt, P. Reilly, *et al.* Decompressive craniectomy in diffuse traumatic brain injury. *New Engl. J. Med.*, 364(16):1493–1502, 2011.

O. Coussy. *Poromechanics*. Wiley, 2004.

S. C. Cowin and S. B. Doty. *Tissue Mechanics*. Springer, 2009.

M. Czosnyka and J. D. Pickard. Monitoring and interpretation of intracranial pressure. *J. Neurolo. Neurosurg. Psychiatry*, 75(6):813–821, 2004.

Y. Davit, C. G. Bell, H. M. Byrne, L. A. Chapman, L. S. Kimpton, G. E. Lang, K. H. Leonard, J. M. Oliver, N. C. Pearson, R. J. Shipley, *et al.* Homogenization via formal multiscale asymptotics and volume averaging: How do the two techniques compare? *Adv. Water Resour.*, 62:178–206, 2013.

E. Detournay and A. H.-D. Cheng. Fundamentals of poroelasticity. 1999.

V. Dhawan and M. DeGeorgia. Neurointensive care biophysiological monitoring. *J. Neurointervent. Surg.*, 4(6):407–413, 2012.

E. Dickinson, J. Limon-Petersen, and R. Compton. The electroneutrality approximation in electrochemistry. *J. Solid State Electrochem.*, 15:1335–1345, 2011.

M. Diringer and A. Zazulia. Osmotic therapy. *Neurocritical Care*, 1(2):219–233, 2004.

F. G. Donnan. The theory of membrane equilibria. *Chem. Rev.*, 1(1):73–90, 1924.

C. S. Drapaca and J. S. Fritz. A mechano-electrochemical model of brain neuro-mechanics: Application to normal pressure hydrocephalus. *Int. J. Num. Anal. Mod., Ser. B*, 1: 82–93, 2012.

D. Drew. Mathematical modeling of two-phase flow. *Annual Rev. Fluid Mech.*, 15(1): 261–291, 1983.

M.-A. Dronne, J.-P. Boissel, and E. Grenier. A mathematical model of ion movements in grey matter during a stroke. *J. Theor. Biol.*, 240(4):599–615, 2006.

L. T. Dunn. Raised intracranial pressure. *J. Neurolo. Neurosurg. Psychiatry*, 73(suppl 1):i23–i27, 2002.

B. S. Elkin, M. A. Shaik, and B. Morrison III. Fixed negative charge and the Donnan effect: A description of the driving forces associated with brain tissue swelling and edema. *Phil. Trans. Royal Soc. London A*, 368(1912):585–603, 2010.

M. Erecińska and I. A. Silver. Tissue oxygen tension and brain sensitivity to hypoxia. *Respiration physiology*, 128(3):263–276, 2001.

J. Fenstermacher and C. Patlak. The movements of water and solutes in the brains of mammals. In *Dynamics of Brain Edema*, pages 87–94. Springer, 1976.

M. Fisher and J. H. Garcia. Evolving stroke and the ischemic penumbra. *Neurology*, 47 (4):884–888, 1996.

R. A. Fishman. Brain edema. *N. Engl. J. Med.*, 293(14):706–711, 1975.

G. Franceschini, D. Bigoni, P. Regitnig, and G. Holzapfel. Brain tissue deforms similarly to filled elastomers and follows consolidation theory. *J. Mech. Phys. Solids*, 54(12): 2592 – 2620, 2006.

A. Frijns, J. Huyghe, and J. Janssen. A validation of the quadriphasic mixture theory for intervertebral disc tissue. *Int. J. Eng. Sci.*, 35(15):1419 – 1429, 1997.

Y. Fung. Structure and stress-strain relationship of soft tissues. *American Zoologist*, 24 (1):13–22, 1984.

R. Ganfield, P. Nair, and W. Whalen. Mass transfer, storage, and utilization of O2 in cat cerebral cortex. *Am. J. Physiol.*, 219:814821, 1970.

J. J. García and J. H. Smith. A biphasic hyperelastic model for the analysis of fluid and mass transport in brain tissue. *Ann. Biomed. Eng.*, 37:375–386, 2009.

J. J. García and J. H. Smith. A biphasic hyperelastic model for hydrocephalus. *Lat. Am. Appl. Res.*, 40(4):295–302, 2010.

T. Gerriets, E. Stolz, M. Walberer, C. Mller, A. Kluge, A. Bachmann, M. Fisher, M. Kaps, and G. Bachmann. Noninvasive quantification of brain edema and the space-occupying effect in rat stroke models using magnetic resonance imaging. *Stroke*, 35:566–571, 2004.

T. Gerriets, M. Walberer, N. Ritschel, M. Tschernatsch, C. Mueller, G. Bachmann, M. Schoenburg, M. Kaps, and M. Nedelmann. Edema formation in the hyperacute phase of ischemic stroke. *J. Neurosurg.*, 111(5):1036–1042., 2009.

W. Gu, W. Lai, and V. Mow. Transport of fluid and ions through a porous-permeable charged-hydrated tissue, and streaming potential data on normal bovine articular cartilage. *J. Biomech.*, 26(6):709–723, 1993.

W. Gu, W. Lai, and V. Mow. Transport of multi-electrolytes in charged hydrated biological soft tissues. *Transport Porous Med.*, 34(1-3):143–157, 1999.

W. Gu, H. Yao, C. Huang, and H. Cheung. New insight into deformation-dependent hydraulic permeability of gels and cartilage, and dynamic behavior of agarose gels in confined compression. *J. Biomech.*, 36(4):593–598, 2003.

S. Hatashita, J. T. Hoff, and S. M. Salamat. Ischemic brain edema and the osmotic gradient between blood and brain. *J. Cereb. Blood Flow Metab.*, 8(4):525–559, 1988.

M. Holmes and V. Mow. The nonlinear characteristics of soft gels and hydrated connective tissues in ultrafiltration. *J. Biomech.*, 23(11):1145–1156, 1990.

M. H. Holmes. A theoretical analysis for determining the nonlinear hydraulic permeability of a soft tissue from a permeation experiment. *Bull. Math. Biol.*, 47(5):669–683, 1985.

G. A. Holzapfel, T. C. Gasser, and R. W. Ogden. A new constitutive framework for arterial wall mechanics and a comparative study of material models. *J. Elasticity*, 61: 1–48, 2000.

L. D. Homer, J. B. Shelton, and T. J. Williams. Diffusion of oxygen in slices of rat brain. *Am. J. Physiol. Regul. Integr. Comp. Physiol.*, 244::R15–R22,, 1983.

P. Howell, G. Kozyreff, and J. Ockendon. *Applied Solid Mechanics*. Cambridge University Press, 2009.

S. Hrabětová, K. C. Chen, D. Masri, and C. Nicholson. Water compartmentalization and spread of ischemic injury in thick-slice ischemia model. *J. Cereb. Blood Flow Metab.*, 22:80–88, 2002.

C.-Y. Huang and W. Y. Gu. Effects of tension-compression nonlinearity on solute transport in charged hydrated fibrous tissues under dynamic unconfined comression. *J. Biomech.*, 129(3):423, 2007.

J. Huyghe and J. Janssen. Quadriphasic mechanics of swelling incompressible porous media. *Int. J. Eng. Sci.*, 35(8):793–802, 1997.

C. E. Johanson. Choroid plexuscerebrospinal fluid circulatory dynamics: Impact on brain growth, metabolism, and repair. In P. M. Conn, editor, *Neuroscience in Medicine*, pages 173–200. Humana Press, 2008.

C. E. Johanson, J. A. Duncan, P. M. Klinge, T. Brinker, E. G. Stopa, and G. D. Silverberg. Multiplicity of cerebrospinal fluid functions: New challenges in health and disease. *Cerebrospinal Fluid Res.*, 5(1):10, 2008.

M. Kaczmarek, R. P. Subramaniam, and S. R. Neff. The hydromechanics of hydrocephalus: Steady-state solutions for cylindrical geometry. *B. Math. Biol.*, 59(2):295–323, 1997.

K. T. Kahle, J. M. Simard, K. J. Staley, B. V. Nahed, P. S. Jones, and D. Sun. Molecular mechanisms of ischemic cerebral edema: Role of electroneutral ion transport. *Physiology*, 24(4):257–265, 2009.

S. Kalyanasundaram, V. Calhoun, and K. Leong. A finite element model for predicting the distribution of drugs delivered intracranially to the brain. *Am. J. Physiol. Regul. Integr. Comp. Physiol.*, 273(5):R1810–R1821, 1997.

Y. Katayama and T. Kawamata. Edema fluid accumulation within necrotic brain tissue as a cause of the mass effect of cerebral contusion in head trauma patients. In T. Kuroiwa, A. Baethmann, Z. Czernicki, J. Hoff, U. Ito, Y. Katayama, A. Marmarou, B. Mendelow, and H.-J. Reulen, editors, *Brain Edema XII*, volume 86 of *Acta Neurochirurgica Supplements*, pages 323–327. Springer Vienna, 2003. ISBN 978-3-7091-7220-9.

A. Katchaslsky and P. F. Curran. *Nonequilibrium Thermodynamics in Biophysics*. Harvard University Press, 1974.

T. Kawamata, T. Mori, S. Sato, and Y. Katayama. Tissue hyperosmolality and brain edema in cerebral contusion. *Neurosurg. Focus*, 22(5):1–8, 2007.

J. P. Keener and J. Sneyd. *Mathematical Physiology*, volume 8. Springer, 1998.

H. K. Kimelberg. Current concepts of brain edema: Review of laboratory investigations. *J. Neurosurg.*, 83:1051–1059, 1995.

I. Klatzo. Pathophysiological aspects of brain edema. *Acta Neuropathol.*, 72:236–239, 1987.

R. Korthuis, J. Scallan, and V. Huxley. *Capillary Fluid Exchange: Regulation, Functions, and Pathology*. Morgan Claypool Publishers, 2010.

S. K. Kyriacou, A. Mohamed, K. Miller, and S. Neff. Brain mechanics for neurosurgery: Modeling issues. *Biomech. Model. Mechanobiol.*, 1(2):151–164, 2002.

W. M. Lai, J. S. Hou, and V. C. Mow. A triphasic theory for the swelling and deformation behaviors of articular cartilage. *J. Biomech. Eng.*, 113(3):245–58, 1991.

G. E. Lang, P. S. Stewart, D. Vella, S. L. Waters, and A. Goriely. Is the Donnan effect sufficient to explain swelling in brain tissue slices? *J. R. Soc. Interface*, 11(96), 2014.

A. Leaf. Maintenance of concentration gradients and regulation of cell volume. *Ann. N. Y. Acad. Sci.*, 72(12):396–404, 1959.

G. Lemon, J. R. King, H. M. Byrne, O. E. Jensen, and K. M. Shakesheff. Mathematical modelling of engineered tissue growth using a multiphase porous flow mixture theory. *J. Math. Biol.*, 52(5):571–594, 2006.

J. Levick. Flow through interstitium and other fibrous matrices. *Exp. Physiol.*, 72(4): 409–437, 1987.

D. N. Levine. The pathogenesis of normal pressure hydrocephalus: a theoretical analysis. *Bull. Math. Biol.*, 61(5):875–916, 1999.

D. Liang, S. Bhatta, V. Gerzanich, and J. Simard. Cytotoxic edema: Mechanisms of pathological cell swelling. *Neurosurg. Focus*, 22(5):E2, 2007.

A. A. Linninger, M. Xenos, B. Sweetman, S. Ponkshe, X. Guo, and R. Penn. A mathematical model of blood, cerebrospinal fluid and brain dynamics. *J. Math. Biol.*, 59(6): 729–759, 2009.

E. H. Lo, M. A. Moskowitz, and T. P. Jacobs. Exciting, radical, suicidal how brain cells die after stroke. *Stroke*, 36(2):189–192, 2005.

X. Lu and V. Mow. Biomechanics of articular cartilage and determination of material properties. *Med. Sci. Sports Exerc.*, 40(2):193, 2008.

J. MacLaurin, J. Chapman, G. W. Jones, and T. Roose. The buckling of capillaries in solid tumours. *Proc. R. Soc. A*, 468(2148):4123–4145, 2012.

A. Mak, W. Lai, and V. Mow. Biphasic indentation of articular cartilage1. Theoretical analysis. *J. Biomech.*, 20(7):703–714, 1987.

B. Markert. A constitutive approach to 3-D nonlinear fluid flow through finite deformable porous continua. *Transp. Porous Media*, 70(3):427–450, 2007.

A. Marmarou. A review of progress in understanding the pathophysiology and treatment of brain edema. *Neurosurg. Focus*, 22:5:1–10, 2007.

A. Marmarou, P. P. Fatouros, P. Barz, G. Portella, M. Yoshihara, O. Tsuji, T. Yamamoto, F. Laine, S. Signoretti, J. D. Ward, M. R. Bullock, and H. F. Young. Contribution of edema and cerebral blood volume to traumatic brain swelling in head-injured patients. *J. Neurosurg.*, 93(2):183–193, 2000.

R. L. Mauck, C. T. Hung, and G. A. Ateshian. Modeling of neutral solute transport in a dynamically loaded porous permeable gel: implications for articular cartilage biosynthesis and tissue engineering. *J. Biomech.*, 125(5):602, 2003.

M. L. McManus, K. B. Churchwell, and K. Strange. Regulation of cell volume in health and disease. *N. Engl. J. Med.*, 333:1260–1266, 1995.

H. Metz, J. McElhaney, and A. K. Ommaya. A comparison of the elasticity of live, dead, and fixed brain tissue. *J. Biomech.*, 3(4):453 – 458, 1970.

K. Miller. Modelling soft tissue using biphasic theory-a word of caution. *Comput. Methods. Biomech. Biomed. Engin.*, 1(3):261–263, 1997.

K. Miller. Constitutive model of brain tissue suitable for finite element analysis of surgical procedures. *J. Biomech.*, 32(5):531–537, 1999.

K. Miller and K. Chinzei. Constitutive modelling of brain tissue: Experiment and theory. *J. Biomech.*, 30(11-12):1115–1121, 1997.

K. Miller and K. Chinzei. Mechanical properties of brain tissue in tension. *J. Biomech.*, 35(4):483–490, 2002.

V. C. Mow, S. C. Kuei, W. M. Lai, and C. G. Armstrong. Biphasic creep and stress relaxation of articular cartilage in compression: Theory and experiments. *J. Biomech. Eng.*, 102:73–84, 1980.

S. Nag, J. Manias, and D. Stewart. Pathology and new players in the pathogenesis of brain edema. *Acta Neuropathol.*, 118:197–217, 2009.

T. Nagashima, T. Shirakuni, and S. I. Rapoport. A two-dimensional, finite element analysis of vasogenic brain edema. *Neurol. Med. Chir.*, 30(1):1, 1990.

P. K. Narotam, J. F. Morrison, and N. Nathoo. Brain tissue oxygen monitoring in traumatic brain injury and major trauma: Outcome analysis of a brain tissue oxygen-directed therapy: Clinical article. *J. neurosurg.*, 111(4):672–682, 2009.

National Stroke Association. www.stroke.org.

C. Nicholson. Diffusion and related transport mechanisms in brain tissue. *Rep. Prog. Phys.*, 64:815–884, 2001.

C. Nicholson and J. M. Phillips. Ion diffusion modified by tortuosity and volume fraction in the extracellular microenvironment of the rat cerebellum. *J. Physiol.*, 321:225–257, 1981.

J. Nolte. *The Human Brain: An Introduction to Its Functional Anatomy.* C.V. Mosby, 4th edition, 1998.

U. Novak and A. H. Kaye. Extracellular matrix and the brain: Components and function. *J. Clin. Neurosci.*, 7(4):280–290, 2000.

R. O'Dea, H. Byrne, and S. Waters. Continuum modelling of in vitro tissue engineering: A review. In *Stud. Mechanobiol. Tissue Eng. Biomate.* Springer-Verlag Berlin Heidelberg, 2012.

R. W. Ogden. *Non Linear Elastic Deformations.* Ellis-Horwood, 1984.

L. Østergaard, S. N. Jespersen, K. Mouridsen, I. K. Mikkelsen, K. Ý. Jonsdottír, A. Tietze, J. U. Blicher, R. Aamand, N. Hjort, N. K. Iversen, *et al.* The role of the cerebral capillaries in acute ischemic stroke: The extended penumbra model. *J. Cereb. Blood Flow Metab.*, 33(5):635–648, 2013.

M. Papadopoulos, S. Saadoun, D. Binder, G. Manley, S. Krishna, and A. Verkman. Molecular mechanisms of brain tumor edema. *Neuroscience*, 129(4):1009–1018, 2004.

M. C. Papadopoulos, S. Krishna, and A. Verkman. Aquaporin water channels and brain edema. *Mt. Sinai J. Med.*, 69(4):242–248, 2002.

H. M. Pappius and K. Elliott. Water distribution in incubated slices of brain and other tissues. *Can. J. Biochem. Physiol.*, 34(5):1007–1022, 1956.

W. M. Pardridge. Drug delivery to the brain. *J. Cereb. Blood Flow Metab.*, 17(7):713–731, 1997.

R. Penta, D. Ambrosi, and R. Shipley. Effective governing equations for poroelastic growing media. *Quart. J. Mech. Appl. Math.*, 67(1):69–91, 2014.

K. R. Rajagopal and L. Tao. *Mechanics of Mixtures*, volume 754. World scientific Singapore, 1995.

S. I. Rapoport. A mathematical model for vasogenic brain edema. *J. Theor. Biol.*, 74(3): 439–467, 1978.

S. I. Rapoport. 7 - brain edema and the blood-brain barrier. In *Primer on Cerebrovascular Diseases*, pages 25 – 28. Academic Press, San Diego, 1997. ISBN 978-0-12-743170-3.

B. Rashid, M. Destrade, and M. D. Gilchrist. Mechanical characterization of brain tissue in compression at dynamic strain rates. *J. Mech. Behav. Biomed.*, 10(0):23–38, 2012.

B. Rashid, M. Destrade, and M. D. Gilchrist. Influence of preservation temperature on the measured mechanical properties of brain tissue. *J. Biomech.*, 46(7):1276–1281, 2013.

Z. B. Redzic, J. E. Preston, J. A. Duncan, A. Chodobski, and J. Szmydynger-Chodobska. The choroid plexus-cerebrospinal fluid system: From development to aging. *Curr. Top. Dev. Biol.*, 71:1–52, 2005.

H. J. Reulen, R. Graham, M. Spatz, and I. Klatzo. Role of pressure gradients and bulk flow in dynamics of vasogenic brain edema. *J. Neurosurg.*, 46(1):24–35, 1977.

T. Secomb, R. Hsu, N. Beamer, and B. Coull. Theoretical simulation of oxygen transport to brain by networks of microvessels: Effects of oxygen supply and demand on tissue hypoxia. *Microcirculation*, 7(4):237–247, 2000.

J. M. Simard, T. A. Kent, M. Chen, K. V. Tarasov, and V. Gerzanich. Brain oedema in focal ischaemia: molecular pathophysiology and theoretical implications. *Lancet Neurol.*, 6:258–68, 2007.

B. R. Simon. Multiphase poroelastic finite element models for soft tissue structures. *Appl. Mech. Rev*, 45(6):191–218, 1992.

A. Smillie, I. Sobey, and Z. Molnar. A hydroelastic model of hydrocephalus. *J. Fluid Mech.*, 539:417–443, 2005.

D. H. Smith and D. F. Meaney. Axonal damage in traumatic brain injury. *Neuroscientist*, 6(6):483–495, 2000.

J. H. Smith and J. A. Humphrey. Interstitial transport and transvascular fluid exchange during infusion into brain and tumor tissue. *Microvascular research*, 73(1):58–73, 2007.

Q. R. Smith. A review of blood-brain barrier transport techniques. In S. Nag, editor, *The Blood-Brain Barrier: Biology and Research Protocols*, pages 193–208. Springer, 2003.

I. Sobey and B. Wirth. Effect of non-linear permeability in a spherically symmetric model of hydrocephalus. *Math. Med. Biol.*, 23:339–361, 2006.

I. Sobey, A. Eisenträger, B. Wirth, and M. Czosnyka. Simulation of cerebral infusion tests using a poroelastic model. *Int. J. Numer. Anal. Model., Ser. B*, 3:52–64, 2012.

J. F. Soustiel, G. E. Sviri, E. Mahamid, V. Shik, S. Abeshaus, and M. Zaaroor. Cerebral blood flow and metabolism following decompressive craniectomy for control of increased intracranial pressure. *Neurosurg.*, 67:6572, 2010.

L. A. Steiner and P. J. D. Andrews. Monitoring the injured brain: ICP and CBF. *Br. J. Anaesth.*, 97(1):26–38, 2006.

S. Strandgaard, J. Olesen, E. Skinhøj, and N. A. Lassen. Autoregulation of brain circulation in severe arterial hypertension. *Br. Med. J.*, 1(5852):507–510, 1973.

K. Strange. Regulation of solute and water balance and cell volume in the central nervous system. *J. Am. Soc. Nephrol.*, 3:12–27, 1973.

D. N. Sun, W. Y. Gu, X. E. Guo, W. M. Lai, and V. C. Mow. A mixed finite element formulation of triphasic mechano-electrochemical theory for charged, hydrated biological soft tissues. *Int. J. Numer. Meth. Eng.*, 45:1375–1402, 1999.

E. Syková and C. Nicholson. Diffusion in brain extracellular space. *Physiol. Rev.*, 88(4): 1277–1340, 2008.

M. D. Tang-Schomer, A. R. Patel, P. W. Baas, and D. H. Smith. Mechanical breaking of microtubules in axons during dynamic stretch injury underlies delayed elasticity, microtubule disassembly, and axon degeneration. *The FASEB Journal*, 24(5):1401–1410, 2010.

Z. Taylor and K. Miller. Reassessment of brain elasticity for analysis of biomechanisms of hydrocephalus. *J. Biomech.*, 37(8):1263–1269, 2004.

G. A. Truskey, F. Yuan, and D. F. Katz. *Transport Phenomena in Biological Systems*. Pearson Prentice Hall Upper Saddle River, NJ, second edition, 2010.

B. Tully and Y. Ventikos. Cerebral water transport using multiple-network poroelastic theory: Application to normal pressure hydrocephalus. *J. Fluid Mech.*, 667:188–215, 2011.

A. Unterberg, J. Stover, B. Kress, and K. Kiening. Edema and brain trauma. *Neuroscience*, 129(4):1019 – 1027, 2004.

M. Ursino. A mathematical study of human intracranial hydrodynamics Part 2-Simulation of clinical tests. *Ann. Biomed. Eng.*, 16(4):403–416, 1988.

M. Walberer, N. Ritschel, M. Nedelmann, K. Volk, C. Mueller, M. Tschernatsch, E. Stolz, F. Blaes, G. Bachmann, and T. Gerriets. Aggravation of infarct formation by brain swelling in a large territorial stroke: A target for neuroprotection? *J. Neurosurg.*, 109 (2):287–293, 2008.

H. F. Wang. *Theory of Linear Poroelasticity with Applications to Geomechanics and Hydrogeology*. Princeton University Press, 2000.

B. Wirth and I. Sobey. An axisymmetric and fully 3D poroelastic model for the evolution of hydrocephalus. *Math. Med. Biol.*, 23(4):363–388, 2006.

B. Wirth and I. Sobey. Analytic solution during an infusion test of the linear unsteady poroelastic equations in a spherically symmetric model of the brain. *Math. Med. Biol.*, 26(1):25–61, 2009.

H. Yao and W. Y. Gu. Convection and diffusion in charged hydrated soft tissues: a mixture theory approach. *Biomech. Model. Mechanobiol.*, 6(1-2):63–72, 2007.

C.-S. Yi, A. L. Fogelson, J. P. Keener, and C. S. Peskin. A mathematical study of volume shifts and ionic concentration changes during ischemia and hypoxia. *J. Theor. Biol.*, 220(1):83–106, 2003.

L. Zhang, K. H. Yang, A. I. King, *et al.* A proposed injury threshold for mild traumatic brain injury. *J .Biomech. Eng.*, 126(2):226–236, 2004.